











Unclassified

SECURITY CLASSIFICATION OF THIS PAGE

## REPORT DOCUMENTATION PAGE

Form Approved  
OMB No. 0704-0188

1a REPORT SECURITY CLASSIFICATION <b>unclassified</b>			1b RESTRICTIVE MARKINGS		
2a SECURITY CLASSIFICATION AUTHORITY			3 DISTRIBUTION/AVAILABILITY OF REPORT Approved for public release; distribution is unlimited.		
2b DECLASSIFICATION/DOWNGRADING SCHEDULE					
4 PERFORMING ORGANIZATION REPORT NUMBER(S)			5 MONITORING ORGANIZATION REPORT NUMBER(S)		
6a NAME OF PERFORMING ORGANIZATION  Naval Postgraduate School		6b OFFICE SYMBOL (If applicable) 33	7a NAME OF MONITORING ORGANIZATION  Naval Postgraduate School		
6c ADDRESS (City, State, and ZIP Code)  Monterey, CA 93943-5000			7b ADDRESS (City, State, and ZIP Code)  Monterey, CA 93943-5000		
8a NAME OF FUNDING/SPONSORING ORGANIZATION		8b OFFICE SYMBOL (If applicable)	9 PROCUREMENT INSTRUMENT IDENTIFICATION NUMBER		
8c ADDRESS (City, State, and ZIP Code)			10 SOURCE OF FUNDING NUMBERS		
			PROGRAM ELEMENT NO	PROJECT NO	TASK NO
			WORK UNIT ACCESSION NO		
11 TITLE (Include Security Classification)  ENHANCED HIGHER ORDER PARAMETRIC X-RADIATION PRODUCTION					
12 PERSONAL AUTHOR(S) DiNova, Kay L.					
13a TYPE OF REPORT Master's Thesis		13b TIME COVERED FROM _____ TO _____		14 DATE OF REPORT (Year, Month, Day) December 1992	
				15 PAGE COUNT 121	
16 SUPPLEMENTARY NOTATION The views expressed in this thesis are those of the author and do not reflect the official policy or position of the Department of Defense or the U.S. Government					
17 COSATI CODES			18 SUBJECT TERMS (Continue on reverse if necessary and identify by block number)		
FIELD	GROUP	SUB-GROUP			
			Parametric X-Radiation, PXR, carbon, Monochromator, Linear Accelerator, Bragg Scattering, Virtual Photons, Crystallography		
19 ABSTRACT (Continue on reverse if necessary and identify by block number)  This thesis examines parametric x-radiation (PXR) which is the Bragg scattering of the virtual photons associated with the Coulomb field of relativistic charged particle from the atomic planes of a crystal. Higher order parametric x-radiation from the {002} planes of a thick mosaic graphite crystal have been observed. The raw PXR data was collected using a SiLi detector and a Pulse Height Analyzer (PHA) software program. The data was corrected for various effects including attenuation, detector drift and efficiency. The absolute number of photons per electron was obtained by using the fluorescent x-ray yield from a tin foil backing on the graphite crystal to determine the LINAC current. The number of photons per electron observed greatly exceeds the expected values. Comparison of the ratio of intensity of a given order to the first order $[I(n)/I(1)]$ to the theoretical ratio shows that the ratios increase with order. Not only is the absolute intensity greater than expected, but the higher orders (compared to the first order) are larger than expected. Lastly, the intensity for various crystal angle orientations and a fixed detector angle was measured.					
20 DISTRIBUTION/AVAILABILITY OF ABSTRACT <input checked="" type="checkbox"/> UNCLASSIFIED/UNLIMITED <input type="checkbox"/> SAME AS REP <input type="checkbox"/> DTIC USERS			21 ABSTRACT SECURITY CLASSIFICATION Unclassified		
22a NAME OF RESPONSIBLE INDIVIDUAL X.K. Maruyama			22b TELEPHONE (Include Area Code) (408) 646-2431		22c OFFICE SYMBOL PH/MX

T260091

Approved for public release; distribution is unlimited.

Enhanced Higher Order Parametric X-Radiation Production

by

Kay L. DiNova  
Lieutenant, United States Navy  
B.A., Rutgers College , 1983

Submitted in partial fulfillment  
of the requirements for the degree of

MASTER OF SCIENCE IN PHYSICS

from the

NAVAL POSTGRADUATE SCHOOL  
December 1992

## ABSTRACT

This thesis examines parametric x-radiation (PXR) which is the Bragg scattering of the virtual photons associated with the Coulomb field of relativistic charged particle from the atomic planes of a crystal. Higher order parametric x-radiation from the {002} planes of a thick mosaic graphite crystal have been observed. The raw PXR data was collected using a SiLi detector and a Pulse Height Analyzer (PHA) software program. The data was corrected for various effects including attenuation, detector drift and efficiency. The absolute number of photons per electron was obtained by using the fluorescent x-ray yield from a tin foil backing on the graphite crystal to determine the LINAC current. The number of photons per electron observed greatly exceeds the expected values. Comparison of the ratio of intensity of a given order to the first order  $[I(n)/I(1)]$  to the theoretical ratio shows that the ratios increase with order. Not only is the absolute intensity greater than expected, but the higher orders (compared to the first order) are larger than expected. Lastly, the intensity for various crystal angle orientations and a fixed detector angle was measured.

## TABLE OF CONTENTS

I. INTRODUCTION.....	1
II. THEORETICAL BACKGROUND.....	2
A. PARAMETRIC X-RAYS (PXR).....	2
B. MULTIPLE SCATTERING, BEAM DIVERGENCE AND MOSAICITY.....	8
C. EFFECTS OF FINITE APERTURE.....	9
III. PXR EXPERIMENTAL DESCRIPTION.....	13
A. ALIGNMENT AND ELECTRON BEAM STEERING.....	13
B. ELECTRONICS FOR SPECTROSCOPY.....	19
C. ENERGY CALIBRATION.....	21
IV. DATA AND ANALYSIS.....	22
A. SINGLE ANGLE EXPERIMENTS (FAR REGION, $\Delta\theta_X < \text{FWHM OF } J_2$ ).....	22
B. SINGLE ANGLE PXR ANALYSIS (FAR REGION).....	32
1. Detector Resolution at PXR Spectral Energies.....	43
2. PXR Bandwidth Determination.....	49
3. Calculations of Absolute PXR Yield (Photons/Electron).....	53
C. PXR DATA COLLECTION (DISPLACEMENT FROM THE BRAGG ANGLE).....	58
D. PXR ANALYSIS (DISPLACEMENT FROM THE BRAGG ANGLE).....	59
V. CONCLUSIONS AND RECOMMENDATIONS.....	85
APPENDIX A. FIGURES OF ROCKING DATA.....	87
APPENDIX B. ....	108
A. PROGRAM IN C.....	108
B. COMPUTER INTEGRATION PROGRAM EXAMPLE.....	109
LIST OF REFERENCES .....	112
INITIAL DISTRIBUTION LIST.....	114



## ACKNOWLEDGMENTS

I'd like to thank Professor X.K. Maruyama for his guidance, patience and his continuous striving for the best result. He constantly encouraged me to probe every detail and hence taught me invaluable lessons in data taking and analysis. Without his attention to detail this work could never have been completed.

Dr. Donald Rule and Dr. Ralph Fiorito deserve my special thanks for their extensive efforts developing and correcting the theory, in addition to their support and understanding of my numerous misconceptions. It is mostly due to the efforts of Dr. Fiorito that the final results presented here have been so thoroughly examined.

Mr. Don Snyder and Mr. Harold Riedtyk are surely overworked and under appreciated. I thank them for putting in those extra hours long into the night so I could obtain data, and without whom this thesis wouldn't have been possible.

I'd also like to thank Dr. John Hubbell and Dr. Steve Seltzer of the National Institute of Standards and Technology for information necessary to resolve attenuation and calibration issues.

Lastly, I thank my husband and two wonderful children for their support and encouragement. In appreciation this work is dedicated to them.



## I. INTRODUCTION

Parametric X-radiation (PXR) is the scattering of the virtual photons associated with the Coulomb field of a relativistic charged particle by the atomic planes of a crystal at or near the Bragg condition. It is monochromatic and spectrally intense. Potentially, PXR may be an important new X-ray source for a host of applications [Ref. 1]. Ter-Mikaelian (1972) first developed the theory of PXR as resonant radiation produced in a thin crystal [Ref. 2]. Later Feranchuck and Ivashin developed a theory for thick crystals. In 1985, the first experiment verifying this theory was performed by Baryshevsky et al at the Tomsk synchrotron [Ref. 3]. This experiment used a 900 MeV electron beam, bombarding a diamond crystal at a Bragg angle of 45 degrees producing x-rays in the 5 to 25 keV range.

The first experiments to observe PXR outside the USSR were conducted at the Naval Postgraduate School (NPS). [Ref. 2]. The first experiments were done with 20 $\mu$ m Si [Ref. 2], 44, 320  $\mu$ m Si [Ref. 4] and Carbon [Ref. 5].

This thesis is an in depth study of the enhancement of the higher order PXR due to the production and subsequent attenuation of x-rays in a thick mosaic carbon graphite crystal. This work presents measurements of absolute PXR production efficiency and the effects of experimental apertures on the bandwidth of PXR spectral line widths, and makes comparisons with calculations. Effects due to beam crystal alignment and due to limited detector aperture field of view have also been investigated. These crystals reveal greater relative production rates for the higher order x-rays than can be explained by target thickness effects. Furthermore, these measurements show that PXR production for all orders in a thick mosaic graphite crystal greatly exceed predictions from calculations based upon current theoretical understanding.



## II. THEORETICAL BACKGROUND

Parametric x-radiation (PXR) is one of several types of x-radiation that are produced by the interaction of a relativistic charged particle propagating in structured media. These include bremsstrahlung, transition radiation (TR), channeling radiation (CR) and Cherenkov radiation. These various mechanisms are discussed and compared in reference 6, which claims that PXR is the most effective source of quasi-monochromatic and focused x-rays, and reference 7 which compares PXR to synchrotron radiation.

### A. PARAMETRIC X-RAYS (PXR)

Parametric x-rays are produced when the electromagnetic field of the relativistic charged particle interacts with the periodic electric susceptibility associated with the crystal lattice structure. When the charged particle beam satisfies the Bragg condition with the crystal lattice, virtual photons are diffracted as real x-rays. [Ref. 2]

PXR is produced when the photon index of refraction  $n(\vec{k}, \omega)$  is greater than unity when the Bragg condition

$$\vec{k}^2 = (\vec{k}_B + \vec{\tau})^2, \quad (|\vec{k}| = |\vec{k}_B|) \quad (1)$$

is fulfilled, where  $\vec{\tau}$  is the reciprocal lattice vector,  $\vec{k}$  is the wave vector of the emitted photon, and  $\omega$  is its frequency. This condition is illustrated in Figure 1. As a result, the condition for Vavilov-Cherenkov radiation

$$1 - \frac{\vec{k} \cdot \vec{v}}{\omega} n(\vec{k}, \omega) = 0, \quad (\hbar = c = 1) \quad (2)$$

is satisfied in a crystal. This is in contrast to a homogeneous medium, where the index of refraction is less than unity for x-rays, and Vavilov-Cherenkov radiation is not produced. Therefore, PXR is simply Vavilov-Cherenkov radiation produced by diffraction according to equation (1). [Ref. 8]

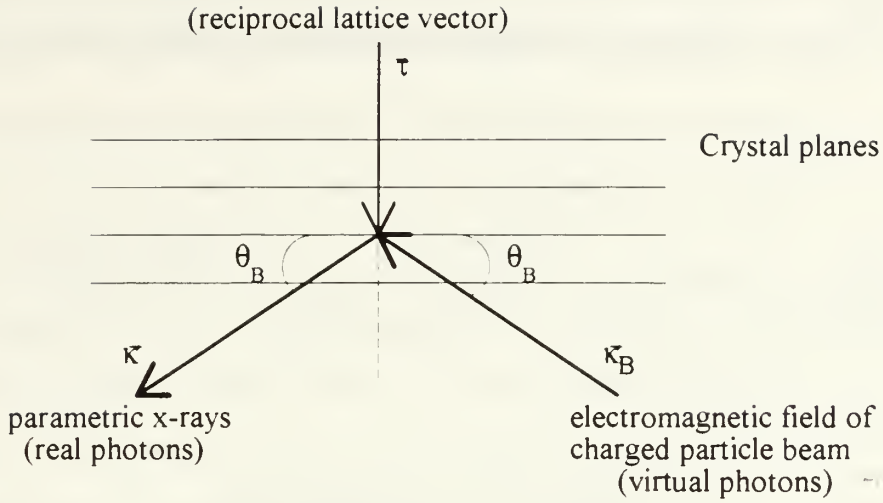


Figure 1. Diffraction of virtual photons associated with the charged particle beam by the atomic planes of the crystal showing the Bragg angle as the angle between the charged particle beam and the crystal planes. [Ref. 2]

There are two ways to treat the diffraction of real and virtual x-rays: 1) dynamic theory and 2) kinematic theory. The first case is realized in ideal crystals of thickness  $L$ , greater than the X-ray extinction length. On the other hand, the kinematic theory of PXR is applicable for real crystals, which consist of thin mosaic blocks turned relative to each other at an angle  $\delta > m/E$ , where  $m$  is the mass of the charged particle and  $E$  is its energy. The kinematic diffraction is more convenient for the experimental observation of PXR and it can be most easily analyzed because the angular and spectral distributions of PXR are essentially simplified and have a universal form for different crystals. [Ref. 8]

Ter-Mikaelian formulated the expression for the number of photons emitted by a charged particle in a thin crystal; treating the interaction as a perturbation, with the crystal requirement

$$\kappa L |n - 1| < 1, \quad (3)$$

where  $L$  is the effective thickness of the crystal. If the refraction of photons and the multiple scattering of the electrons in the crystal are taken into account, then the results,

for a mosaic crystal with  $\delta > m/E$  and with PXR from different blocks being coherent, remain correct. The spectral and angular distributions of emitted photons are formulated by

$$\frac{\partial^2 N}{\partial n_{\perp} \partial \omega} = \frac{e^2}{2\pi} \omega L_a |\mathbf{g}_{\tau}|^2 \frac{|\kappa_{\perp}, \omega v + \tau|^2}{\left[ (\kappa_{\perp} - \tau_{\perp})^2 + \frac{\omega^2}{v^2} (1 - v^2) \right]^2} \left[ 1 - \exp\left(-\frac{L}{L_a}\right) \right] \delta(q), \quad (4)$$

$$q = \frac{\omega}{v} - \sqrt{\omega^2 - \kappa^2} + \tau_z - \frac{\omega}{2} [\text{Re}(\mathbf{g}_0) - \theta_s]. \quad (5)$$

Here  $\mathbf{g}_{\tau}$  and  $\mathbf{g}_0$  are the Fourier components of the dielectric susceptibility parallel and perpendicular to the reciprocal lattice vector. These values are directly related to the coherent scattering amplitude of the photons by the atoms of the crystal.  $\theta_s$  is the angle of multiple scattering. Equation (4) is written in a coordinate system with the z-axis directed along the particle velocity  $\vec{v}$ ;  $\kappa_{\perp} = \omega n_{\perp}$ ; and  $L_a = [\omega \text{Im}(\mathbf{g}_0)]^{-1}$ . [Ref. 8] The differential radiation cross section for PXR as derived by Feranchuck and Ivashin can also be written in terms of angular displacements from the Bragg angle instead of  $n_{\perp}$  as:

$$\frac{\partial^2 N}{\partial \theta_x \partial \theta_y \partial \omega} = \frac{1}{2\pi^2} \frac{e^2}{\hbar c} \frac{1}{\omega_B} |\mathbf{g}_{\tau}|^2 \frac{\theta_x^2 \cos^2(2\theta_B) + \theta_y^2}{(\gamma^{-2} + \theta_x^2 + \theta_y^2 + |\mathbf{g}_0|)} \frac{1}{16 \sin^4 \theta_B \left( \frac{\theta_x}{\tan \theta_B} - \frac{\Delta \omega}{\omega_B} \right)^2 + \rho_s^2}, \quad (6)$$

where  $\mathbf{g}_0 = n(\omega) - 1 = \frac{1}{2} \left( \frac{\omega_p}{\omega} \right)^2 \frac{f_1(\sin \theta / \lambda)}{Z}$ ,  $n(\omega)$  is the index of refraction,  $\omega_p$  is the plasma

frequency,  $\theta_{x,y} = \frac{(\vec{\kappa} - \vec{\kappa}_B)_{x,y}}{\omega_B}$ , where  $\theta_x, \theta_y$  are the angular displacements away from the



Bragg angle in and out of the incident plane respectively,  $|\mathbf{g}_\tau| = \left| \frac{4r_e\lambda^2}{\pi V} f_1 \left( \frac{\sin \theta}{\lambda} \right) \right|$ ,  $f_1$  is the x-ray scattering factor of the crystal,  $V$  is the volume of the unit cell of the crystal,  $r_e$  is the classical electron radius,  $\hbar=c=1$ ,  $\rho_s = \lambda / (L_a(\omega)2\pi)$  and  $L_a(\omega)$  is the photon absorption length. [Ref. 8]

The characteristic quasi monochromatic photons produced at large angles relative to the charged particle's velocity vector,  $\bar{\mathbf{v}}$ , distinguishes PXR from other radiation mechanisms. The particle energy does not determine the emitted photon's wave vector,  $\bar{\mathbf{k}}$ , nor frequency  $\omega_B$ . The emitted photon's wave vector depends upon the reciprocal lattice vector,  $\bar{\boldsymbol{\tau}}$ , the velocity vector of the electron and the Bragg frequency. The Bragg angle,  $\theta_B$ , is the angle between the velocity vector,  $\bar{\mathbf{v}}$  and the crystallographic planes associated with the reciprocal lattice vector  $\bar{\boldsymbol{\tau}}$ . The PXR maxima are defined by the crystal lattice structure amplitudes corresponding to  $\bar{\boldsymbol{\tau}}$ . The values of the emitted wave vectors,  $\bar{\mathbf{k}}$ , and frequencies  $\omega_B$  are

$$\bar{\mathbf{k}} = \omega_B \bar{\mathbf{v}} + \bar{\boldsymbol{\tau}}; \quad \bar{\mathbf{k}} \cdot \bar{\mathbf{v}} = 2\theta_B, \quad (7)$$

$$\omega_B(n) = \frac{\tau^2}{2|\tau_z|} = \frac{|\tau|}{2\sin\theta_B} = \frac{n\pi c}{d\sin\theta_B}, \quad n=1,2,3\dots \quad (8)$$

where  $d$  is the distance between the crystal planes corresponding to the vector  $\bar{\boldsymbol{\tau}}$ . [Ref. 3.]

The intensity of PXR is proportional to  $|\mathbf{g}_\tau|^2$  and is greater in crystals with higher packing factors, such as a diamond lattice. Rotation of a crystal by some  $\Delta\theta$  results in the emitted wave vector,  $\bar{\mathbf{k}}$ , rotating  $2\Delta\theta$  in the same direction while the frequency varies as a result of equation (7). The angular distribution of emitted photons can be derived by integrating equations (4) or (6) over  $\omega$ , resulting in

$$\frac{\partial^2 N}{\partial\theta_x\partial\theta_y} = \sum_{n=1}^{\infty} \frac{e^2}{4\pi} \frac{\omega_B}{c} L_a \left[ 1 - \exp\left(-\frac{L}{L_a}\right) \right] \frac{|\mathbf{g}_\tau(\omega_B)|^2}{\sin^2\theta_B} \cdot \frac{[\theta_x^2 \cos^2 2\theta_B + \theta_y^2]}{[\theta_x^2 + \theta_y^2 + \theta_{ph}^2]^2}; \quad (9)$$

$$\theta_{ph}^2 = \frac{m^2}{E^2} + \theta_s^2 + |\mathbf{g}_0|, \quad (10)$$

$$\theta_s^2 = \theta_{mult\ scat}^2 + \theta_{beam-div}^2 + \theta_{mos}^2, \quad (11)$$

where  $m$  is the rest mass of the electron,  $L_a$  is the absorption coefficient which is a function of  $\omega$  and  $\theta_{ph}$  is the characteristic angular spread of the PXR.  $\theta_s$  includes the effects of multiple scattering of the beam electrons, electron beam divergence and crystal mosaicity. This can be put in dimensionless form by means of the normalized amplitude  $J = N/N_0$  and angles  $x, y \equiv \theta_{x,y}/\theta_{ph}$ :

$$\frac{\partial^2 N}{\partial x \partial y} = N_0 J(x, y); \quad J(x, y) = \frac{x^2 \cos^2 2\theta_B + y^2}{(x^2 + y^2 + 1)^2}; \quad (12)$$

$$N_0 = \sum_{n=1}^{\infty} \frac{e^2}{4\pi} \frac{\omega_B}{c} L_a \left[ 1 - \exp\left(-\frac{L}{L_a}\right) \right] \frac{|\mathbf{g}_\tau(\omega_B)|^2}{\sin^2 \theta_B}. \quad (13)$$

The number of photons detected in an angular width of  $\theta_D$  about  $\theta_B$  is obtained by integrating equation 9:

$$N_D = \pi N_0 (1 + \cos^2 2\theta_B) \int_0^{\rho_D} \frac{\rho^3}{(\rho^2 + 1)} d\rho, \quad (14)$$

$$N_D = N_1 (1 + \cos^2 2\theta_B) \left\{ \ln \frac{\dot{\theta}_D^2 + \theta_{ph}^2}{\theta_{ph}^2} - \frac{\theta_D^2}{\theta_D^2 + \theta_{ph}^2} \right\}, \quad (15)$$

where  $\rho_D = \frac{\theta_D}{\theta_{ph}}$ . The detector angular size is a factor in determining the value of  $N_D$ , even for  $\theta_D \ll \theta_{ph}$ . This factor does not occur in channeling or in bremsstrahlung radiation; however in PXR, the intensity slowly decreases inversely proportional to  $\theta$  as  $\theta$  increases. [Ref. 8]

According to equations (14) and (15), there is no threshold characteristics in the PXR intensity. The angular frequency, however, depends on  $\theta_{ph}(E)$  which increases with the electron energy

$$E < E_{opt} = \sqrt{\frac{m^2 + \theta_s^2}{|\mathbf{g}_0|}}, \quad (16)$$

in accordance with equation (9) and (10), thus setting the limiting threshold energy for PXR. The number of photons decreases rapidly for  $E < E_{opt}$ . The number detected becomes

$$N_D \cong \frac{\pi}{2} N_0 (1 + \cos^2 2\theta_B) \frac{1}{2} \left( \frac{\theta_d}{\theta_{ph}} \right)^4 \sim \left( \frac{E}{E_{opt}} \right)^4. \quad (17)$$

This phenomena suggests that if the beam energy is not sufficient, regardless of whether all the other parameter conditions are met, PXR may not be observed. [Ref. 8].

Integration of equations (4) or (6) over  $n_{\perp}$  or  $d\Omega$  respectively results in the frequency distribution,

$$\frac{\partial N}{\partial u} = N_1 J_1(\mathbf{u}); \quad J_1(\mathbf{u}) = \frac{1 + \mathbf{u}^2 (1 + \cos^2 2\theta_B)}{(1 + \mathbf{u}^2)^{3/2}}; \quad (18)$$

$$N_1 = \frac{\pi}{2} N_0; \quad \mathbf{u} = \tan \theta_B \frac{(\omega - \omega_B)}{\omega_B \theta_{ph}}. \quad (19)$$

Equation (18) can be put in terms of frequency by using the chain rule  $\frac{\partial N}{\partial \omega} = \frac{\partial N}{\partial u} \frac{\partial u}{\partial \omega}$ , and

$\frac{\partial u}{\partial \omega}$  can be determined using equation (19). Although equations (18) and (19) do not apply to real experiments with finite aperture, they have been previously applied to the experimental results. [Ref. 8]



## B. MULTIPLE SCATTERING, BEAM DIVERGENCE AND MOSAICITY

In reference 1, the Adischev et. al. have used

$$\theta_{M.S.} = \frac{E_s}{E} \sqrt{\frac{L}{L_R}}, \quad (20)$$

$E_s \approx 21$  MeV,  $L$  is the effective thickness of the crystal and  $L_R$  is the radiation length. This value is an approximation applicable to very high energy electrons and is well known to over estimate the multiple scattering effect. [Ref. 9] The Bethe-Ashkin formula for multiple scattering which gives a more accurate estimate for  $\theta_{M.S.}^2$  is used in the analysis and is given by;

$$\langle \theta_{M.S.}^2 \rangle = k \log \left[ 1.13 \cdot 10^{-4} Z^{4/3} z^2 A^{-1} t \right], \quad \theta_l^2 = k \equiv 0.157 \frac{Z(Z+1)z^2}{A} \frac{t}{(pv)^2}, \quad (21)$$

where  $Z$  is the atomic number,  $A$  is the atomic weight and  $t$  is the thickness of the foil in grams per square centimeter. The charge of the scattered particle is  $z$ ,  $p$  is its momentum and  $v$  its velocity,  $\langle \theta^2 \rangle$  is an average scattering angle value obtained by integrating over angle, where  $\theta_l$  is the maximum angle used in the analysis. It is estimated as the angle for which there is, on the average throughout the full thickness  $t$  of the foil, only one collision with  $\theta > \theta_l$ . [Ref. 11]

Since x-rays are produced throughout the electron's path length, the amount of multiple scattering varies from zero to the value appropriate for the full path length of the electron in the crystal. Additionally, the x-rays which are generated inside the crystal are attenuated due to absorption. Thus there is a weighting of x-rays reaching the detector, with the weighting factor equal to  $e^{-\mu x}$ , where  $\mu$  is the absorption coefficient for the particular x-ray energy. Therefore, x-rays produced near the front face of the crystal are weighted more than those near the back surface. This weighting effectively biases the detected x-rays toward those produced at lower values of  $x$ , i.e. near the front face of the crystal where the multiple scattering is lowest. The proper way to account for the effects

of multiple scattering would be to add up all the x-rays produced as a function of  $x$ , including an  $x$  dependent multiple scattering effect.

For simplicity, a mean value of  $\langle \theta_{M.S.}^2 \rangle$  can be calculated by weighting the value of  $\langle \theta^2 \rangle$  with the absorption attenuation of x-rays,  $e^{-\mu x}$ . The mean value for  $x$  is defined as follows

$$\langle x \rangle \equiv \frac{\int_0^L x e^{-\mu x} dx}{\int_0^L e^{-\mu x} dx}. \quad (22)$$

[Ref. 9] Since the Bethe-Ashkin formula for  $\langle \theta_{M.S.}^2 \rangle$  to first order is proportional to  $x$ , this value for  $x$  is used in equation (21) in place of the crystal thickness,  $t$ , to determine the multiple scattering angle  $\theta_s$  [Ref. 11]. In our treatment, the effect of the divergence of the electron beam is not included. To more rigorously include the effect of beam divergence on the x-ray angular distribution and bandwidth, the electron beam angular distribution must be convolved with the angular distribution of the x-ray production as has been done e.g. in the case of transition radiation [Ref. 12]. For simplicity of calculation the effect of divergence was not included in the analysis since the effective beam divergence of the NPS LINAC ( $<1$  mrad) is unimportant.

### C. EFFECTS OF FINITE APERTURE

Previous PXR experiments to date have compared the experimental data with the results of equation (18). However, the theoretical values obtained by using equation (18) refer to an unrealistic idealization i.e., an infinite detector aperture, which does not approximate the real conditions of these experiments and neglect the effect of the aperture on the PXR spectrum.

In order to calculate the spectral distribution for real experimental conditions, equation (15) should be integrated over the appropriate angular field of view as determined by the detector size and the distance from the crystal to the detector. The integration limits  $\bar{\theta}_x$

and  $\bar{\theta}_y$  are set by the angular fields of view in and out of the plane of observation ( $\Delta\theta_x = 2\bar{\theta}_x$  and  $\Delta\theta_y = 2\bar{\theta}_y$  respectively). [Ref. 13]

Case I. Infinite  $\bar{\theta}_x$ , finite  $\bar{\theta}_y$ . Integrating equation (7) first over  $\theta_y$  with a finite upper limit of  $\bar{\theta}_y$  and then integrating  $\theta_x$  from 0 to  $\infty$  results in

$$\frac{\partial N}{\partial \omega} = 2 \left( \frac{e^2}{\hbar c} \right) \frac{|\chi_{10}|^2}{(4 \sin \theta_B \cos \theta_B)} \frac{L_a \left( 1 - e^{-\frac{L}{L_a}} \right)}{\lambda \theta_{ph} \omega} J_2(u), \quad (23)$$

where the function  $J_2$  is defined as;

$$J_2(u) = \cos^2(2\theta_B) u^2 \left[ \frac{\alpha_y}{1+u^2} \frac{1}{\alpha_y^2 + 1 + u^2} + \tan^{-1} \left( \frac{\alpha_y}{(1+u^2)^{1/2}} \right) \frac{1}{(1+u^2)^{3/2}} \right] \\ + \left[ \tan^{-1} \left( \frac{\alpha_y}{(1+u^2)^{1/2}} \right) \frac{1}{(1+u^2)^{1/2}} - \frac{\alpha_y}{(\alpha_y^2 + 1 + u^2)} \right] \quad (24)$$

and  $\alpha_y = \frac{\theta_y}{\theta_{ph}}$ . This is derived by using a delta function approximation for the x dependence, see equation 6. [Ref. 9]

Case II.  $\bar{\theta}_x$  and  $\bar{\theta}_y$  both finite. In this case there are two regimes. a) The first is the narrow line limit regime in which  $\rho_s \approx \Delta\theta_x$ , then

$$\frac{\partial N}{\partial \omega} \propto \frac{\left( \frac{\rho_s}{2} \right)^2}{(\theta_x - \theta_B)^2 + \left( \frac{\rho_s}{2} \right)^2} \quad (25)$$

b) The second is the aperture limited bandwidth regime for which the delta function approximation is still correct if  $\Delta\theta_x \gg \rho_s$ . Then:

$$\frac{\partial N}{\partial \omega} \propto \begin{cases} \Delta\theta_x J_2(u), & -\bar{\theta}_x < \theta_x < \bar{\theta}_x \\ 0, & \theta_x \notin (-\bar{\theta}_x, \bar{\theta}_x) \end{cases} \quad (26)$$



In this case the energy bandwidth is determined based on the relative value of  $\Delta\theta_x$  and the full width at half maximum (FWHM) of  $J_2(u)$ . If  $\Delta\theta_x$  is larger than the FWHM of  $J_2(u)$ , then the bandwidth is determined to be the FWHM of  $J_2(u)$ . This region is referred to later in this thesis as the "near region". If  $\Delta\theta_x$  is smaller than the FWHM of  $J_2(u)$ , then the bandwidth is proportional to  $\Delta\theta_x$  and is relatively insensitive to the form of  $J_2(u)$ . This regime is called the small aperture regime referred to later in this thesis as the "far region". The bandwidth for the small aperture regime is:

$$\Delta\omega = \frac{\Delta\theta_x \omega}{\tan(\theta_B)} \quad (27)$$

It is the small aperture regime that applies to this thesis work and that is most applicable to previous PXR experiments [Ref. 10]. Figures 2 and 3 illustrate the function  $J_2(u)$  with  $\Delta\theta_x < \text{FWHM of } J_2(u)$  for the far region and  $\Delta\theta_x > \text{FWHM of } J_2(u)$  for the near region respectively.

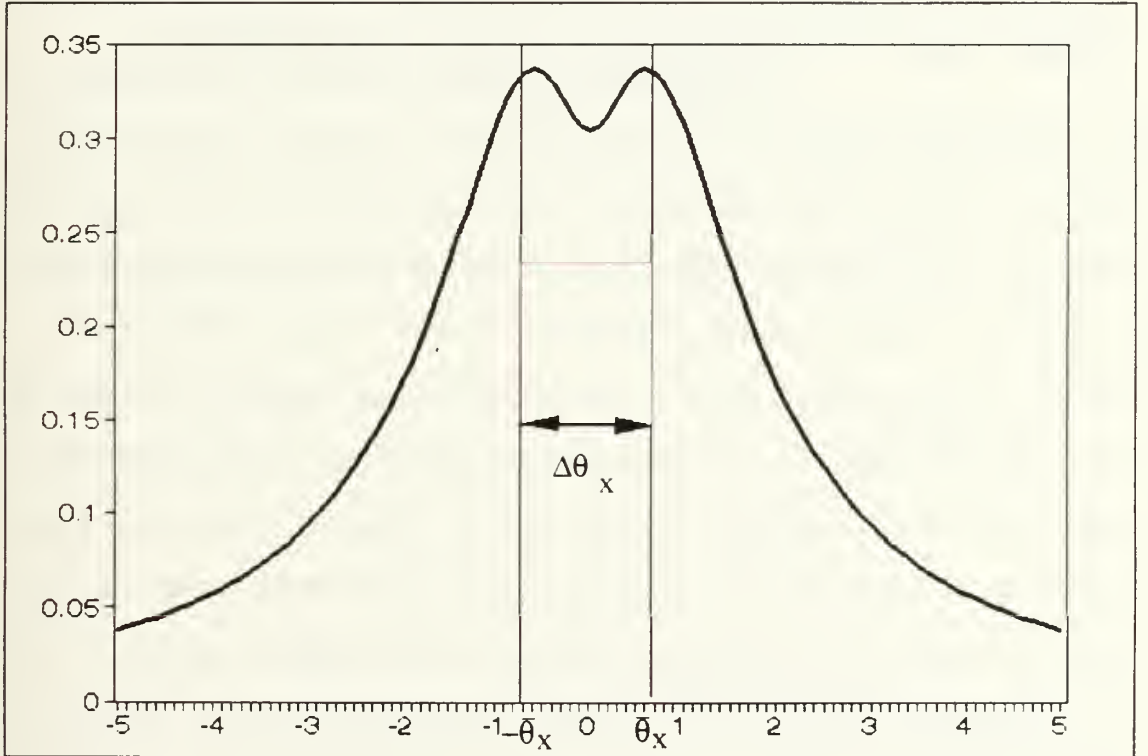


Figure 2.  $J_2$  and the field of view for the "far region" at the Bragg angle.

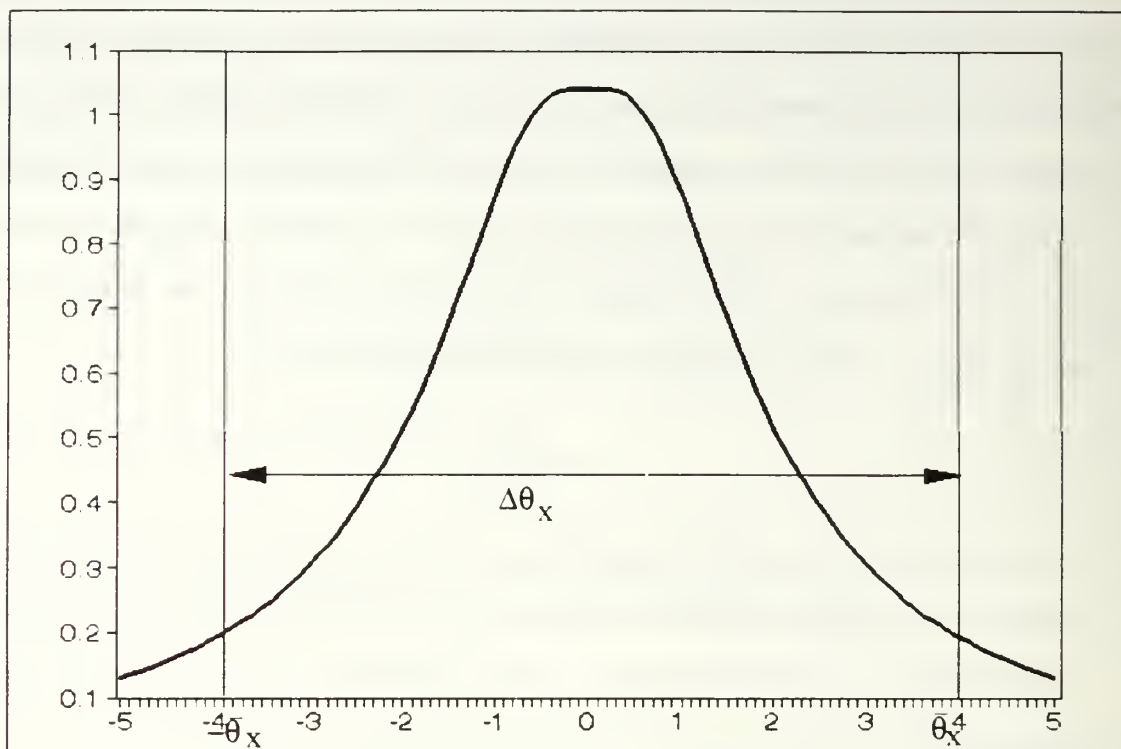


Figure 3.  $J_2$  and the field of view for the "near region" at the Bragg angle.

### III. PXR EXPERIMENTAL DESCRIPTION

Several PXR experiments were conducted using a  $1.39 \pm 0.01$  mm thick graphite crystal in Bragg geometry. The x-ray observation angle was set at 45 degrees with respect to the electron beam direction. In this configuration, corresponding to a Bragg angle of 22.5 degrees with respect to the {002} atomic planes of the carbon mosaic crystal, measurements were made at detectors placed at 100 cm. and 29 cm. from the target to observe the effects of changing the solid angle of observation. At both these configurations, "rocking data" measurements were made. "Rocking data" were obtained by rotating the crystal about the nominal Bragg angle of 22.5 degrees. The rocking data provided the dependence of the absolute and relative intensities of the various order x-rays when the Bragg condition was not exactly satisfied.

#### A. ALIGNMENT AND ELECTRON BEAM STEERING

The NPS Linear Accelerator (LINAC) was used to conduct these experiments. The beam energy varied with each experiment with a nominal electron energy of 90 MeV. Two different SiLi detectors [Ref. 14 & 15] were used in these experiments. The first was an EG&G ORTEC model 7113-16250 with an active detector region of  $200 \text{ mm}^2$ , and the other was a Canberra model SI200250 with an active detector region of  $200 \text{ mm}^2$ . The SiLi detectors have nominal time resolution times of  $12 \text{ } \mu\text{sec}$  determined by the pulse shaping preamplifier. Because the LINAC is pulsed at 60 Hz with a macro structure length of  $1 \text{ } \mu\text{sec}$ , the system is count rate limited. The LINAC duty cycle makes the count rate 60 MHz when a single photon is detected during each LINAC pulse. The LINAC was adjusted to limit the macroscopic average count rate including background to one count per three to five machine macropulses in the whole detector energy range. Consequently, the LINAC beam was limited to a dark current estimated to be of the order

of  $2 \times 10^{-13}$  amps. Dark current refers to using the LINAC with zero gun grid voltage, so that only stray electrons are accelerated. The ratio of counts per machine pulse was determined by use of fluorescent foils to prevent the double counting of photons by the detector. That is, if two photons are stopped in the detector simultaneously (within the peak shaping time of the detector) these two photons will appear as a single photon with an energy equivalent to the sum of the two coincident photons. Pulse pile up was of critical concern in this experiment because two first order PXR photons observed simultaneously would register as a second order PXR photons at double the energy. This would falsely enhance the higher orders as well as reduce the first order, resulting in ratios of intensity of higher order peaks to first order peaks too high. Maintaining a constant dark current was difficult to achieve and required constant operator attention.

The experimental setup is shown in Figure 4. The beam is shown entering a vacuum chamber from the left at the entrance port. At the center of the chamber is a target ladder which can be remotely rotated, raised, lowered and tilted. An alignment-reference laser is located outside the port located 90 degrees counter clockwise from the entrance port. The detector is located 45 degrees clockwise from the beam exit port or 135 degrees counter clockwise from the entrance port. To help align the electron beam a phosphorescent screen was placed at the end of a 27.5 in. pipe located at the beam exit port.

Experiments prior to July 22 1992 were conducted using an EG&G ORTEC Si(Li) x-ray detector model number 7113-16250. Due to the fixed height of the target chamber and the detector's large liquid nitrogen tank located below the detector window the detector couldn't be placed closer than about two feet from the chamber. For experiments with this detector a copper vacuum pipe 27.5 in. long was placed at this port fitted with a one mil Kapton window (1 in. diameter). The results obtained from these experiments will be referred to as the far case or the far region. Experiments on or after July 22<sup>nd</sup>



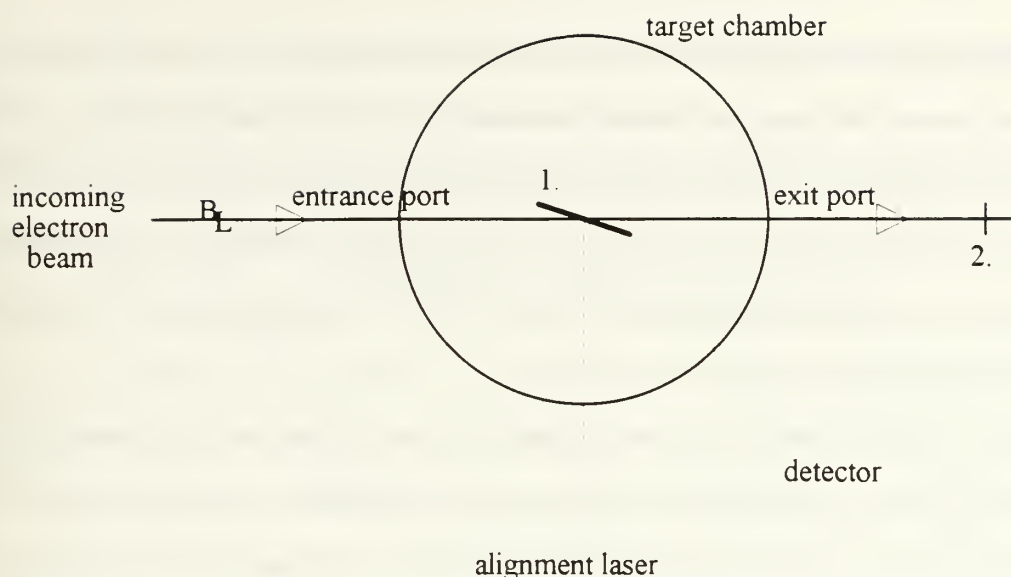


Figure 4. PXR experimental setup in the LINAC end station, showing incoming charged particle beam and beam line, alignment-reference laser, detector, and entrance and exit ports. 1. Target ladder with calibration foil, mirror, and carbon crystal. 2. downstream phosphorescent screen.

were conducted using a Canberra Si(Li) x-ray detector model number SI200250. This detector consist of a two fill and vent port dewar to allow operation at any orientation and a "slim-line" detector chamber which is small in size and weight. [Ref. 14] This detector has a much smaller horizontally mounted liquid nitrogen tank and could be positioned directly next to the vacuum chamber. The vacuum chamber port was fitted with the same one mil Kapton window that covered the copper pipe. The results obtained from these experiments will be referred to as the near case or near region.

A remotely vertically positionable ladder and 2 axis goniometer were used to hold and orient the mosaic carbon crystal used in this experiment. The crystal used in all the experiments is a mosaic graphite monochromator measured to be  $1.39 \pm 0.01$  mm. thick. manufactured by Union Carbide. The density of the crystal is  $2.260 \pm 0.005$  grams per cubic centimeter. The spacing of the reflecting  $\{002\}$  planes is  $3.356 \pm 0.003$  angstroms. The mosaic spread is  $\geq 0.4$  degrees. [Ref. 16] (Pure crystals (mosaic spread = 0) such as Si have lower reflectivity than mosaic crystals in normal x-ray diffraction and therefore, a higher the mosaic spread results in a theoretically higher measured intensity.) On June 5<sup>th</sup>

half of the crystal was covered with a 0.0275 mm thick layer of tin  $7.31 \text{ g/cm}^3$  on the back face of the crystal. This foil was essential as a calibration source. From the location of the  $K_{\alpha}$  fluorescence line, the energy stability and energy calibration of the detector throughout the experiment could be monitored. The observed yield of photons is proportional to the integrated electron current through the foil. This information was used to determine the absolute photon production rate. [Ref. 17]

The ladder which housed the mosaic graphite crystal also contained three separate foils, copper (Cu), yttrium (Y) and indium (In), which were replaced on June 5<sup>th</sup> by a sandwich foil consisting of a titanium (Ti) foil 0.0164 mm. thick, a yttrium (Y) foil 0.0603 mm. thick, and a tin (Sn) foil 0.0275 mm. thick. These foils were used for energy calibration purposes and to determine the LINAC beam current. (The details of this calculation are presented in reference 17.) The ladder also contained a phosphorescent screen with a pin hole in the center which was used to position the electron beam. The target ladder also contained a mirror, coplanar with the crystal face which was used to reflect a reference laser back onto itself to establish the zero degrees or "home" position.

The reference laser was used to establish the orientation and position of the crystal with respect to the electron beam. Using cutouts with a pinhole in the center to cover the ports, the laser was adjusted so that it went through the geometric center of the chamber. The ladder was then placed in the center of the chamber with the motor controls attached and the pinhole set to the position of the laser beam. The ladder was manually adjusted for tilt so that the laser went through the pinhole in the center of the phosphorescent screen, and remained on the pinhole upon 360 degree rotation of the crystal. A mirror and the graphite were positioned so that their faces were coplanar and such that the rotation axis of the ladder was in their planes as well. Then, by setting the mirror at 45 degrees with respect to the laser beam, the laser beam was reflected down the exit pipe. A second phosphorescent screen was placed at the end of the exit pipe with the center of the screen location based on the location of the reflected laser. This second screen greatly improved

the alignment of the experiment. It was determined that the position of the center of the screen was not identically at the geometric center of the pipe. After the first data were obtained, using this screen, the screen slipped, and could not be replaced exactly without breaking vacuum and re-configuring it. The screen was replaced with its center near the geometric center of the pipe, which introduced a slight additional uncertainty in the crystal angle of less than two tenths of a degree. For this reason, in future experiments, OTR should be used on a downstream foil as an alignment as was first done with Si. [Ref. 4]

After the chamber was sealed and a vacuum was established the LINAC was then tuned to the given energy, and a beam was established. The beam was adjusted so that it went through the center of the quadrupole magnets, so that adjustments in klystron frequency and phase during the experiment would not affect the location of the beam. Using end station steering magnets, the beam was steered so that it went through the pin hole located on the screen on the ladder. Since the only means of steering without changing the position of the beam through the quadrupole magnets is end station steering (see Figure 5) a compromise had to be made to get the beam through both the center of the screen on the ladder and through the center of the downstream screen. Additionally, the beam's focus required a compromise. Focusing downstream leads to a more parallel beam at the target, but it also makes a larger beam spot. Focusing on the target gives a smaller beam spot, but the beam electrons are not parallel. The beam was focused approximately half way between the two screens based on these two factors. This uncertainty however, contributes to the uncertainty in the crystal angle with respect to the beam line of less than one tenth of a degree.

Once the beam was focused and the steering adjusted, the electron gun was turned off and the current was reduced to dark current. The ladder's angle was adjusted using the laser since the electron beam's position is known relative to the laser. Refer to Figure 6.

The angle  $\theta_C$ , for positioning the crystal is determined with respect to the reference laser.  $\theta_C$  is the angle by which the crystal was rotated and was equal to  $\theta_B$  or  $\theta_B + 180$

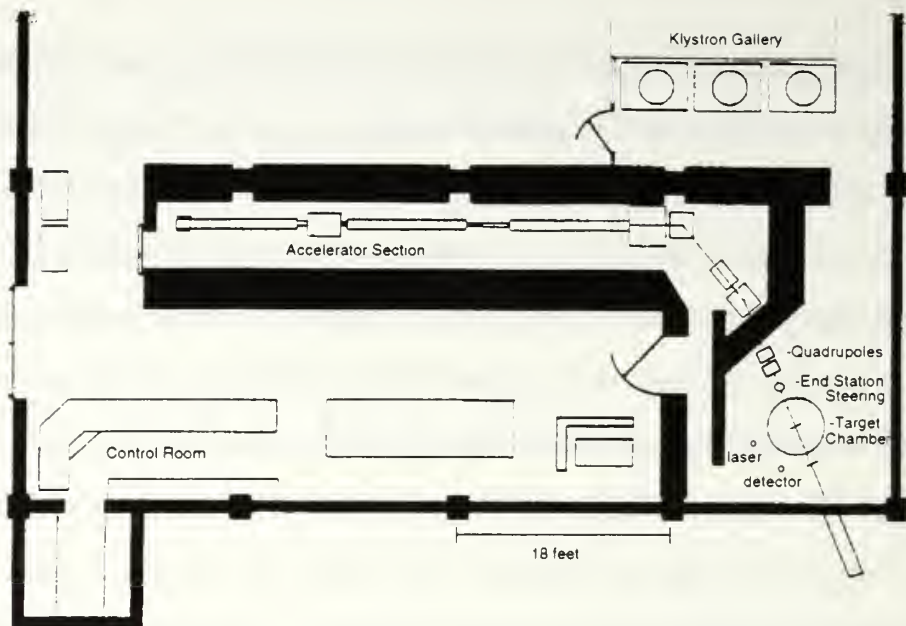


Figure 5. Naval Postgraduate School 100 MeV Linear Accelerator (LINAC) showing klystrons, quadrupole magnets and end station steering magnets.

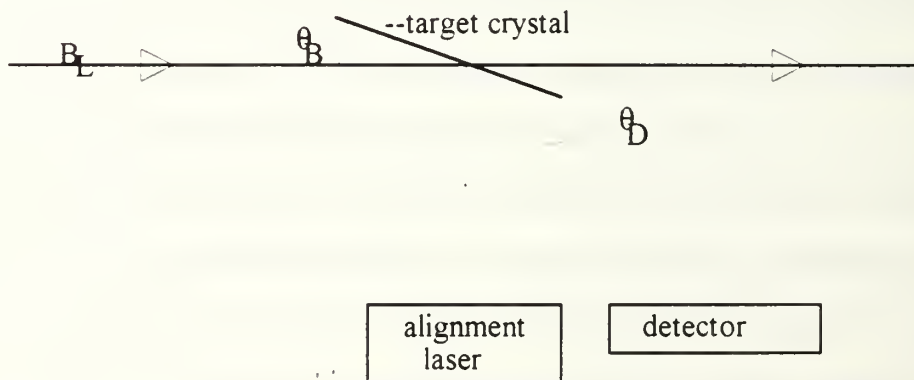


Figure 6. The relationship between the incoming particle beam and the ladder,  $\theta_B$ , and between the beam and the detector  $\theta_D$  which is fixed at 45 degrees.

degrees. The home or zero degrees position was established by using a mirror on the ladder. When the ladder is oriented at zero degrees with respect to the laser, the beam is reflected back onto the laser. Using a remote camera the "home" or zero position is established and fine adjusted after every rotation of the crystal. This gives a more consistent angle and also removes the backlash inherent in the motor controls. With



reference to the laser the electron beam enters the chamber at 90 degrees. The target crystal orientation for these experiments varied with respect to the beam line while the detector angle was fixed at 45 degrees.

## **B. ELECTRONICS FOR SPECTROSCOPY**

Because the end station is relatively exposed to the klystron gallery (see Figure 5) the SiLi detectors are susceptible to ground loops and radiated noise from the klystrons. Consequently great effort was taken to insure sufficient grounding and shielding to suppress the noise pulse. In addition a gating system was set up. Figure 7 is a block diagram of the electronics setup. The signal is received by either SiLi detector. It is amplified by an ORTEC Amp 571 pre-amplifier and an ORTEC 450 amplifier which was replaced on May 8<sup>th</sup> by a TENNELEC TC 244 amplifier. It is passed through an ORTEC 426 linear gate with a gate width of 5 microseconds. This gate was replaced in later experiments with a TENNELEC TC 304 linear gate which has wider gating capabilities. The gate is triggered by a Stanford Research System Inc. model DG535 four channel digital delay/pulse generator. The detector and preamplifier were located in the LINAC end station. To allow for possible changes in settings the remaining components were located in the control room. This resulted initially in a noise problem that was eliminated by trial and error, using grounding straps and a return signal from the amplifier in the control room to an oscilloscope in the end station. The delay generator delay time ( $T_d$ ) is adjusted with respect to  $T_0$ , the machine's start sequence time. The delay time is adjusted so that the start of the gate coincides approximately with the apparent arrival of the beam pulse at the ladder in the chamber. The ideal delay time,  $T_d$  for the gating was determined by using an oscilloscope along with the pulse height analyzer and the fluorescent signal from a copper foil.  $T_d$  was determined to be the time at which the maximum signal was observed. Shorter and longer delay times gave no signal. The maximum was found to be

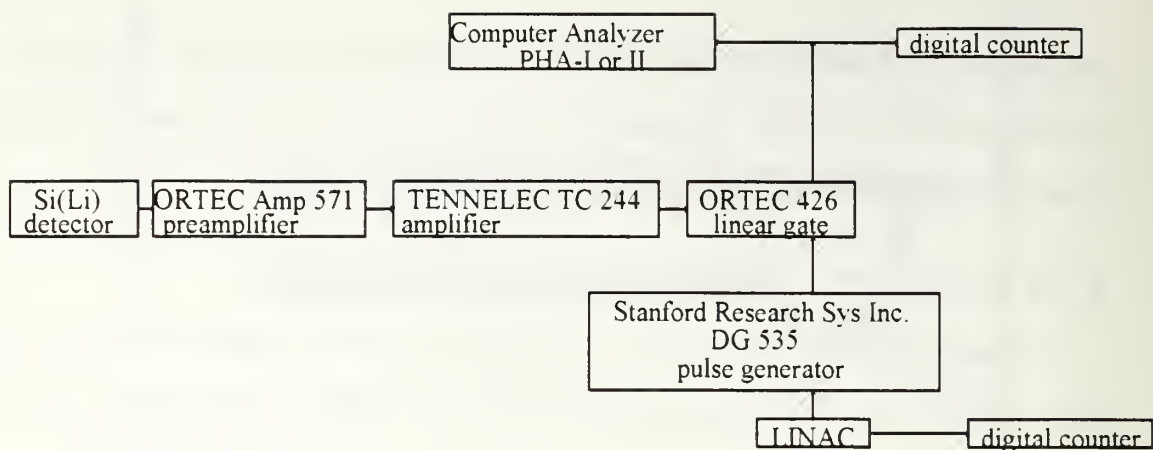


Figure 7. Electronic setup.

6  $\mu$ s, for the earlier experiments using the ORTEC amplifier, and 30.6  $\mu$ s for the TENNELEC amplifier.

The LINAC generates 60 pulses of one microsecond duration every second. Since x rays are only produced during the actual pulse time this gating doesn't affect the PXR spectrum or the sandwich foil calibration spectrum, other than by limiting the noise that is non-coincident with PXR production. The gating limits detection to the on-time of the LINAC pulse. However klystron RF noise adds a bias to the pulse signal energy calibration which tends to be non-random with respect to  $T_0$  hence shifting the energy calibration compared to that obtained using radioactive sources. Since the PHA determines the energy (or channel) based on the energy deposited in the active detector region at a given time and if the x ray arrives during a consistently negative klystron noise the PHA determines the energy of the x ray to be lower than it is. The klystron noise was typically in the negative voltage portion during the gating (see Figure 8). The negative voltage adds to the positive voltage produced by the detected x-rays. This lowers the output voltage. The net effect is a lower pulse height, which is interpreted by the pulse height analyzer as a lower energy photon. Therefore the calibration must be obtained during the same portion of the machine cycle as the PXR spectrum to get the same klystron noise effect for both PXR and calibration x rays. For radioactive sources gating

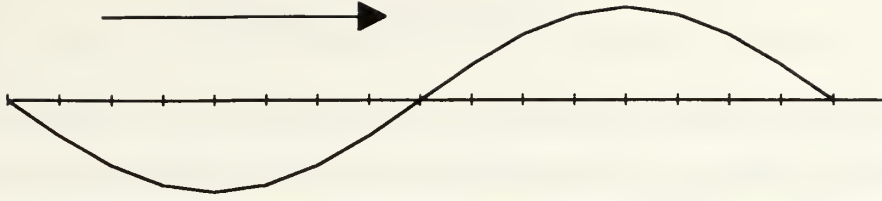


Figure 8. Typical shape of klystron noise during PXR data collection. The arrow indicates approximate gating portion.

effectively eliminates the signal. Without gating the noise contributes randomly and therefore results in a net zero shift. Gated fluorescent source's peaks and the gated PXR spectral peaks will consistently shift to lower values than expected if the calibration is based on radioactive sources. Therefore, the known fluorescent energy values were used to calibrate the detectors.

### C. ENERGY CALIBRATION

For each experiment an energy calibration spectrum was obtained. These were obtained by measuring the x-ray fluorescence from either three separate foils or the sandwich foil described in Section A. Observed x-rays are the fluorescent x-rays at the K-edge of the excited atom. The K-edge x-ray energy for titanium is 4.509 keV, 8.04 keV for copper, 14.932 keV for yttrium, 24.10 keV for indium and 25.196 keV for tin .[Ref. 18] The calibration is obtained by establishing the centroid of the fluorescent peak. That centroid channel is then set equal to the known de-excitation energy. Assuming a linear relationship between channel position and energy, the equation for determining the energy for a given channel is determined by the following equations:

$$E = \alpha(\text{chn}) + \beta , \quad (28)$$

$$\alpha = \frac{E_1 - E_2}{\text{chn}_1 - \text{chn}_2} , \quad (29)$$

$$\beta = E_2 - \alpha(\text{chn}_2) , \quad (30)$$

where  $E_1$  and  $E_2$  are the energies of peak 1 and peak 2 respectively, and  $\text{chn}_1$  and  $\text{chn}_2$  are the corresponding centroid channel numbers,  $\alpha$  is the slope and  $\beta$  is the intercept of the Energy vs. Channel line.

#### IV. DATA AND ANALYSIS

##### A. SINGLE ANGLE EXPERIMENTS (FAR REGION, $\Delta\theta_x < \text{FWHM OF } J_2$ )

To obtain a PXR spectrum, the target ladder was lowered until the mirror was in line with the electron beam, and the home position was determined as described in Chapter III. section A. The ladder was lowered to the crystal and then rotated to the desired angle. All single angle experiments used the ORTEC SiLi detector and were in the far region. For the far region the detector was approximately 100 cm from the target and subtended  $2.0 \times 10^{-4}$  sr. A summary of the various variables for these experiments can be found in Table 1, and the details are given below.

TABLE 1. SUMMARY OF VARIABLES FOR THE SINGLE ANGLE EXPERIMENTS WITH NOMINAL ANGLES NEAR THE BRAGG ANGLE OF 22.5 DEGREES.

Date	Beam Energy (MeV)	Amplifier (peaking time)	Gate (width) [delay]	Detector (distance to detector)	Nominal Angle (degrees)
5 May	~90	Ortec 450 (12 $\mu$ s)	Ortec 426 (5 $\mu$ s) [30.6 $\mu$ s]	EG&G Ortec SiLi model #7113-16250 (1006 mm)	22.5
8 May	~90	TENNELEC TC 244 (12 $\mu$ s)	"	" (1003 mm)	22.5
7 July	88	"	"	" (1002 mm)	22.5
	88	"	"	" (1002 mm)	23
8 July	84.5	TENNELEC TC 244 (8 $\mu$ s)	Ortec 426 (35 $\mu$ s) [7.7 $\mu$ s]	" (1003 mm)	22.5

"Beam energy" is the energy of the LINAC electron beam, "Amplifier" is the model of the amplifier, with the amplifier peaking time listed below in parentheses, "Gate" is the model of the linear gate used with the gate width listed in parentheses and the delay time from



the LINAC start for the start of the gate are listed in brackets, "Detector" is the model number of the detector with the distance to the detector listed in parentheses (the variations are due to slight variations in the distance from the kapton window to the detector window referred to as the air gap), "Nominal Angle" is the crystal angle with respect to the electron beam line.

Data was obtained on May 5<sup>th</sup> by rotating the crystal 157.5 degrees clockwise ( $\theta_C = 157.5$  degrees) which corresponds to  $\theta_B = 22.5$  degrees. The window to detector distance (air gap) was 1.4 cm of air. The ORTEC 450 amplifier was used. The PXR spectrum is shown in Figure 9.

Data was obtained on May 8<sup>th</sup> at the same angle for a longer time to improve signal to noise. The ORTEC 450 amplifier was replaced by the TENNELEC TC 244 amplifier for this and all the subsequent single angle experiments. The amplifier was set for a 12  $\mu$ s peaking time, which gives the best energy resolution. The delay time of the linear gate was adjusted based upon observation of the copper foil fluorescence to 30.6  $\mu$ s. The air gap was 1.1 cm. The PXR and calibration spectra are shown in Figures 10 & 11. The calibration for May 5<sup>th</sup> is similar to that of May 8<sup>th</sup> and is not shown.

Data was also obtained on July 7<sup>th</sup> at a Bragg angle of 22.5 degrees. The LINAC was tuned to 88.0 MeV and the air gap thickness was 1.0 cm. The amplifier and gating setups were the same as those on May 8<sup>th</sup>. There appeared to be a drift problem, either a drift in klystron noise as the machine warmed up, or a detector drift. To reduce the effects of this drift the experiment was performed as follows. First a calibration was obtained using the sandwich foil starting at 0 hours, then using the carbon crystal, a PXR spectrum was obtained for two hours. Due to a setup error the crystal was positioned such that the electron beam missed the tin backing, and therefore there wasn't a tin peak for the calibration and later for an absolute photons per electron calculation. This spectrum was saved and a second calibration was obtained after three hours. This was followed by two separate two hour PXR spectra, which were obtained without moving the ladder. This

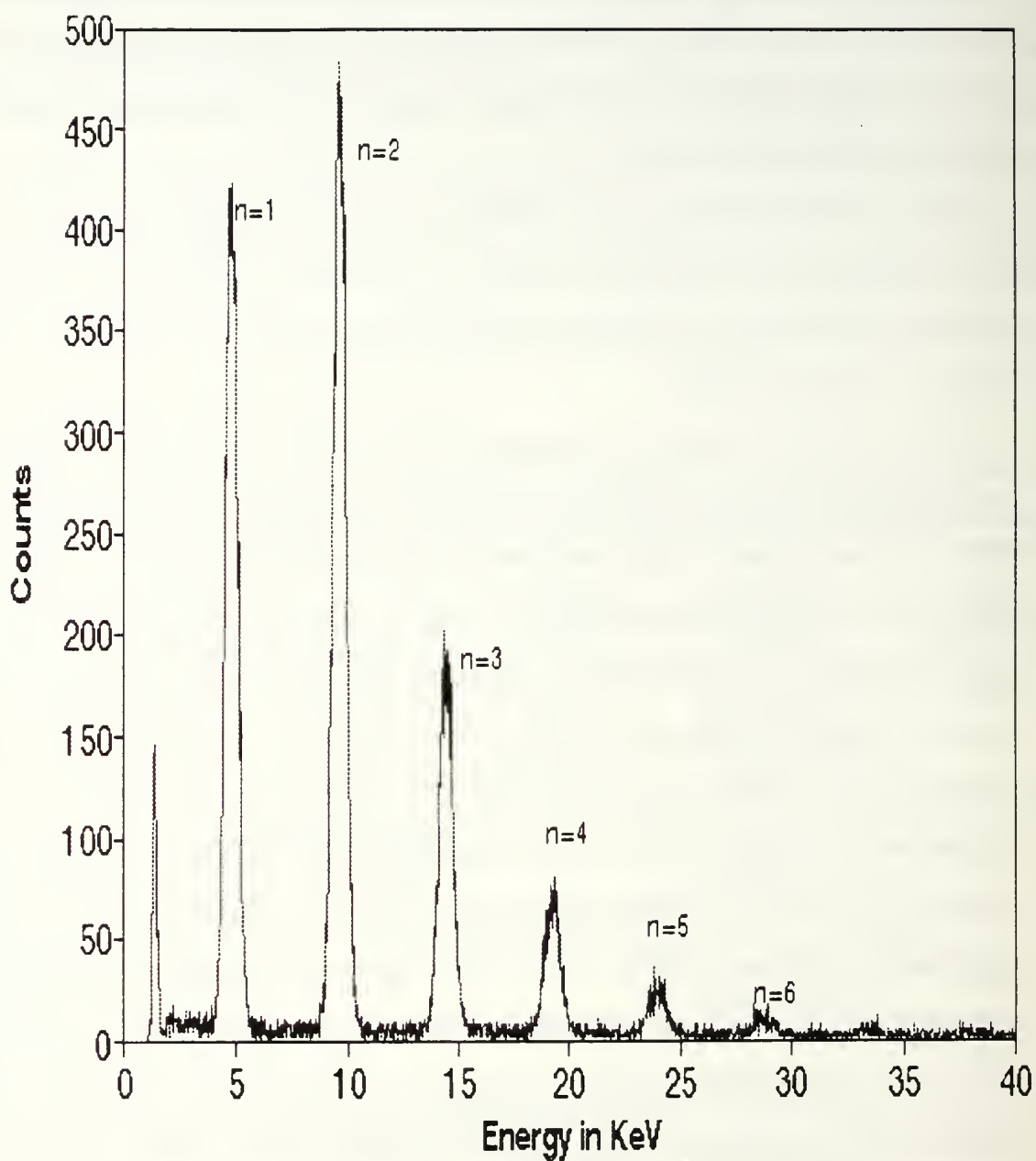


Figure 9. PXR spectrum from the {002} planes of the carbon graphite crystal, obtained on May 5 at an angle of 22.5 degrees. This spectrum clearly shows 6 orders. The low energy peak is LINAC induced noise.

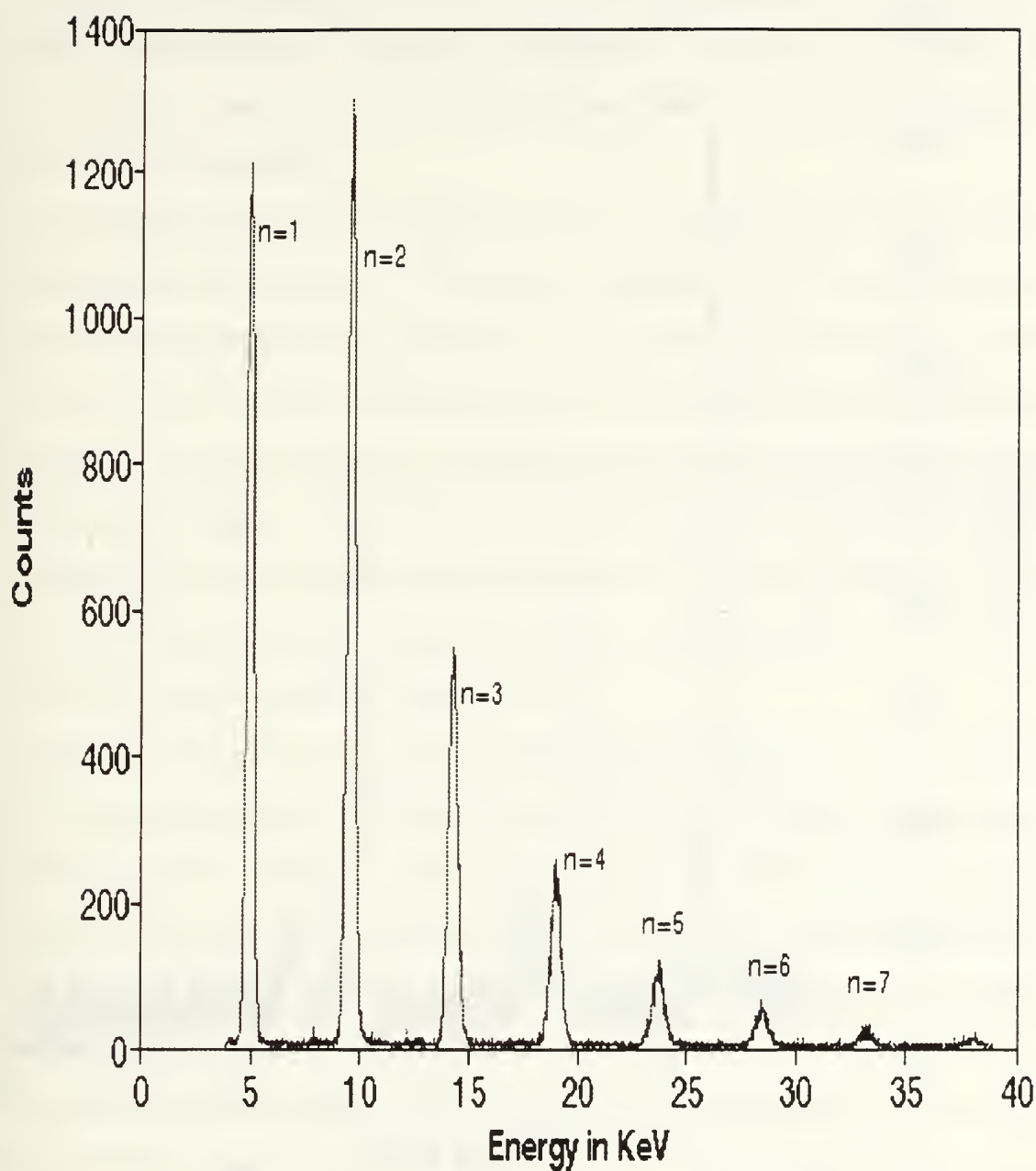


Figure 10. PXR spectrum from the {002} planes of the carbon graphite crystal, obtained on May 8 at an angle of 22.5 degrees. This spectrum clearly shows 7 orders. The pulse height analyzer discriminator was set at approximately 4 KeV to discriminate out the LINAC induced noise.

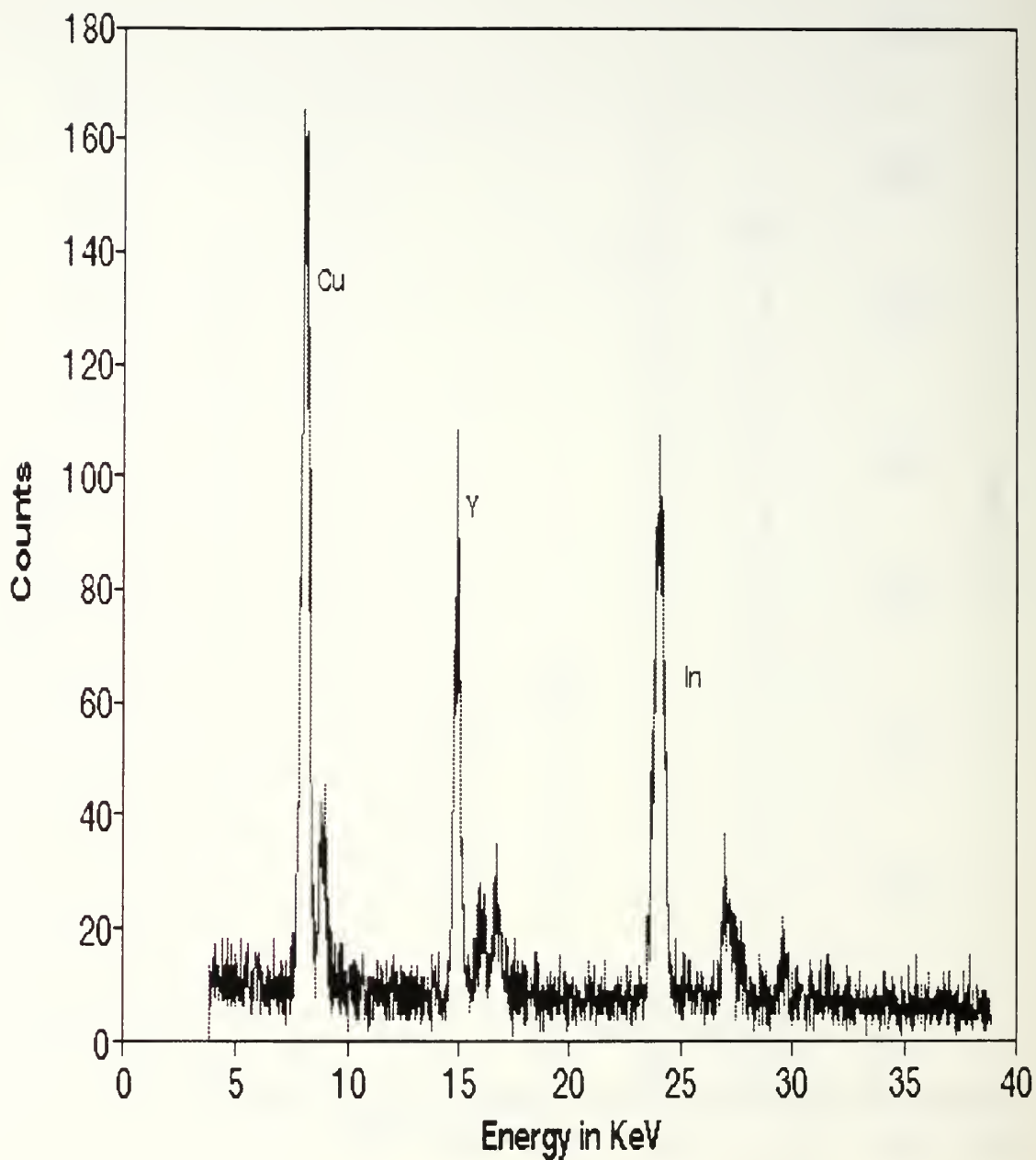


Figure 11. Energy calibration spectrum obtained on May 8. This calibration used the spectrum of three separate foils which were added together by use of a spreadsheet on QPRO. The pulse height analyzer discriminator was set at approximately 4 KeV to discriminate out the LINAC induced noise.



resulted in three independent PXR spectra at a nominal Bragg angle of 22.5 degrees. The crystal was then rotated to a nominal Bragg angle of 23 degrees and a spectrum was obtained for two hours, followed by a third calibration after 9 hours from the beginning of this day's data accumulation.

The calibration information is shown in Table 2. This table shows that the second calibration's centroids appear to shift about six channels to the left compared to their corresponding peaks in the first calibration, while the third calibration's centroids appear within one channel of the corresponding peaks in the first calibration. This information shows that it is crucial to have tin or another fluorescent foil in place for calibration while taking a PXR spectrum. It also suggests that data be taken in several shorter time periods rather than one longer time period. With knowledge of the tin peak's position for each run one can then shift the spectra appropriately and then add them together. This procedure will markedly improve the spectral resolution.

The spectra taken at 22.5 degrees were combined in the following manner. The centroid of the tin calibration peak in each spectra was determined. Then by shifting the channels of the three spectra so that the tin centroids were the same, the three spectra were added channel by channel on a QPRO spreadsheet [Ref. 22]. Figures 12-14 show the combined PXR spectrum at 22.5 degrees, the spectrum at 23 degrees and the energy calibration spectrum respectively.

On July 8<sup>th</sup> similar data was obtained, using the new linear gate set at 35  $\mu\text{s}$  wide and delayed from the machine start cycle time,  $T_0$  by 7.7  $\mu\text{s}$ . The air gap thickness was 1.1 cm. Additionally the amplifier peaking time was reduced from 12  $\mu\text{s}$  to 8  $\mu\text{s}$ . A lower peaking time reduces the effect of double counting single events since the effects of double counting are proportional to the pulse peaking time, however there is a tradeoff with energy resolution. The energy resolution is related to the pulse peaking time. There are two contributions. One is from parallel noise (detector leakage current, and all resistors which parallel the detector) that is proportion to the square root of the peaking time. The

TABLE 2. JULY 7<sup>th</sup> CALIBRATION DATA, SHOWING PEAK ENERGY, CENTROID CHANNEL NUMBER AND PEAK FWHM.

<b>Cal. 0 hours</b>		<b>Theoretical Centroid Energy (keV)</b>	<b>Centroid channel # (shift)</b>	<b>Full Width Half Max. (keV)</b>	<b>Apparent Shift in Energy (eV)</b>
Titanium	K $\alpha$	4.509	191	0.640	-
Yttrium	K $\alpha$	14.932	747	0.620	-
	K $\beta$	16.7	847	0.675	-
Tin	K $\alpha$	25.196	1307	0.735	-
	K $\beta$	28.486	1487	1.470	-
<b>Cal 3 hours</b>					
Titanium	K $\alpha$	4.509	180 (-11)	0.320	-150
Yttrium	K $\alpha$	14.932	739 (-7)	0.415	-230
	K $\beta$	16.7	840 (-7)	0.490	-140
Tin	K $\alpha$	25.196	1302 (-5)	0.490	-90
	K $\beta$	28.486	1488 (-1)	1.22	-50
<b>Cal 9 hours</b>					
Titanium	K $\alpha$	4.509	192 (-1)	0.350	-70
yttrium	K $\alpha$	14.932	748 (-1)	0.305	-70
	K $\beta$	16.7	847 (-0)	0.370	0
Tin	K $\alpha$	25.196	1307 (-0)	0.345	0
	K $\beta$	28.486	1488 (+1)	0.290	+60

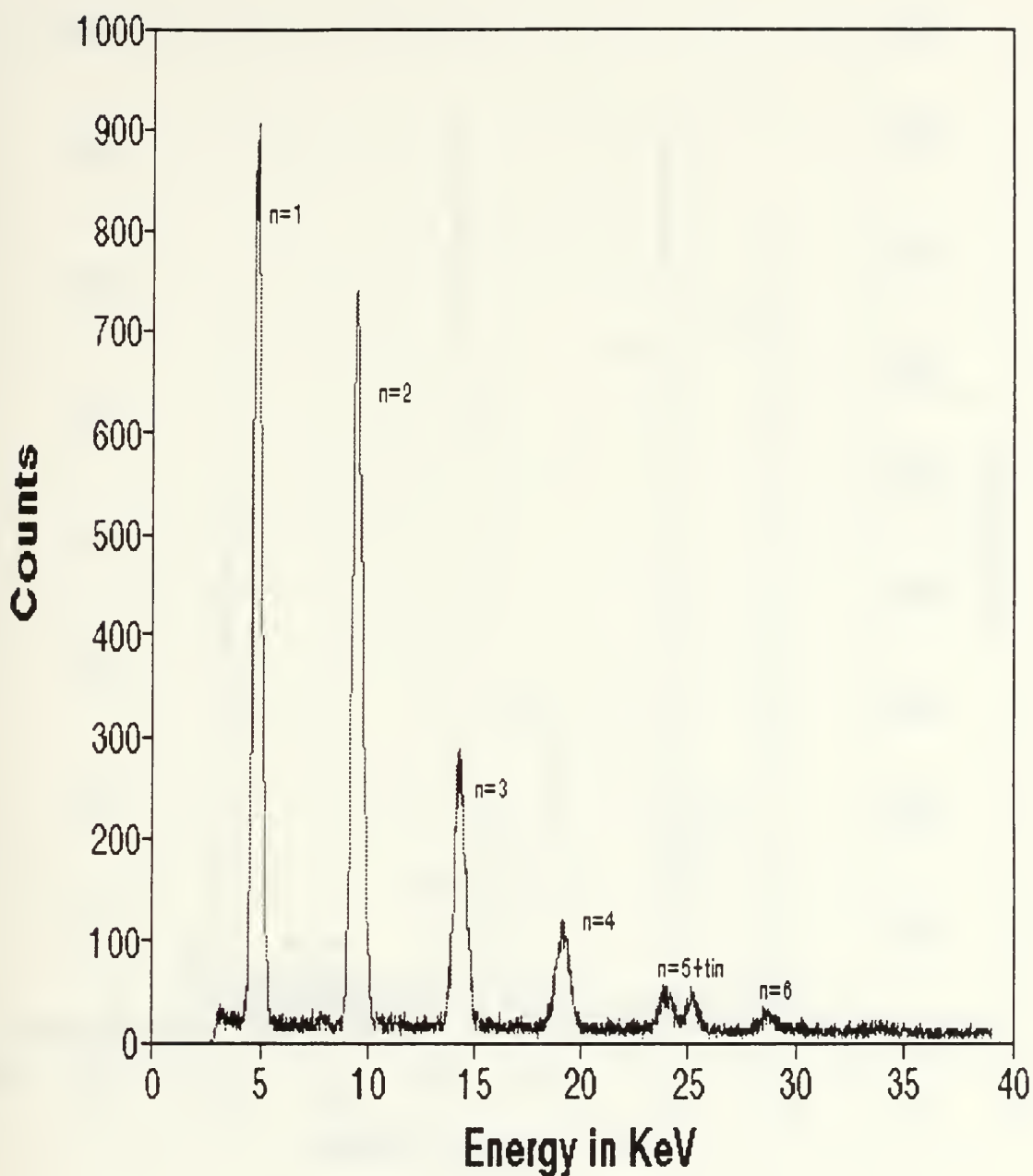


Figure 12. PXR spectrum from the {002} planes of carbon graphite, obtained on July 7<sup>th</sup> at an angle of 22.5 degrees. This spectrum was obtained by combining three separate shorter time period PXR spectrum. This spectrum shows six orders with the fifth order and the tin calibration peak slightly overlapping, with the tin peak at a higher energy than the n=5 peak.

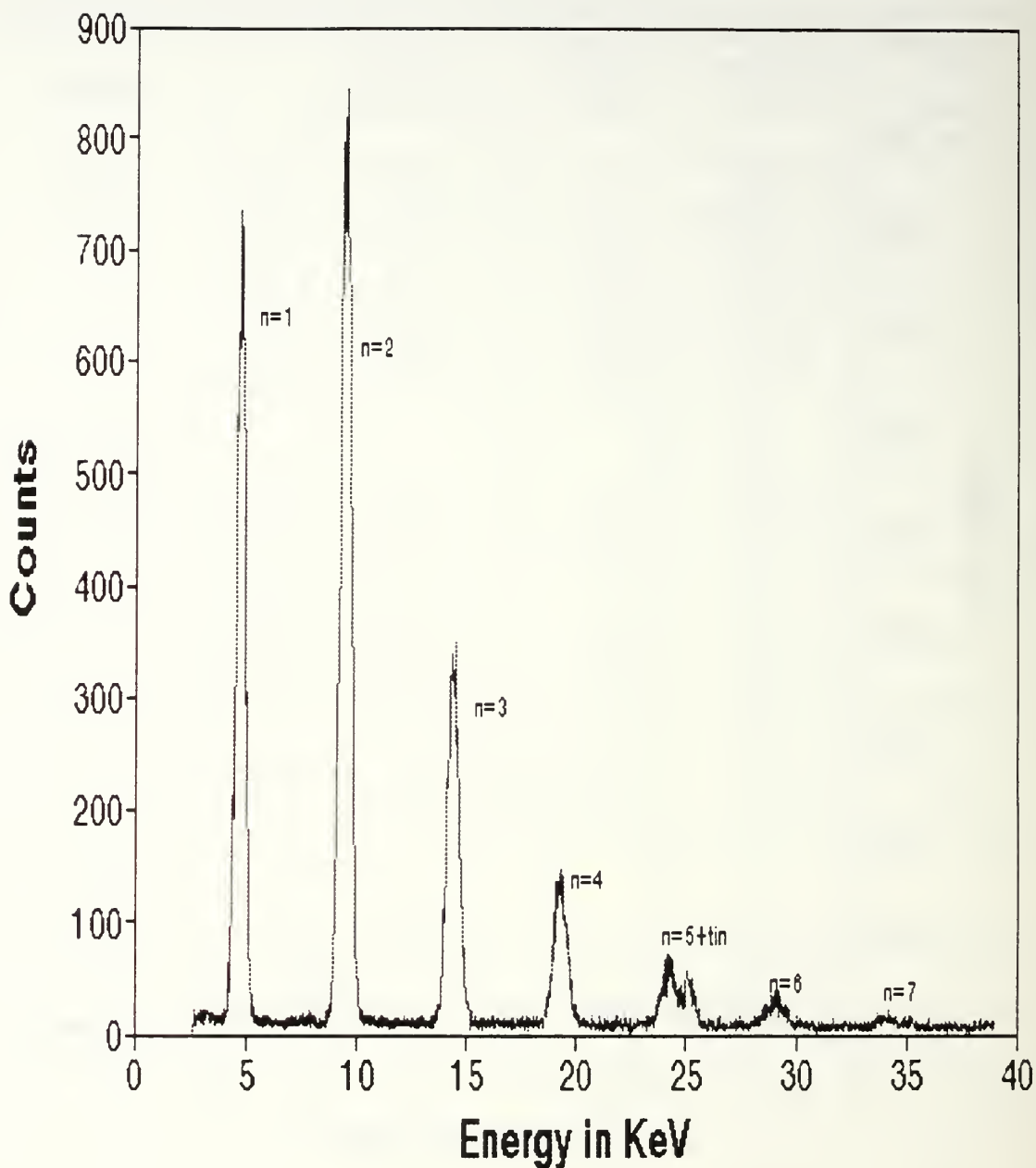


Figure 13. PXR spectrum from the {002} planes of carbon graphite, obtained on July 7<sup>th</sup> at an angle of 23. degrees. This spectrum shows six orders with the fifth order and the tin calibration peak slightly overlapping, with the tin peak at a higher energy than the n=5 peak.



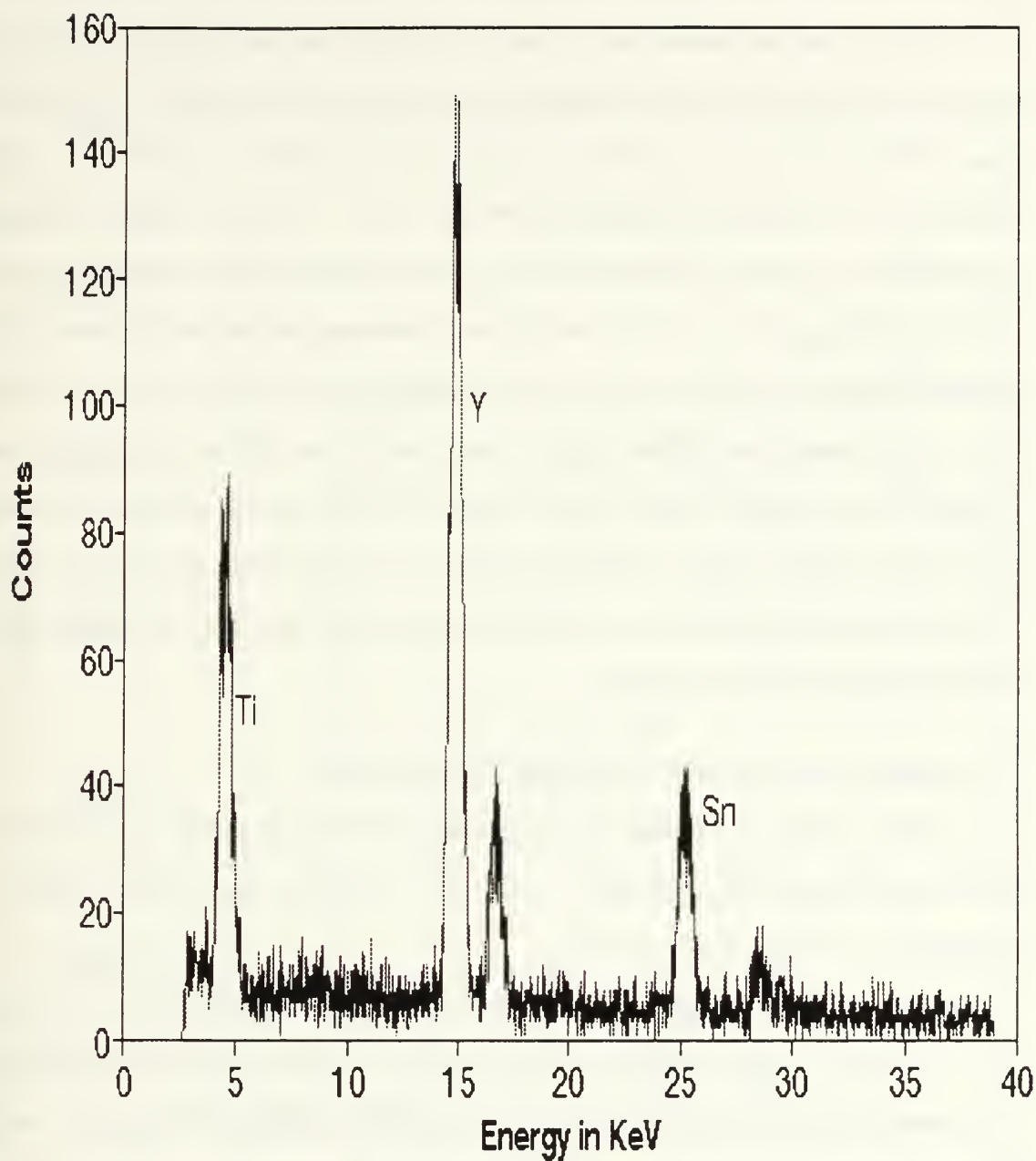


Figure 14. First of three energy calibrations obtained on July 7<sup>th</sup>. This calibration used the sandwich foil containing Titanium, Yttrium and Tin. The  $K_{\alpha}$  and  $K_{\beta}$  peaks of Y and Sn are both visible, while the Ti only shows the  $K_{\alpha}$  peak.

second is serial noise (total input capacitance, transconductance (gain of the input device etc.)) that is inversely proportional to the square root of the peaking time. This results in an optimum peaking time for SiLi detectors between 8 and 24  $\mu$ s. [Ref. 20] The LINAC was tuned to 84.5 MeV. Additionally, the PHA was updated to the PHA-II software which has 8192 channels compared to 2048 for PHA-I. The PHA-II digital stabilization was utilized to counter the effects of drift. An energy calibration was obtained before and after the PXR spectrum. To compare the results obtained with the results from the 2048 channel analyzer the data was binned using a simple program written in C (see Appendix B). Four channels were added together and placed in one bin using the energy value obtained from the third of the four bins. Figures 15 & 16 show the binned PXR spectrum and the first binned energy calibration spectrum. The resolution is probably improved because of collecting data over more channels and then binning, and due to the use of the PHA-II digital stabilization option.

## **B. SINGLE ANGLE PXR ANALYSIS (FAR REGION)**

In order to compare the data with theory, and from one experiment to the next the following analysis was performed. First the net area of each spectral peak was determined. This was done two ways.

The first way used the software supplied with the PCA I TENNELEC PHA. Using the PHA computer analysis the peaks were determined by estimating where each peak began and ended, and setting these channels as a region of interest. The PHA analyzer determines the average background by averaging the start channel with the three previous channels and the stop channel with the three following channels and drawing a straight line connecting these two average values. All counts below this noise line are treated as noise and counts above it as signal. The program determines the gross and net area. Gross area is the total number of counts in the region (including noise) and net area is only the

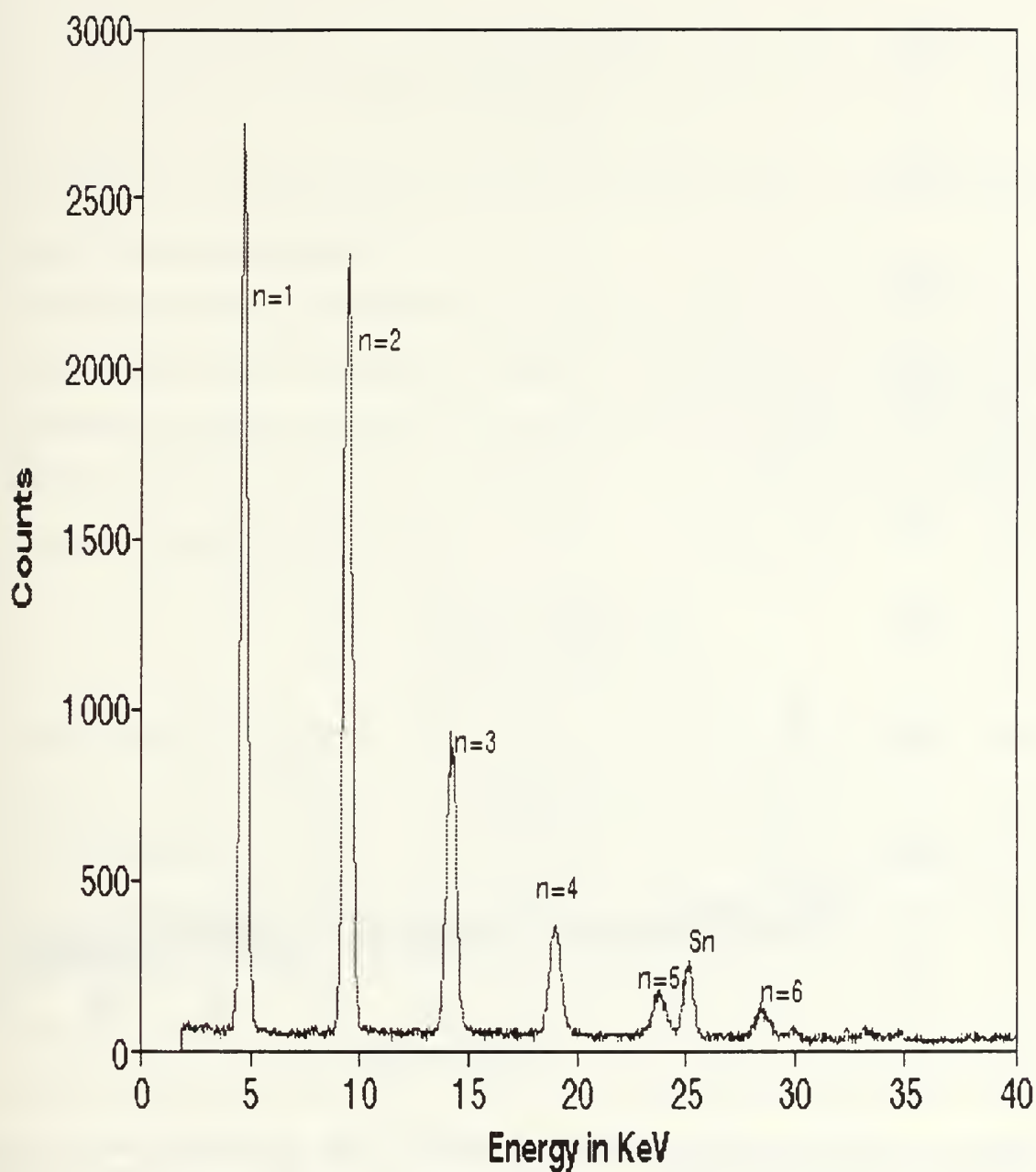


Figure 15. PXR spectrum from the {002} planes of carbon graphite, obtained on July 8<sup>th</sup> at an angle of 22.5 degrees, using the Canberra (SiLi) detector. This spectrum shows six orders with the fifth order and the tin calibration peak slightly overlapping, with the tin peak at a higher energy than the n=5 peak.

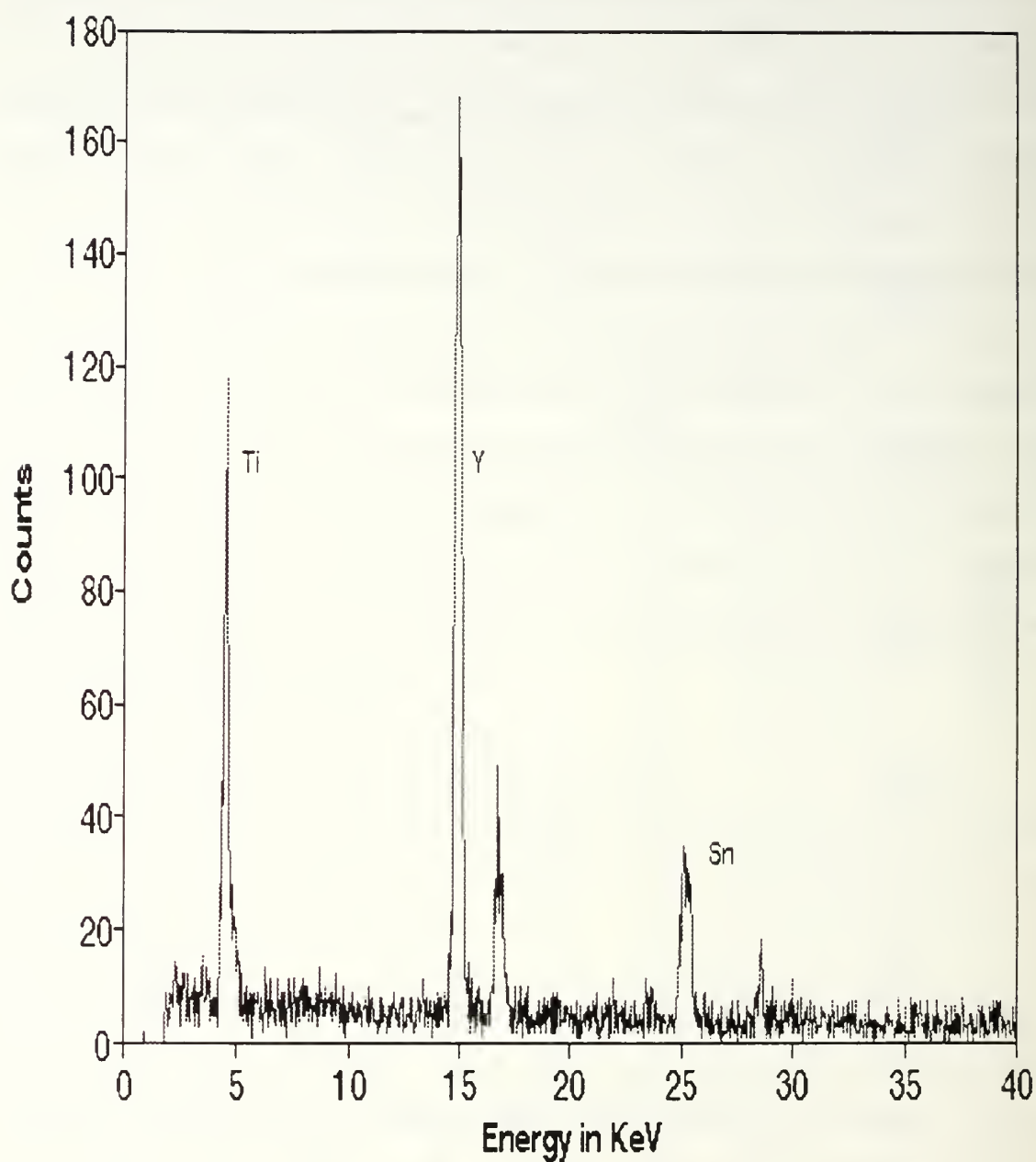


Figure 16. Energy calibration obtained on July 8<sup>th</sup>. This calibration used the sandwich foil and the Canberra (SiLi) detector. This spectrum shows the K $\alpha$  peak of Ti, Y and Sn, and the K $\beta$  peaks of Y and Sn. This spectrum was plotted by binning four channels together and plotted at the central channel of these four bins.



number of counts above the noise line. It also determines the FWHM and the centroid of the peak using the following equation:

$$\text{chn}_{\text{ctrd}} = \frac{\sum_i \text{counts}_i * \text{chn}_i}{\sum_i \text{counts}_i}, \quad (31)$$

where  $\text{Chn}_i$  is the channel number (or equivalent energy) and  $\text{counts}_i$  is the corresponding number of counts in that channel.

The second way was to determine the average noise in the regions between the peaks using the gross area of 100 channels divided by 100. The background was determined by multiplying the number of channels in the peak by the average noise in the region just following the peak. The net area is determined by subtracting this background from the Gross area. The error in the Net area is

$$\frac{\Delta N}{N} \% = \frac{\sqrt{\text{Area}_{\text{gross}} + \text{Area}_{\text{background}}}}{\text{Area}_{\text{gross}} - \text{Area}_{\text{background}}}, \quad (32)$$

since the error in the area is  $\sqrt{\text{Area}}$ . Tables 3-7 show these values for the various experiments. Figure 17 shows a plot of the comparison between the PHA net area and the Extended Background net area for the May 8th data. This plot shows that except for the first two peaks there is very little difference between the net areas as determined by these two methods.

The raw spectrum area needs to be corrected for attenuation as the photon travels between the target and the detector. Also the relative efficiency of the detector must be taken into account. The attenuation coefficients were determined using a computer program called XCOM [Ref 21] near the centroid energy. Some of the coefficients are listed in Table 8, along with the detector efficiency [Ref. 5] and the values of the correction factors for Be, Kapton and for air at the two extreme thickness values. The final column shows the total correction factor for an air thickness of 1.1 cm.

TABLE 3: MOSAIC CARBON CRYSTAL{002} PLANE PEAK DATA TAKEN MAY 5<sup>th</sup> FOR 90 MEV ELECTRON BEAM AT BRAGG ANGLE OF  $\theta_B = 22.5$  DEGREES FOR PEAKS 1-6.

peak #	<u>1</u>	<u>2</u>	<u>3</u>	<u>4</u>	<u>5</u>	<u>6</u>
E(n) keV	4.47	9.75	14.85	20.04	25.1	30.3
E(n)/E(1)	1	2.18	3.32	4.48	5.62	6.77
<b><u>Peak</u></b>						
gross	423	482	202	76	36	15
background	5	5	5	5	5	5
net	418	477	197	71	31	10
<b><u>Area</u></b>						
gross	13822	16570	7261	3286	1284	630
<b>PHA</b>						
background	858	588	736	642	462	320
net	12964	15982	6525	2644	822	310
$\Delta N/N\%$	0.93	0.82	1.37	1.75	5.1	10
<b>Extended Background</b>						
background	400	485	455	500	380	400
net	13422	16525	6806	2786	904	240
$\Delta N/N\%$	0.89	0.81	1.29	2.21	4.1	13

TABLE 4: MOSAIC CARBON CRYSTAL{002} PLANE PEAK DATA TAKEN MAY 8<sup>th</sup> FOR 90 MEV ELECTRON BEAM AT BRAGG ANGLE OF  $\theta_B = 22.5$  DEGREES FOR PEAKS 1-4

peak #	<u>1</u>	<u>2</u>	<u>3</u>	<u>4</u>
E(n) keV	4.905	9.509	14.239	19.0301
E(n)/E(1)	1	1.94	2.9	3.88
<b><u>Peak</u></b>				
gross	1213	1301	552	260
background	8	8	8	8
net	1205	1293	544	252
<b><u>Area</u></b>				
gross	25888	31844	16189	8192
<b><u>PHA</u></b>				
background	918	869	750	850
net	24970	30975	15439	7342
$\Delta N/N\%$	0.66	0.56	0.84	1.3
<b><u>Extended Background</u></b>				
background	424	624	592	672
net	25464	31220	15597	7520
$\Delta N/N\%$	0.64	0.58	0.83	1.25

TABLE 5. SAME AS TABLE 4 FOR PEAKS 5-8.

peak #	<u>5</u>	<u>6</u>	<u>7</u>	<u>8</u>
E(n) KeV	23.828	28.5723	33.3524	38.368
E(n)/E(1)	4.86	5.83	6.8	7.82
<b><u>Peak</u></b>				
gross	121	69	33	20
background	7	6	5	4
net	114	63	28	16
<b><u>Area</u></b>				
gross	4473	2287	1248	733
<b>PHA</b>				
background	624	574	352	252
net	3849	1713	896	481
$\Delta N/N\%$	1.85	3.12	4.46	6.52
<b>Extended Background</b>				
background	721	486	435	332
net	3752	1801	813	401
$\Delta N/N\%$	1.92	2.92	5.05	8.14



TABLE 6: MOSAIC CARBON CRYSTAL{002} PLANE COMBINED PEAK DATA TAKEN JULY 7<sup>th</sup> FOR 88 MEV ELECTRON BEAM AT BRAGG ANGLE OF  $\theta_B = 22.5$  DEGREES FOR PEAKS 1-5. ANALYZED BY COMBINING THE THREE INDIVIDUAL 22.5 DEGREE SPECTRUM.

peak #	<u>1</u>	<u>2</u>	<u>3</u>	<u>4</u>	<u>5</u>
E(n) KeV	4.85	9.50	14.30	19.10	23.99
E(n)/E(1)	1	1.96	2.95	3.94	4.95
<b><u>Peak</u></b>					
gross	4905	740	287	123	55
background	17	17	15	13	11
net	888	723	272	110	44
<b><u>Area</u></b>					
gross	23812	23590	10640	5304	2454
<b><u>PHA</u></b>					
background	1315	1269	1517	1434	1213
net	22497	22321	9123	3870	1241
$\Delta N/N\%$	0.70	0.71	1.21	2.21	4.88
<b><u>Extended Background</u></b>					
background	1283	1518	1345	1388	1016
net	22529	22072	9295	3916	1438
$\Delta N/N\%$	0.70	0.72	1.18	2.09	4.10

TABLE 7. MOSAIC CARBON CRYSTAL{002} PLANE PEAK DATA TAKEN JULY 7<sup>th</sup> FOR 88 MEV ELECTRON BEAM AT BRAGG ANGLE OF  $\theta_B = 23.0$  DEGREES FOR PEAKS 1-5.

peak #	<u>1</u>	<u>2</u>	<u>3</u>	<u>4</u>	<u>5</u>
E(n) KeV	4.72	9.47	14.39	19.32	24.20
E(n)/E(1)	1	2.01	3.05	4.09	5.13
<b><u>Peak</u></b>					
gross	735	843	349	149	70
background	11	10	10	8	7
net	724	833	339	141	63
<b><u>Area</u></b>					
gross	19766	25832	12319	5766	-
<b><u>PHA</u></b>					
background	1020	960	1248	855	-
net	18746	24872	11071	4911	2217 <sup>1</sup>
$\Delta N/N\%$	0.77	0.66	1.05	1.66	-
<b><u>Extended Background</u></b>					
background	921	949	986	795	-
net	18845	24883	11333	4971	-
$\Delta N/N\%$	0.76	0.66	1.02	1.35	-

<sup>1</sup>The net area was determined by use of a peak fitting program with the following parameters: Gaussian Peak; 25.197 KeV centroid, 0.548 FWHM with a background of counts =  $20.94 - 0.527 \cdot \text{Energy}$ , which is consistent with the value of 7 used in the Peak channel.

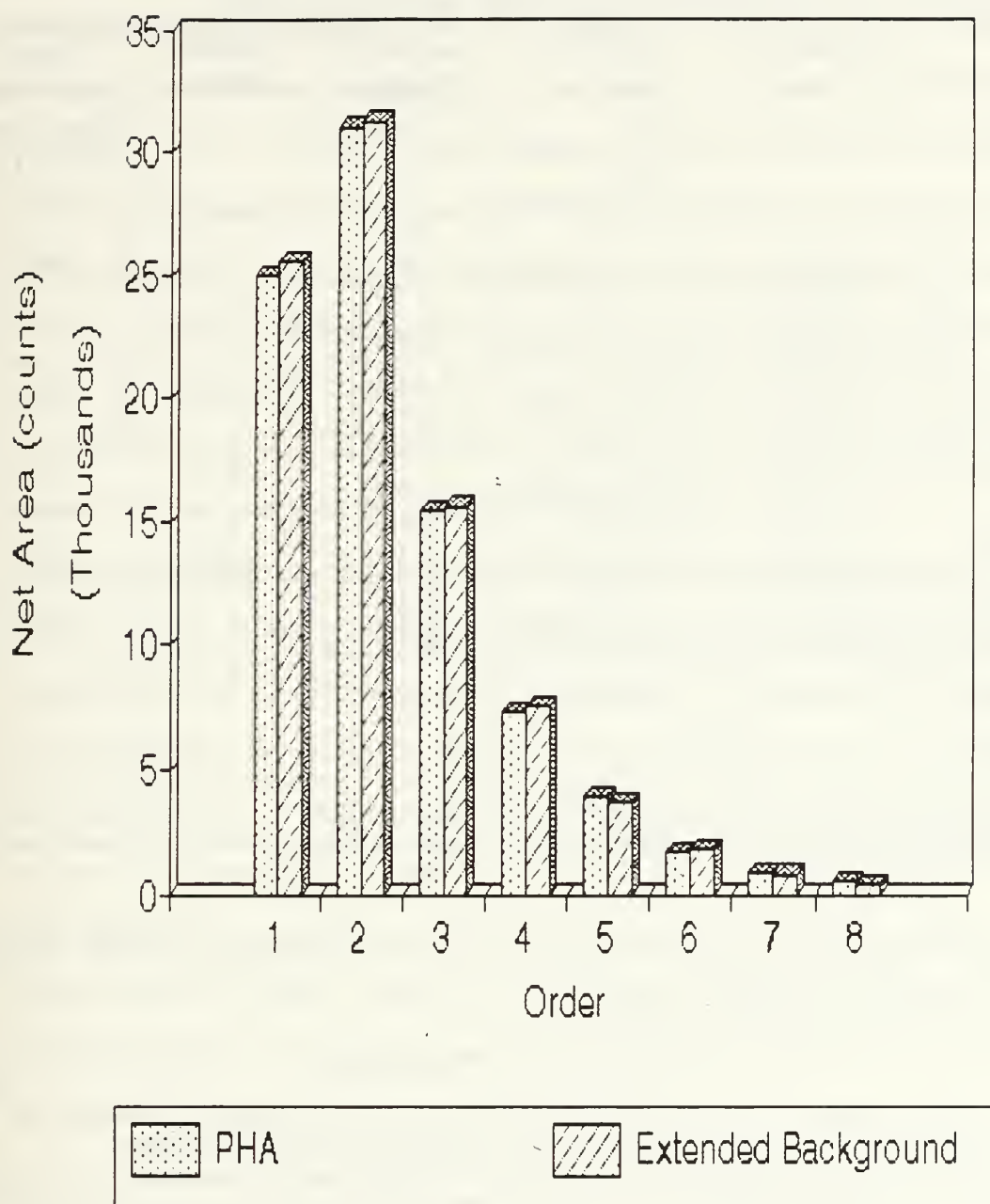


Figure 17. Plot of the net area in each peak as a function of the peak number as determined by the pulse height analyzer and by using the extended background method for the May 8th data.

TABLE 8. ATTENUATION COEFFICIENTS FOR THE PEAK ENERGIES, DENSITY AND THICKNESS FOR BE, DRY AIR AND KAPTON.

Energy (KeV)	$\mu$ (cm <sup>2</sup> /g) Be [ $e^{-\mu\rho t}$ ]	$\mu$ (cm <sup>2</sup> /g) Dry Air [ $e^{-\mu\rho t}$ $t=1.0$ cm] { $e^{-\mu\rho t}$ $t=1.4$ cm}	$\mu$ (cm <sup>2</sup> /g) Kapton [ $e^{-\mu\rho t}$ ]	Detector Efficiency	Total correction factor for t air =1.1 cm
5	4.37 [0.961]	40.3 [0.949] {0.930}	25.5 [0.913]	1.0	0.833
10	0.647 [0.994]	5.12 [0.993] {0.991}	3.18 [0.989]	1.0	0.976
15	0.307 [0.997]	1.61 [0.998] {0.997}	1.04 [0.996]	1.0	0.991
20	0.225 [0.998]	0.778 [0.999] {0.999}	0.542 [0.998]	0.97	0.965
25	0.194 [0.998]	0.484 [0.999] {0.999}	0.366 [0.999]	0.86	0.857
30	0.179 [0.998]	0.354 [1.00] {0.999}	0.288 [0.999]	0.72	0.717
density g/cm <sup>3</sup>	1.82	0.001294	1.42	-	-
thickness	0.005 cm	1.0<t<1.4 cm	0.0025 cm	-	-

Using the net area from the PHA analysis and the coefficients listed above the corrected counts is determined using the following:

$$I_0 = I * e^{+(\mu\rho t)_{Be} + (\mu\rho t)_{Air} + (\mu\rho t)_{Kapton}}, \quad (33)$$

where I is either Net Area or Net Peak counts counted by the (SiLi) detector.

Two methods of analysis were used to determine the counts at the front face of the crystal  $I_0$ . The first and simplest used equation 33 applied peak to peak where  $(\mu\rho t)_{total}$  is assumed constant over the entire peak. This is the analysis used in references 4 & 5. However, for the low energy peaks  $\mu$  varies over the peak and the values obtained for  $I_0$  vary depending on if you use  $\mu(5 \text{ keV})$  or  $\mu$  for each individual channel. For this reason a second method was examined. The second method involved using a least squares fit of

the attenuation coefficient. The actual coefficients and the approximations for the three materials are shown in Figures 18-20. The formulas give  $\mu$  as a function of energy and are applied to the values of energy and the number of counts on a QuattroPro (QPRO) spreadsheet. [Ref. 22] The counts are then summed over the peak and a new  $I_0$  is obtained. See Table 9 for the areas and the ratio of the area of the nth order to the area of the first order for the raw data as collected by the detector, the corrected data using the linear attenuation coefficient at the centroid and the data corrected using the linear attenuation coefficient for each channel. Figure 21 plots the raw area, the area corrected for attenuation based on the coefficient at the peak centroid and the coefficient for each channel using the least square fit values for the May 8th data.

It is not clear that the use of the channel by channel correction is appropriate since the detector response not only broadens the PXR spectrum, there is a folding of the detector response into the PXR spectral response. If the detector resolution is small compared to the PXR resolution the channel by channel correction method is a better approximation, if the PXR resolution is small compared to the detector resolution the correction at the centroid is the better approximation, and if the two are comparable which is the case for these experiments as seen below the best method would be to deconvolve the PXR spectrum from the detector response and then apply a channel by channel correction. Since this method is extremely complex it is not applied here, and for ease of calculation **the method of using the attenuation coefficient at the peak centroid will be utilized for the remainder of the analysis.** In order to determine the best method the PXR resolution needs to be calculated.

### **1. Detector Resolution at PXR Spectral Energies.**

To determine the detector energy resolution, the calibration peaks were assumed to be Gaussian in shape. The natural line widths of the x-ray fluorescence peaks were



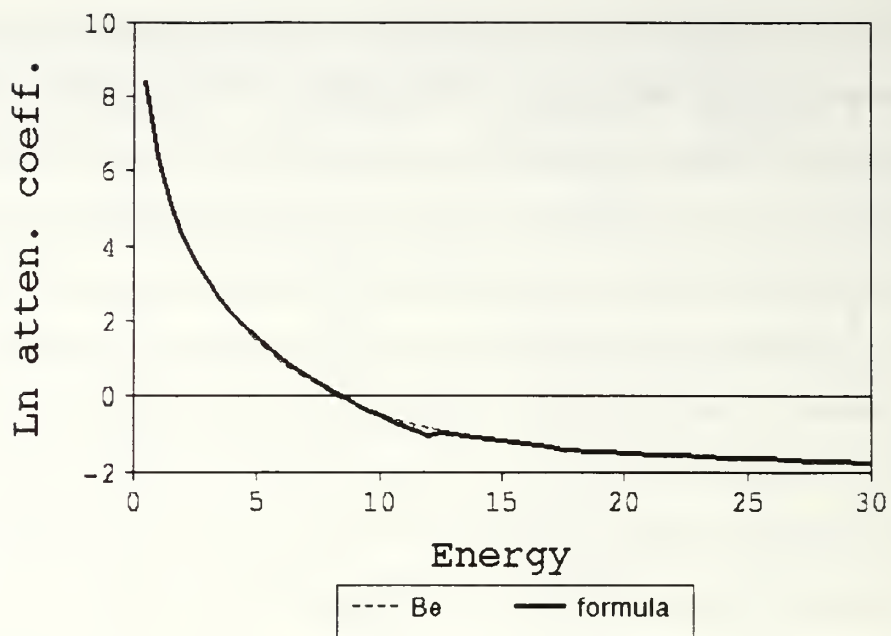


Figure 18. Plot of the log of the actual linear attenuation coefficient for Be vs. energy in KeV, and the formula values using 3 section least square fit.

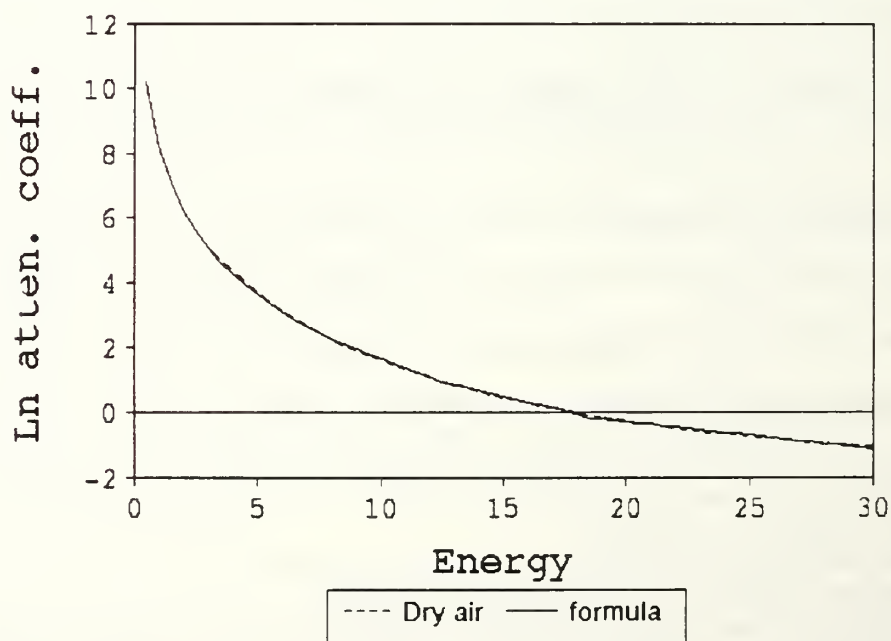


Figure 19. Plot of the log of the actual linear attenuation coefficient for Dry Air vs. energy in KeV, and the formula values using 3 section least square fit.

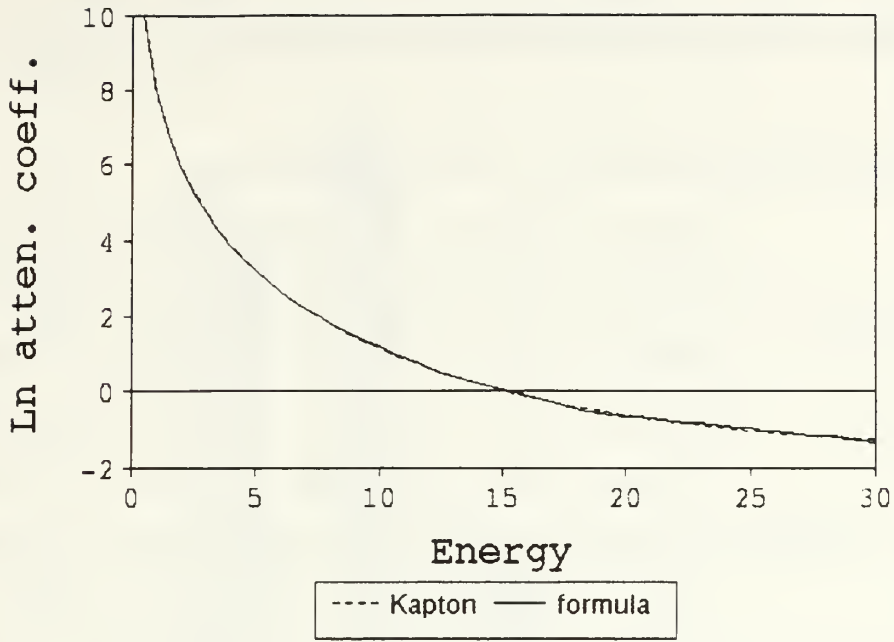


Figure 20. Plot of the log of the actual linear attenuation coefficient for Kapton vs. energy in KeV, and the formula values using 3 section least square fit.

obtained from Reference 23, these natural line widths varied from 10 eV to 45 eV. The natural line widths were also assumed to be Gaussian distributions. From the measured fluorescence peaks the detector resolution or linewidths were determined by adding them in quadrature:

$$\Gamma_{obs}^2 = \Gamma_{det}^2 + \Gamma_{lw}^2, \quad (34)$$

where  $\Gamma_{obs}$  is the measured linewidth,  $\Gamma_{det}$  is the detector resolution and  $\Gamma_{lw}$  is the natural fluorescent linewidth. The units are keV. The uncertainty in  $\Gamma_{lw}$  is assumed to be zero, therefore the uncertainty in  $\Gamma_{det}$  is the same as the uncertainty in  $\Gamma_{obs}$ . The experimental values of  $\Gamma_{det}$  and  $\Gamma_{obs}$  by less than two tenths of a percent. These results are in agreement with those previously obtained [Ref. 4.] Thus the value of the detector resolution to be used will be that of the observed calibration spectrum line widths.

TABLE 9. DATA CORRECTED FOR ATTENUATION THROUGH KAPTON WINDOW, AIR AND BE DETECTOR WINDOW.

Date	1	2	3	4	5
<b>Measured Area at the detector; ratio Area<sub>n</sub>/Area<sub>1</sub></b>					
5 May	12964 ; 1	15982 ; 1.23	6525 ; 0.50	2644 ; 0.20	822 ; 0.06
8 May	24970 ; 1	30975 ; 1.24	15439 ; 0.62	7342 ; 0.29	3849 ; 0.15
7 July 22.5°	22497 ; 1	22321 ; 0.99	9123 ; 0.41	3870 ; 0.17	1241 ; 0.06
7 July 23°	18746 ; 1	24872 ; 1.33	11071 ; 0.59	4911 ; 0.26	2216 ; 0.12
8 July	28690 ; 1	28554 ; 1.00	13666 ; 0.48	5649 ; 0.20	1354 ; 0.05
<b>Area Corrected for attenuation at the peak centroid; ratio Area<sub>n</sub>/Area<sub>1</sub></b>					
5 May	15886 ; 1	16410 ; 1.03	6587 ; 0.41	2648 ; 0.17	825 ; 0.05
8 May	30124 ; 1	31742 ; 1.05	15575 ; 0.52	7379 ; 0.24	3863 ; 0.13
7 July 22.5°	27000 ; 1	22859 ; 0.85	9202 ; 0.34	3889 ; 0.14	1246 ; 0.05
7 July 23°	22498 ; 1	25471 ; 1.13	11166 ; 0.50	4936 ; 0.22	2224 ; 0.10
8 July	34624 ; 1	29262 ; 0.85	13786 ; 0.40	5678 ; 0.16	1359 ; 0.04
<b>Area corrected at each channel using fitted coefficients; ratio Area<sub>n</sub>/Area<sub>1</sub></b>					
5 May	13418 ; 1	16294 ; 1.21	6868 ; 0.51	2848 ; 0.21	1029 ; 0.08
8 May	27333 ; 1	31559 ; 1.15	15642 ; 0.57	7533 ; 0.28	3896 ; 0.14
7 July 22.5°	24816 ; 1	22484 ; 0.90	9498 ; 0.38	4026 ; 0.16	-
7 July 23°	20843 ; 1	25166 ; 1.21	11357 ; 0.55	4981 ; 0.24	-
8 July	31405 ; 1	29337 ; 0.95	13491 ; 0.43	5674 ; 0.18	2476 ; 0.08

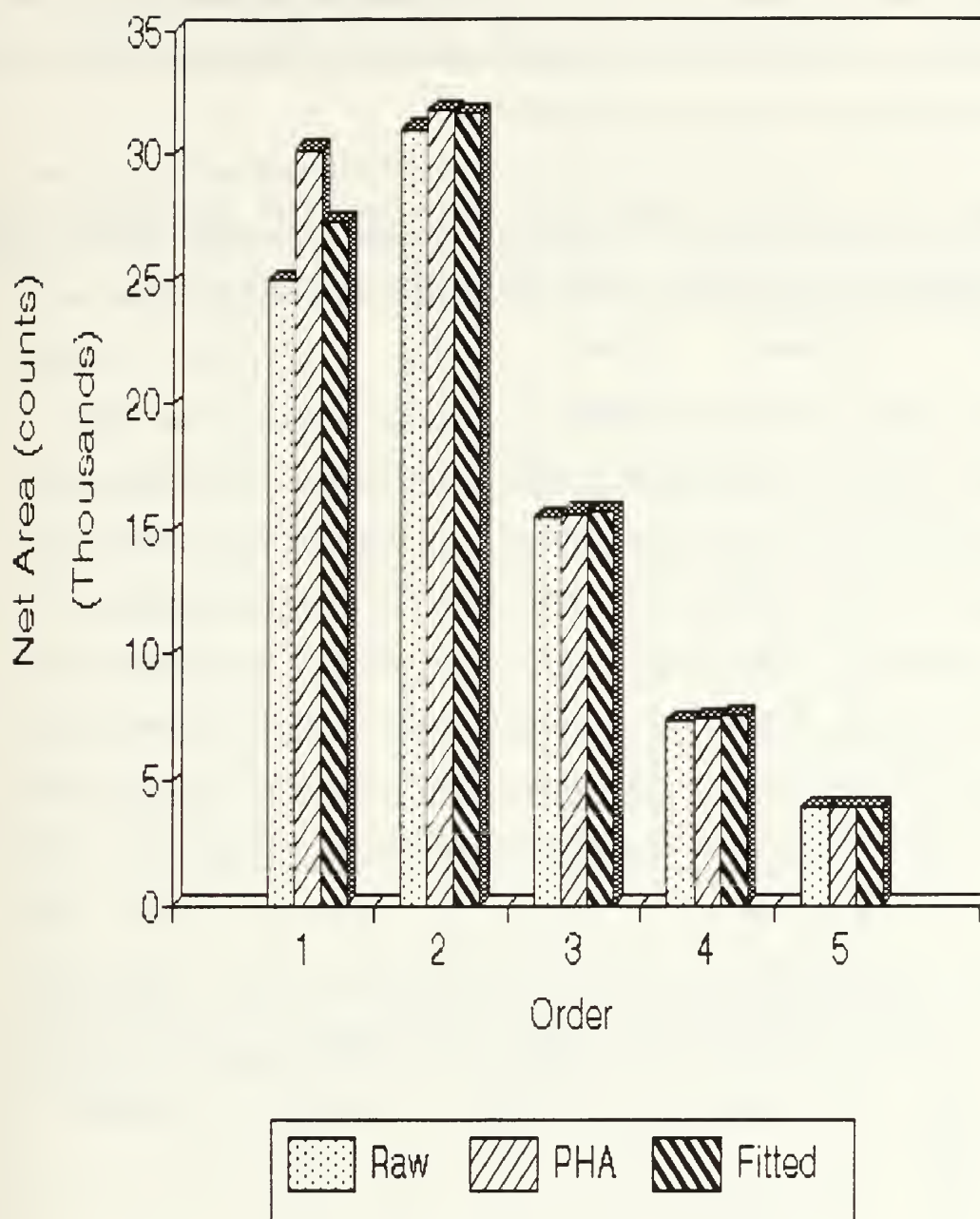


Figure 21. Plot of the raw area at the detector, the corrected area using the linear attenuation coefficient at the centroid of the peak (labeled centroid) and the linear attenuation coefficient for each channel based on a least square fit for the May 8th data.

Table 10 lists the values of the natural x-ray fluorescence linewidths and the observed linewidths as determined by the pulse height analyzer for the calibration foils for the May 5<sup>th</sup>, May 8<sup>th</sup>, July 7<sup>th</sup> and July 8<sup>th</sup> spectra.

TABLE 10. LIST OF CALIBRATION FOILS AND THE RESPECTIVE X-RAY ENERGY PEAK VALUES. INCLUDED IN THE LIST ARE THE NATURAL LINewidths OF THE FOILS, AND THE OBSERVED RESOLUTION.

Date	Element	Energy (keV)	$\Gamma_{lw}$	$\Gamma_{obs}$
May 5	Cu	8.04	0.003	0.698
	Y	14.92	0.006 <sup>2</sup>	0.628
May 8	Cu	8.04	0.003	0.394
	Y	14.92	0.006 <sup>2</sup>	0.269
	In	24.10	0.010 <sup>3</sup>	0.466
July 7	Ti	4.51	0.002	0.325 <sup>4</sup>
	Y	14.92	0.006 <sup>2</sup>	0.417 <sup>4</sup>
	Sn	25.196	0.010 <sup>5</sup>	0.493 <sup>4</sup>
July 8	Ti	4.51	0.002	0.180
	Y	14.92	0.006 <sup>1</sup>	0.300
	Sn	25.196	0.010 <sup>5</sup>	0.248

<sup>2</sup>The linewidth of Y wasn't listed in reference 23. The values was approximated by using the values of Sr (5.6 eV) and Zr (6.7 eV).

<sup>3</sup>The linewidth of In wasn't listed in reference 23. The value was approximated by using the values of Pd (10.2eV) and Ag (10.0 eV) .

<sup>4</sup>The observed resolution was taken from the calibration taken after three hours.

<sup>5</sup>The linewidth of Sn wasn't listed in reference 23. The value was approximated by using the values of Pd & Ag (10 eV). The next element listed was W (43 eV) giving an upper limit which is still insignificant compared the the observed resolution.



## 2. PXR Bandwidth Determination.

The PXR bandwidth is determined in the same manner, that is

$$\Gamma_{\text{PXR}}^2 = \Gamma_{\text{obs}}^2 - \Gamma_{\text{det}}^2, \quad (35)$$

where  $\Gamma_{\text{PXR}}$  is the bandwidth of the PXR spectral line. The units are in keV. Table 11 lists the values of the observed resolution for a given energy, the calculated PXR bandwidth for the various single angle experiments and the expected value as calculated using equation (27).

Note that the observed linewidths in Table 10. vary with the various experiments. These variation are due to the changes made in the experimental procedure. That is the May 5th data is much wider due to poorer resolution of the ORTEC 450 amplifier. This amplifier was replaced by the TENNELEC TC 244 amplifier following that experiment. The July 8th data used an upgraded version of the PHA software which has digital stabilization features which compensate for drift and therefore reduces the observed linewidth. Notice that in spite of these changes in detector resolution, the PXR linewidths do not vary significantly, since the changes in the detector resolution are accounted for by equation (35).

TABLE 11. LIST OF OBSERVED RESOLUTION AND CALCULATED PXR BANDWIDTH FOR THE VARIOUS SINGLE ANGLE EXPERIMENTS.

Date	Energy (keV)	$\Gamma_{\text{obs}}$ (keV)	$\Gamma_{\text{PXR}}$ (keV)	Theory
5 May	4.4	0.64	-	0.17
	9.8	0.67	-	0.35
	14.9	0.77	0.45	0.52
	20.0	0.95	0.76	0.70
	25.1	0.86	0.68	0.87
	30.3	1.20	1.10	1.0
8 May	4.9	.35	0.15	0.17
	9.5	0.41	0.23	0.35
	14.2	0.49	0.32	0.52
	19.0	0.53	0.35	0.70
	23.8	0.57	0.39	0.87
	28.6	0.63	0.46	1.05

TABLE 11. cont.

Date	Energy (keV)	$\Gamma_{\text{obs}}$ (keV)	$\Gamma_{\text{PXR}}$ (keV)	Theory
7 July 22.5 degrees	4.8	0.47 <sup>6</sup>	0.34	0.17
	9.8	0.54 <sup>4</sup>	0.39	0.35
	14.3	0.63 <sup>4</sup>	0.38	0.52
	19.1	0.54 <sup>4</sup>	0.30	0.70
	24.0	1.02 <sup>7</sup>	0.90	0.87
7 July 23 degrees	5	0.47	0.34	0.17
	15	0.61	0.42	0.50
	25	0.82	0.65	0.83
8 July	5	0.37		0.17
	15	0.52	0.43	0.52
	25	0.26 <sup>5</sup>	0.20	0.87

Once the resolution and the net area is determined at the front face of the crystal, these values can be compared to the theoretical values. Since, for most of these experiments, there was no reference tin peak from which to compute the LINAC current, the analysis is accomplished by comparing the experimental ratios of the intensity (area) of a given order to the intensity of the first order with that calculated from theory. The single angle experiments were all obtained in the far region, therefore the theoretical ratios are determined by integrating equation (26) over the field of view, and the bandwidth is based on  $\Delta\theta_x$  and not the FWHM of  $J_2$ . The experimental ratios are listed in Table 9 above. As described in Chapter II, section C, the calculations must be performed over the limited field of view.

Figure 2 in Chapter II section C illustrates how the aperture in the far case is less than the FWHM of  $J_2$ . The theoretical ratios are calculated by integrating equation (26) over the field of view for each order then taking the ratio of the number for a given order to the first order. Since the effects of mosaic spread and multiple scattering aren't well

<sup>6</sup>The observed resolution was taken from the calibration taken after three hours.

<sup>7</sup>Estimated due to overlap of fifth order peak with the tin peak in the PXR spectrum.

understood, the theoretical values with and without these effects are included for comparison. These ratios are shown in Table 12 along with the experimental ratios. The experimental ratios are plotted as a function of order in Figure 22. The experimental values are compared with the theory by dividing the experimental value by the theoretical value and is also shown in Table 12.

TABLE 12. COMPARISON OF EXPERIMENTAL AREA RATIOS,  $I(n)/I(1)$ , WITH THEORY WITH AND WITHOUT THE EFFECTS OF MULTIPLE SCATTERING AND MOSAIC SPREAD.

Date	n	Experimental Data		Theory without scattering or mosaic spread		Theory with scattering and mosaic spread	
		Net Area (counts)	Ratio	Ratio	$\frac{\text{Exp}}{\text{theory}}$	Ratio	$\frac{\text{Exp}}{\text{theory}}$
5 May	1	15900	1	1	1	1	1
	2	16400	1.03	0.27	3.8	0.09	11.4
	3	6600	0.42	0.05	8.4	0.01	42
	4	2700	0.17	0.01	17	0.003	57
	5	800	0.05	0.005	10	0.001	50
8 May	1	30200	1	1	1	1	1
	2	31700	1.05	0.27	3.9	0.09	11.7
	3	15600	0.52	0.05	10.4	0.01	52
	4	7400	0.25	0.01	17	0.003	57
	5	3900	0.13	0.005	10	0.001	50
7 July 22.5°	1	27000	1	1	1	1	1
	2	22900	0.85	0.27	3.1	0.09	9.4
	3	9200	0.34	0.05	6.8	0.01	34
	4	3900	0.14	0.01	10	0.003	47
	5	1200	0.04	0.005	8	0.001	40
7 July 23°	1	22500	1	1	1	1	1
	2	25500	1.13	0.02	56.5	0.11	10.3
	3	11200	0.50	0.004	125	0.02	25
	4	4900	0.22	0.001	220	0.004	55
	5	2200	0.10	0.0003	330	0.001	1000
8 July	1	34600	1	1	1	1	1
	2	29300	0.85	0.27	3.1	0.08	10.6
	3	13800	0.40	0.05	8	0.01	40
	4	5700	0.16	0.01	16	0.003	53
	5	1300	0.04	0.005	80	0.001	40

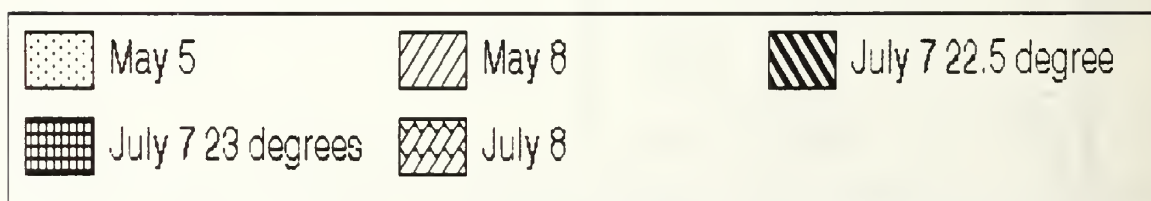
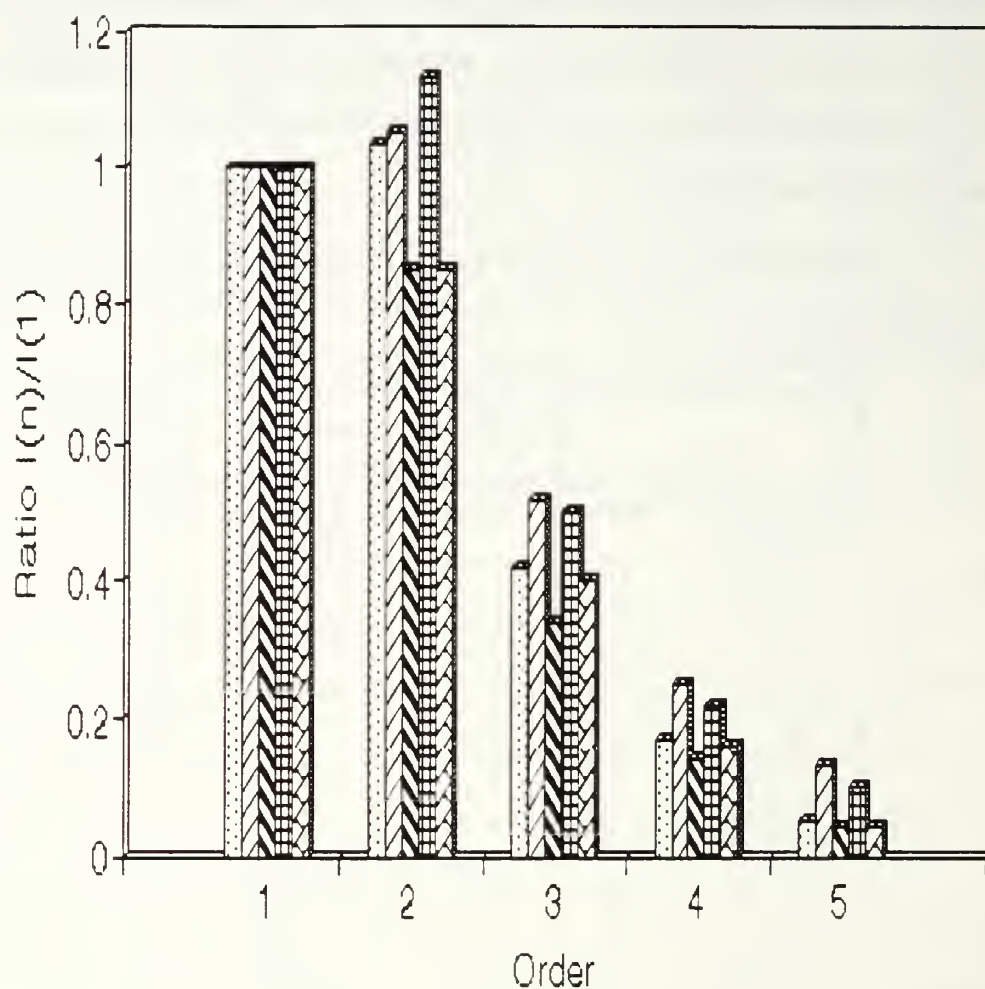


Figure 22. Plot of Area ratio of nth order peak to first order peak vs order for the four experiments conducted near the Bragg angle of 22.5 degrees.

Notice that the experimental ratios are consistently larger than theory, and the inclusion of mosaic spread and multiple scattering makes the discrepancy even larger, thus showing



that equation (21) may be preferred over equation (20). This indicates that the theory is inadequate to explain the observed results. It also indicates that it is important to look at the convolution of the electron beam divergence with the multiple scattering effect for an even better estimation of the effect of multiple scattering.

### 3. Calculations of Absolute PXR Yield (Photons/Electron)

In addition to comparing the intensity ratios, for the 7 and 8 July experiments the number of photons per electron can be calculated. The Linac current can be determined by using the yield of the Tin fluorescent peak using the following equation

$$I_{\text{LINAC}} = \frac{\left( \frac{\text{Area}_{\text{Tin}}}{\text{time}} \right) (AW_{\text{Tin}})}{\sigma_{\text{Tin}} \left( \frac{\Omega_{\text{det}}}{4\pi} \right) \rho(N_a) f_{\text{dex}}(t) \epsilon(a)} , \quad (36)$$

where  $I_{\text{LINAC}}$  is the calculated beam current,  $\text{Area}_{\text{Tin}}$  is the Area of the tin peak at the detector (from the pulse height analyzer), time is the collection time of the PXR spectrum,  $AW$  is the atomic weight,  $\sigma$  is the electron interaction cross section ( $1.0 \text{ e-}26 \text{ m}^2$ )[Ref. 24],  $\Omega_{\text{det}}$  is the solid angle subtended by the detector ( $2 \times 10^{-4} \text{ sr.}$ ),  $\rho$  is the density of the target ( $2.260 \text{ g/cm}^3$ ),  $N_a$  is Avogadro's number,  $f_{\text{dex}}$  is the de-excitation transition probability ( $0.712$ )[Ref. 25],  $t$  is the thickness of the target ( $2.98 \times 10^{-5} \text{ m}$  for 22.5 degrees),  $\epsilon$  is the relative detector efficiency at the tin peak energy ( $0.9$  for these experiments) and  $a$  is the total attenuation factor of photons (through the effective thickness of tin, the effective thickness of the mosaic crystal, the kapton window, the air gap and the beryllium window of the detector ( $0.763$  for 22.5 degrees.))[Ref. 21]).

The electron interaction cross sections [Ref. 24] were obtained for 85 MeV electrons. The transition probabilities [Ref. 25] include both the K-L11 and the K-L111 de-excitation probabilities. The attenuation coefficients were obtained using XCOM at the known de-excitation energy of Tin. The details of these calculations may be found in reference 17.



Using the LINAC current in electrons per second, the intensity of the PXR in counts as listed in Table 9 and the data collection time, the number of photons can be calculated as;

$$\frac{\left( \frac{\text{PXR Area}}{\text{Time}} \right)}{\text{LINAC Current}} \quad (37)$$

These values are shown in Table 13 along with the calculated currents.

TABLE 13. COMPARISON OF THE EXPERIMENTAL NUMBER OF PHOTONS PER ELECTRON TO THEORY WITH AND WITHOUT THE EFFECTS OF MOSAIC SPREAD AND MULTIPLE SCATTERING.

DATE [current (amps)]	N	EXP DATA	THEORY WITH SCATT	EXP THEORY	THEORY WITHOUT SCATT	EXP THEORY
7 July 22.5°	1	1.57e-6	3.64e-8	43	1.39e-7	11
[1.74e-13]	2	1.48e-6	3.14e-9	471	3.69e-8	40
	3	5.92e-7	4.24e-10	1400	7.14e-9	83
	4	2.62e-7	1.07e-10	2450	1.98e-9	132
	5	5.6e-8	3.56e-11	2120	6.85e-10	110
7 July 23 °	1	1.60e-6	3.03e-8	53	6.24e-8	26
[2.21e-13]	2	1.81e-6	3.38e-9	536	1.27e-8	143
	3	7.94e-7	5.03e-10	1580	2.30e-9	345
	4	3.48e-7	1.29e-10	2700	6.24e-10	558
	5	1.56e-7	4.33e-11	3600	2.13e-10	732
8 July	1	1.58e-6	3.63e-8	44	1.39e-7	11
[2.67e-14]	2	1.34e-6	3.13e-9	428	3.69e-8	36
	3	6.30e-7	4.23e-10	1490	7.12e-9	89
	4	2.60e-7	1.06e-10	2450	1.98e-9	131
	5	5.94e-8	3.55e-11	1670	6.83e-10	87

The number of photons per electron are plotted vs order for these three dates in Figure 23. Note that the data is consistently larger than the theory, as seen with the ratios. Figure 24 is a plot of the number of photons per electron for experimental data, and the theory with and without the effects of multiple scattering and mosaic spread. With the actual number of photons per electron there is more information than with the ratios alone. First it is clear that the data is much larger than expected. Second, the difference between the data and the theory gets larger with order, which explains why the error in the ratios increased with order. Because of overlap, a peak fitting routine was used to obtain the area under the fifth order PXR and tin peaks. [Ref. 26]

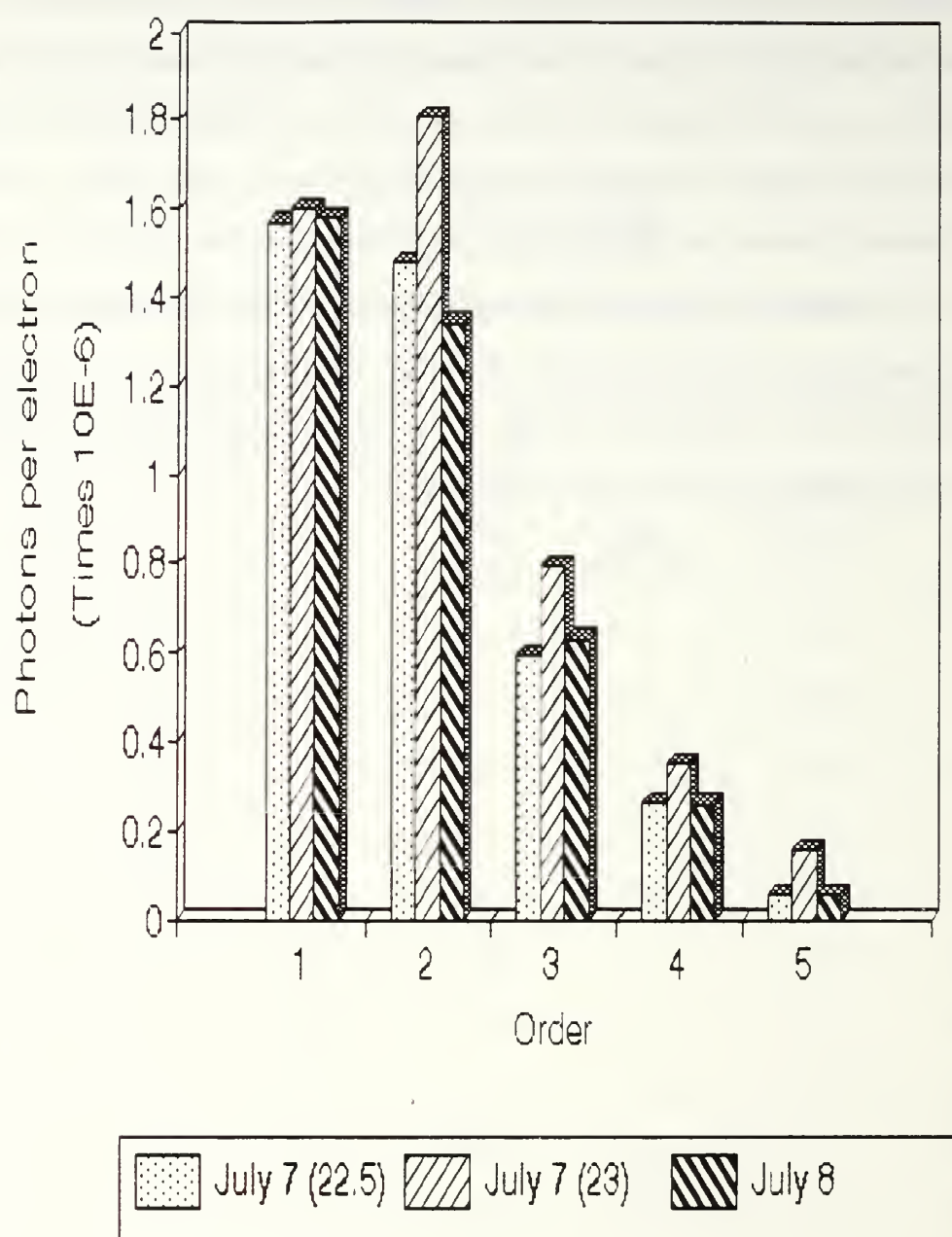


Figure 23. Plot of the absolute number of photons per electron vs order for the three experiments near the Bragg angle of 22.5 degrees with a tin peak used to determine the LINAC current.

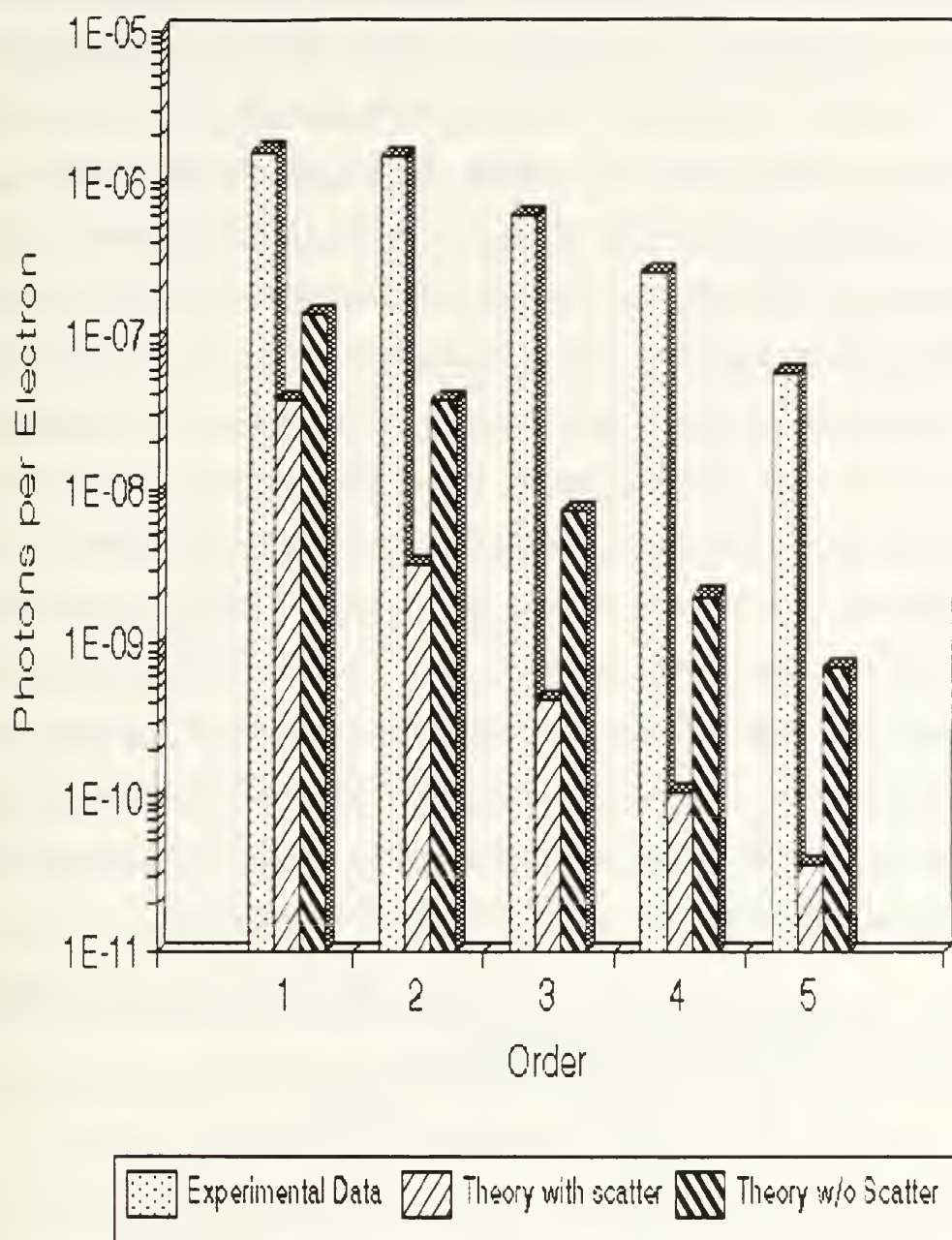


Figure 24. Plot of number of photons per electron vs angle for the 7 July 22.5 degree data along with the theory both with and without the effects of multiple scattering and mosaic spread.

### C. PXR DATA COLLECTION (DISPLACEMENT FROM THE BRAGG ANGLE)

Two sets of "rocking data" were obtained. For these experiments rocking data refers to a fixed detector angle of 45 degrees with respect to the beam line, and the crystal angle is rocked about the Bragg angle of 22.5 degrees. The first was obtained on June 5, 1992. Data was obtained using the ORTEC SiLi detector and the TENNELEC amplifier. This is the far region. The linear gate was set at 5  $\mu$ s wide with a delay time of 30.6  $\mu$ s from  $T_0$  (the LINAC start sequence time). The air gap thickness was 1.1 cm. Brief spectra were obtained starting at 22.5 degrees for 200 seconds. Then the edges were determined by obtaining spectra at 26.5 and 18.5 degrees, both of which showed no PXR peaks. To obtain an estimate of the angle giving the largest count rate three more angles were set for 200 seconds each. The results are shown in Table 14, where "counts" is the net number of counts in the peak channel of the  $n=1$  peak. The count rate appeared to increase upon rotation from 22.5 degrees to lower angles with the maximum near 22.1 degrees. Angles were selected assuming 22.1 degrees to be the angle which produced the maximum count rate. (This doesn't agree with theory where 22.5 degrees should be the maximum, but due to uncertainties in the crystal orientation this was assumed within error).

TABLE 14. NUMBER OF COUNTS VS. ANGLE FOR 200 SECOND SPECTRUM OBTAINED ON JUNE 5, 1992 (FAR REGION).

Angle	counts
22.5	13
26.5	0
18.5	0
22.3	15
22.1	17
21.9	10



The crystal angle was varied starting at 19.1 degrees, and increased by 1.0 degree. When the angle was within 1 degree of the assumed maximum the angle was increased by 0.5 degrees. The spectra were obtained for 30 minutes each. As seen in Table 15 the number of counts in the peak channel in the  $n=1$  peak continued to increase beyond 22.1 degrees. The angle was increased in 0.5 degree steps until the number of counts in the peak channel were comparable to the number at 21.1 degrees, after which 1.0 degree steps were taken until very little  $n=1$  peak showed. These uncorrected PXR spectra are shown in Figures 25 & 26. Full scale spectra can be found in Appendix A. This data shows that the maximum count rate is obtained near 22.5 degrees as expected.

On July 22, 1992, rocking data was obtained using the Canberra (SiLi) detector and the TENNELEC amplifier. This is the near region. The LINAC was tuned to 95.9 MeV. The air gap was 1.1 cm. Due to a set up error the data collection time was not fixed and therefore varied at different angles but was approximately 45 minutes. A longer time was used than on June 5<sup>th</sup> since the Tin peak wasn't as well defined. The angles were taken to be the same as those used on June 5<sup>th</sup> for comparison purposes with the exception that no spectrum was collected at 19.1 degrees. These uncorrected PXR spectra are shown in Figures 27 & 28. Full scale spectra can be found in Appendix A.

#### **D. PXR ANALYSIS (DISPLACEMENT FROM THE BRAGG ANGLE)**

The analysis of the data involved three issues. The first is the value of the PXR energy versus angle, the second is the intensities versus angle and the last is the number of photons per electron versus angle.

To determine the PXR energy versus angle the original spectra were analyzed using the pulse height analyzer to determine the centroid of each peak, including the centroid of the tin peak. The value of the first order centroid was plotted vs. angle, along with the theoretical value. There appeared to be a discrepancy between the theory and the data. Next the tin peak centroid was plotted vs. angle. Note that theoretically the tin peak

TABLE 15. NUMBER OF COUNTS VS. ANGLE FOR 200 SECOND SPECTRUM OBTAINED ON JULY 22, 1992 (NEAR REGION).

Angle	Counts
19.1	negligible
20.1	13
21.1	25
21.6	49
22.1	98
22.6	203
23.1	149
23.6	62
24.1	45
24.6	36
25.6	25
26.6	negligible

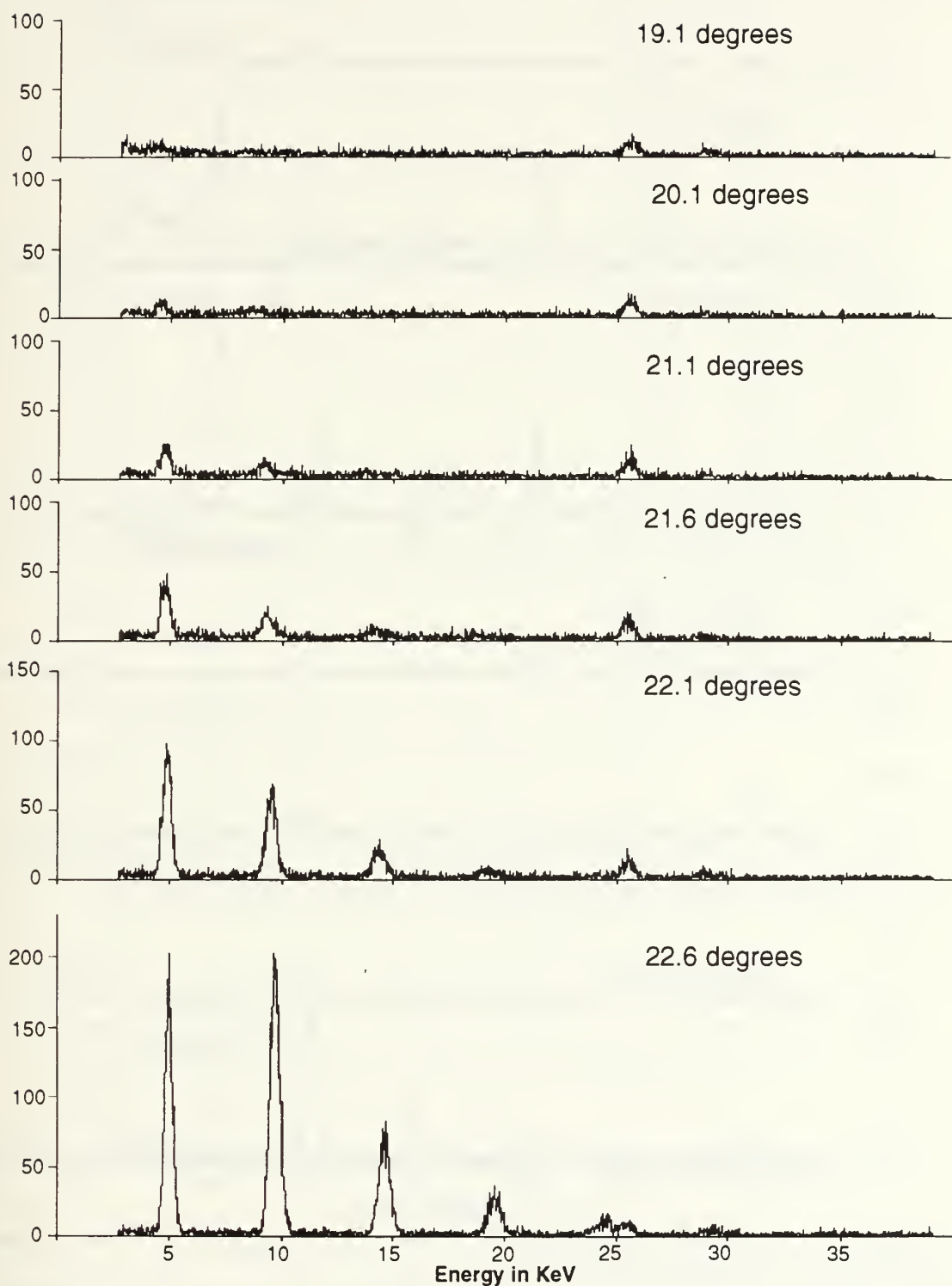


Figure 25. PXR spectra from the {002} planes of carbon graphite for the "far region", obtained on June 5th at angles 19.1-22.6 degrees.

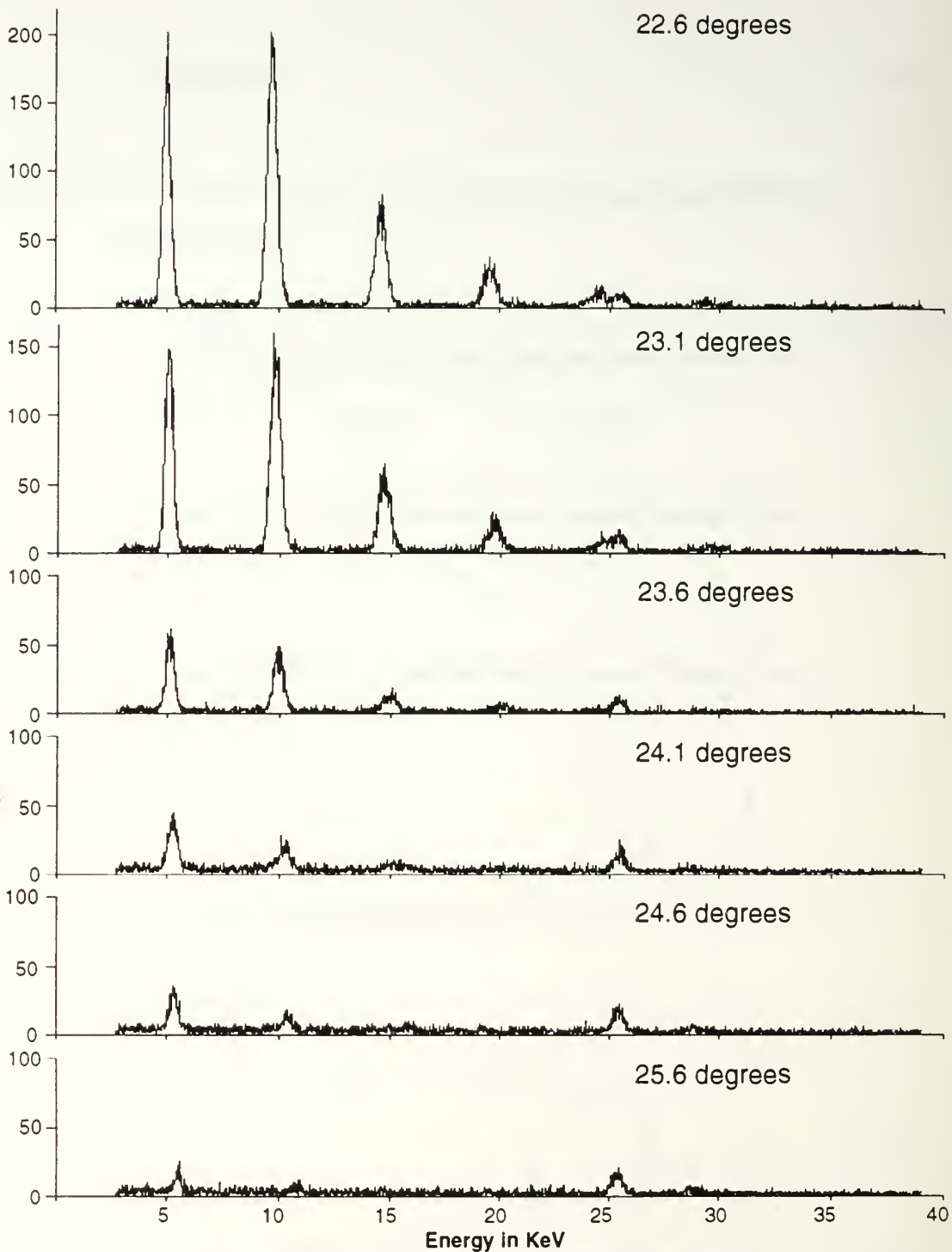


Figure 26. PXR spectra from the {002} planes of carbon graphite for the "far region", obtained on June 5th at angles 22.6-25.6.

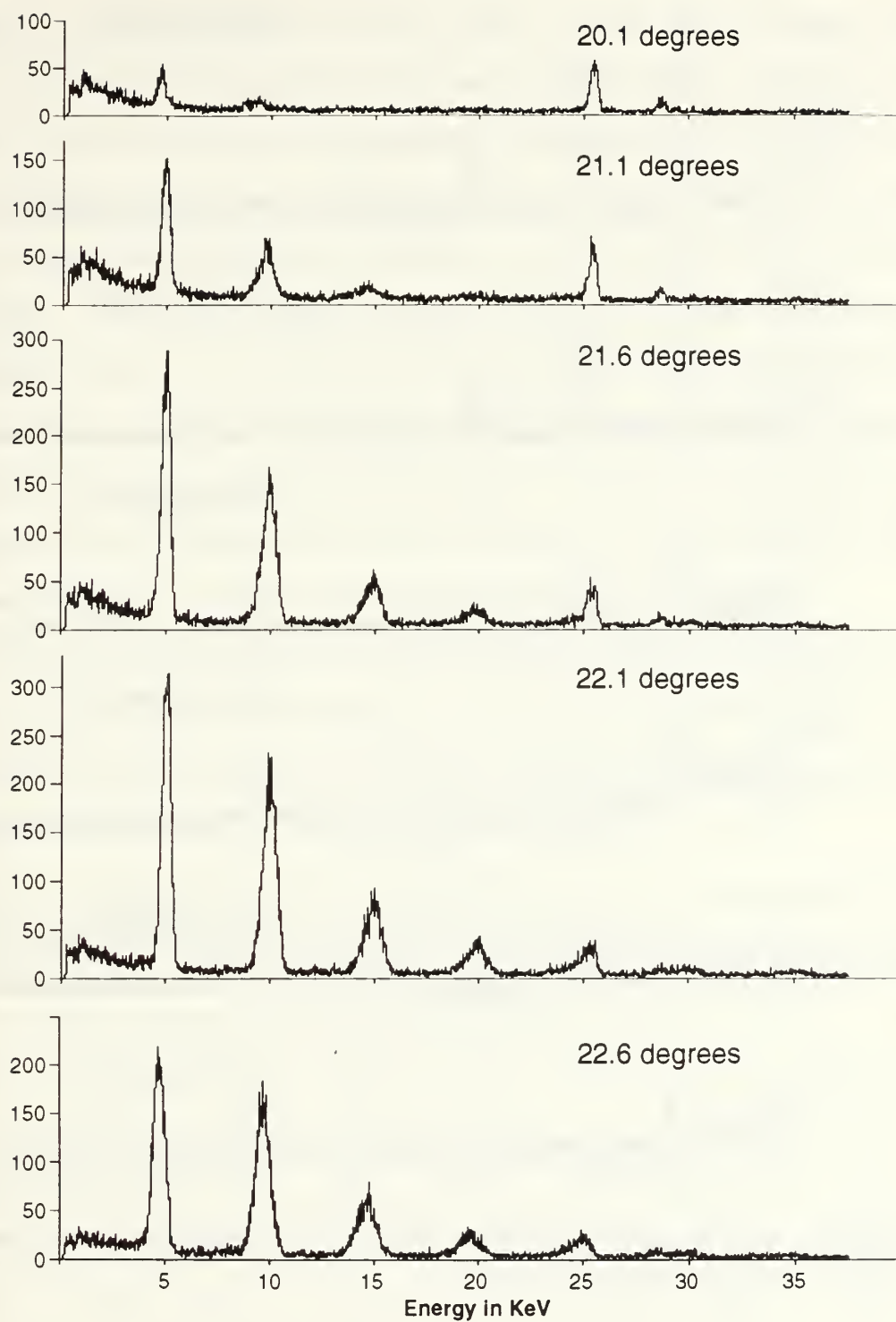


Figure 27. PXR spectra from the {002} planes of carbon graphite for the "near region", obtained July 22nd at angles 20.1-22.6.



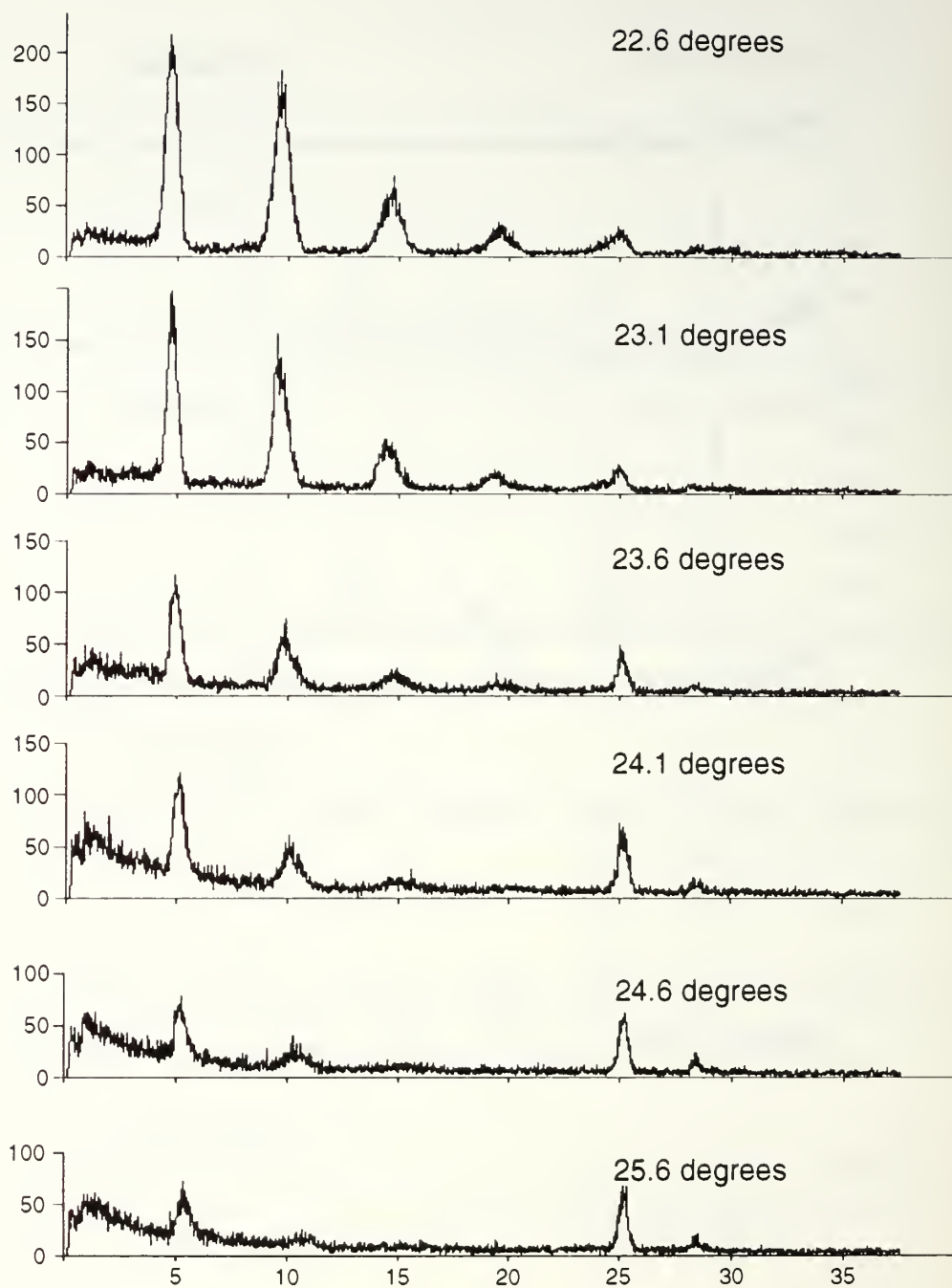


Figure 28. PXR spectra from the {002} planes of carbon graphite for the "near region", obtained July 22nd at angles 22.6-25.6.

position in the spectrum should not depend on angle. The fact that the tin peak's position was not constant with angle showed that there was some shifting in energy with time. Taking the difference between the experimental tin peak centroid and the known tin de-excitation energy (25.1955KeV) and subtracting this difference from the PXR centroid, this corrected PXR centroid was compared with theory and showed much better agreement. These plots are shown in Figures 29 & 30 for the June 5<sup>th</sup> and July 22<sup>nd</sup> experiments respectively. The scale on the left refers to the PXR energies. The original PXR centroids are plotted as "pxr centroid", the PXR centroid minus the difference in the true tin and known tin is plotted as "corrected cent". The experimental tin peak is shown using the scale on the right, with the known tin energy plotted as a dotted line. Note that the same increments were used on the two scales for comparison purposes.

This also explains the difference between the expected values of  $E(n)/E(1)$  equal to  $n$  and the actual values as listed in Tables 2-6. This is further illustrated in Table 16. The (\*) indicates corrected values based on the shift in the Tin peak centroid energy from the known de-excitation energy. This shift is listed as "Tin Shift".

TABLE 16. COMPARISON OF RAW ENERGY RATIOS TO THE RATIOS OF THE SHIFTED ENERGIES FOR THE 5 JUNE ROCKING DATA.

ANGLE	E(1)	E(2)	E(1)/E(2)	TIN SHIFT	E(1)*	E(2)*	E(1)* / E(2)*
21.1	4.73	9.23	1.95	0.27	4.46	8.96	2.01
21.6	4.78	9.34	1.95	0.22	4.56	9.12	2.00
22.1	4.84	9.52	1.97	0.26	4.58	9.26	2.02
22.6	4.94	9.72	1.97	0.23	4.71	9.49	2.01
23.1	4.98	9.81	1.97	0.13	4.85	9.68	2.00
23.6	5.02	9.95	1.98	0.17	4.85	9.78	2.02
24.1	5.21	10.17	1.95	0.18	5.03	9.99	1.99
24.6	5.23	10.40	1.99	0.18	5.05	10.22	2.02

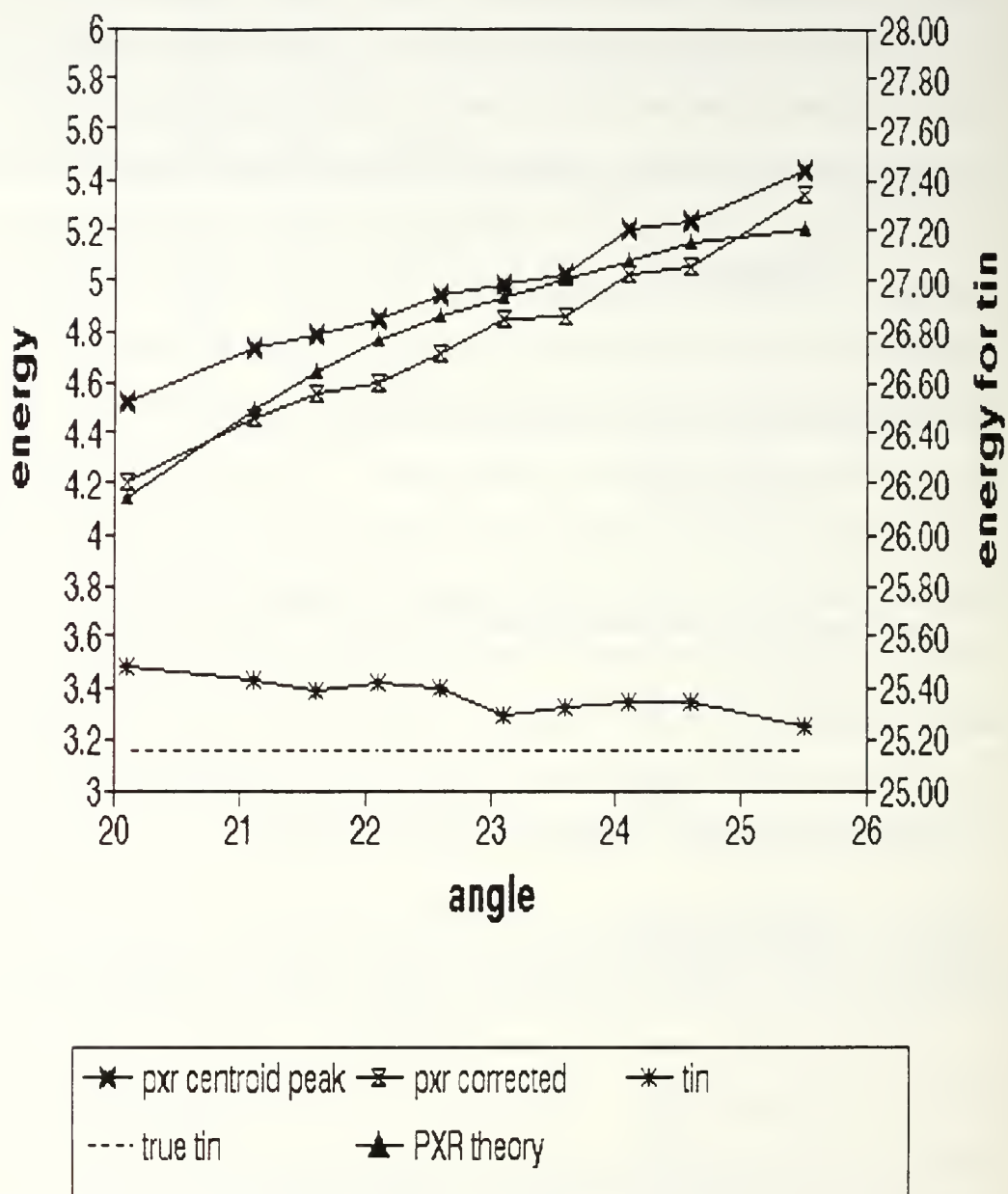


Figure 29. Plot of PXR first order energy original data, corrected data and theory vs. angle, tin centroid and theory for the June 5<sup>th</sup> experiment (far region).

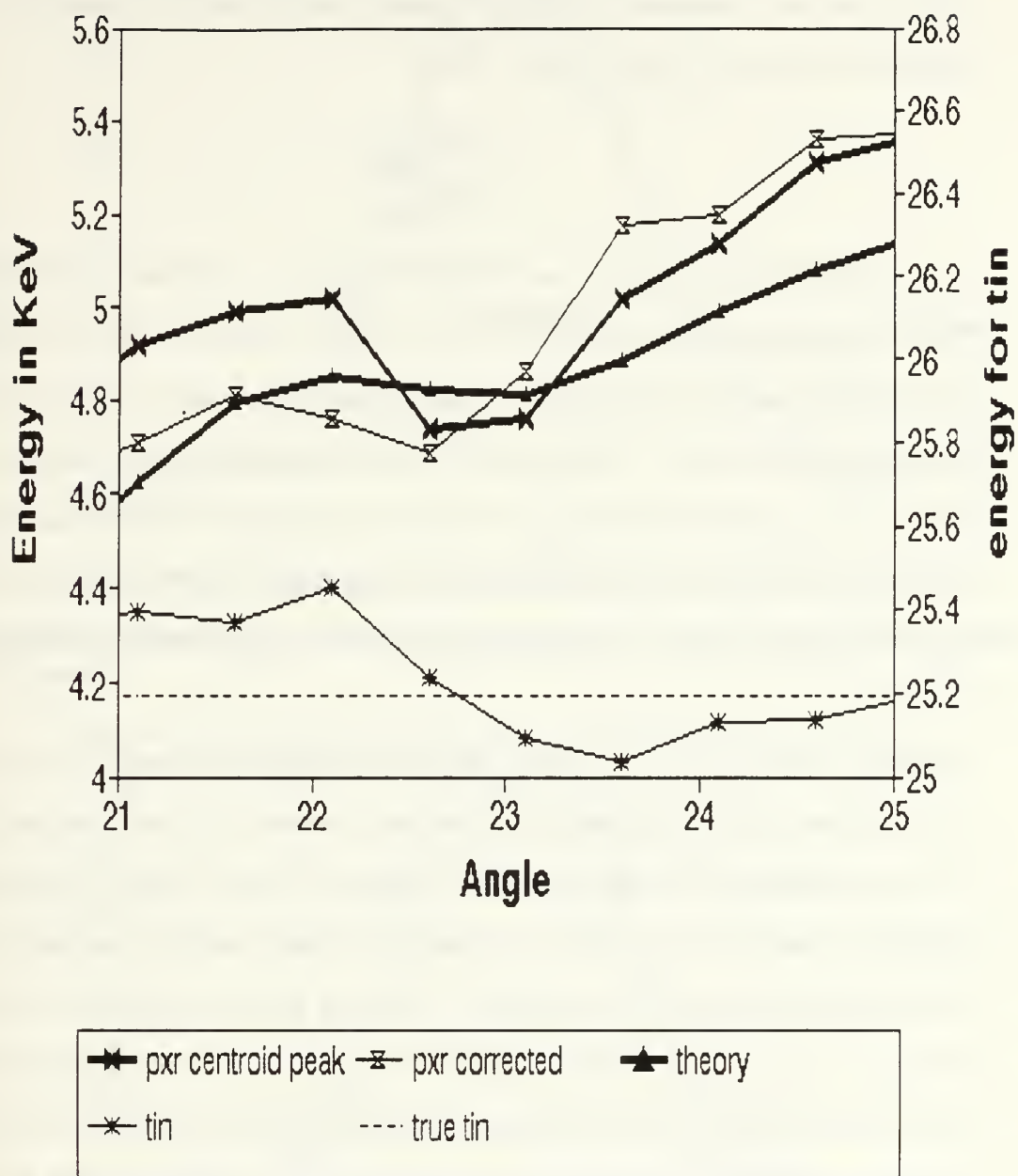


Figure 30. Plot of PXR first order energy original data, corrected data and theory vs. angle, tin centroid and theory for the July 22<sup>nd</sup> experiment (near region).

These values were computed by finding the energy centroid based on equations (23) and (24) within the limits of the field of view. That is:

$$\frac{\int x \frac{dN}{dE} dx}{\int \frac{dN}{dE} dx}, \quad (37)$$

where the integrals are computed over the field of view  $\Delta\theta_x$ . Figures 31-33 illustrate the effect of changing angles on the field of view. Figure 31 illustrates  $\Delta\theta_x$  for the far case near the Bragg angle, while Figure 32 is approximately one degree displaced from the Bragg angle for the far case. Notice that the effect of changing the crystal angle is to shift the field of view across the function  $J_2$ . The detector sees a slice of  $J_2$  and that slice shifts across  $J_2$  as the crystal angle changes from the Bragg angle. Figure 33 illustrates the field of view for the near case. Notice that the field of view is larger than the FWHM of  $J_2$  for this case.

Comparison of Figures 29 & 30 show that for the far region the detail of the function  $J_2$  is not important in the energy centroid calculations, however for the near region the detail of  $J_2$  has a definite effect on the calculations. The dip in Figure 30 near 23 degrees shows the effect of the dip of  $J_2$ . There is a larger discrepancy between the theory and the corrected data for the July 22nd experiment. This may be due to the small tin peak area and therefore a larger error in determining the tin peak centroid. Also, since the details of  $J_2$  have a larger effect, an error in the angle determination has a larger effect, and shifting the data by 1/4 degree would show better agreement with the corrected data and theory. Figures 34 and 35 shows a plot of the corrected values of the energies for the first three orders versus angle, along with the theoretical values for the June 5<sup>th</sup> and July 22<sup>nd</sup> experiments respectively. Note that on this scale the difference between theory and experiment is very small, although there is a larger difference at the smaller angles for the higher orders.



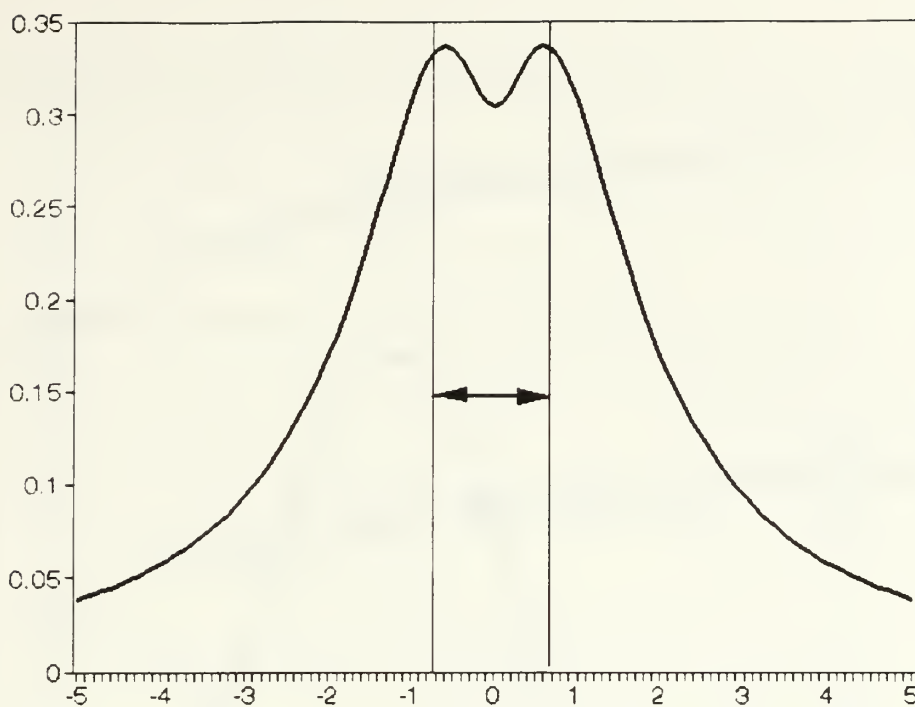


Figure 31. Illustration  $J_2$  and the field of view for the far region near the Bragg angle of 22.5 degrees.

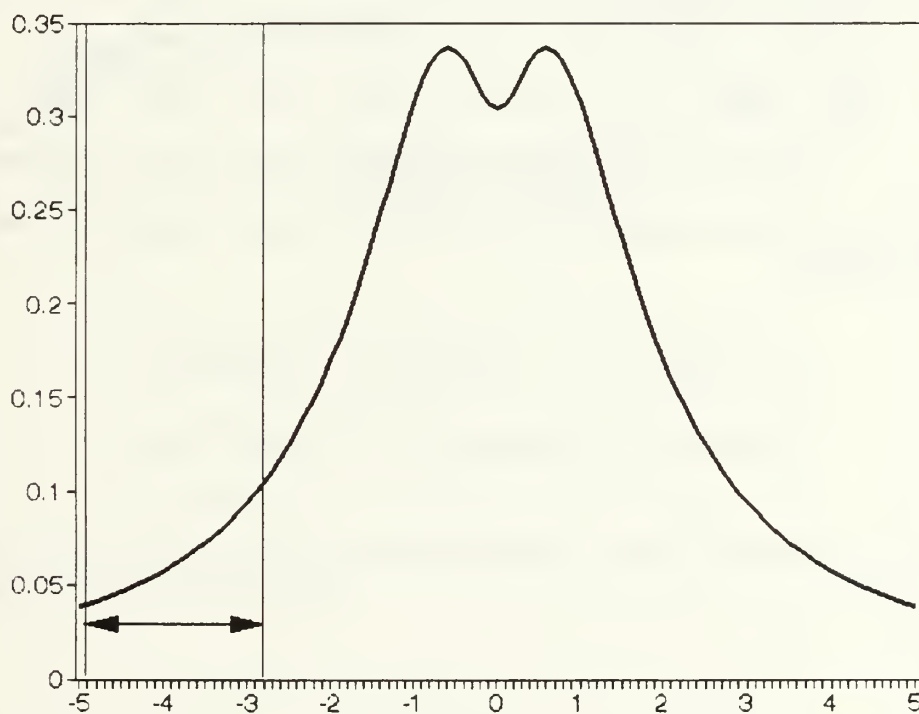


Figure 32. Illustration of  $J_2$  and the field of view for the far region approximately one degree displaced from the Bragg angle i.e. 23.5 degrees.

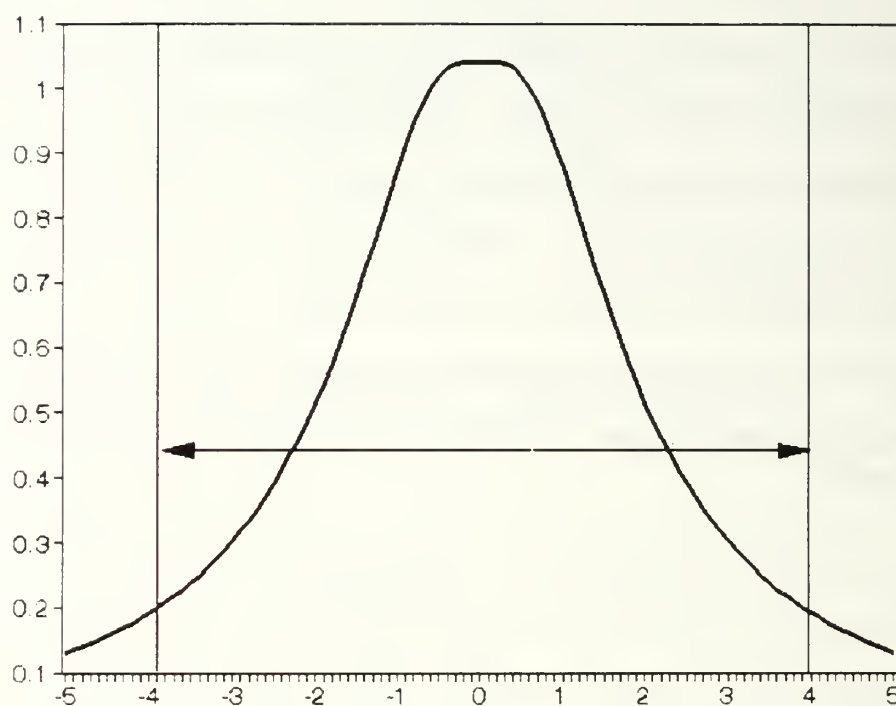


Figure 33. Illustration of  $J_2$  and the field of view for the near region near the Bragg angle of 22.5 degrees.

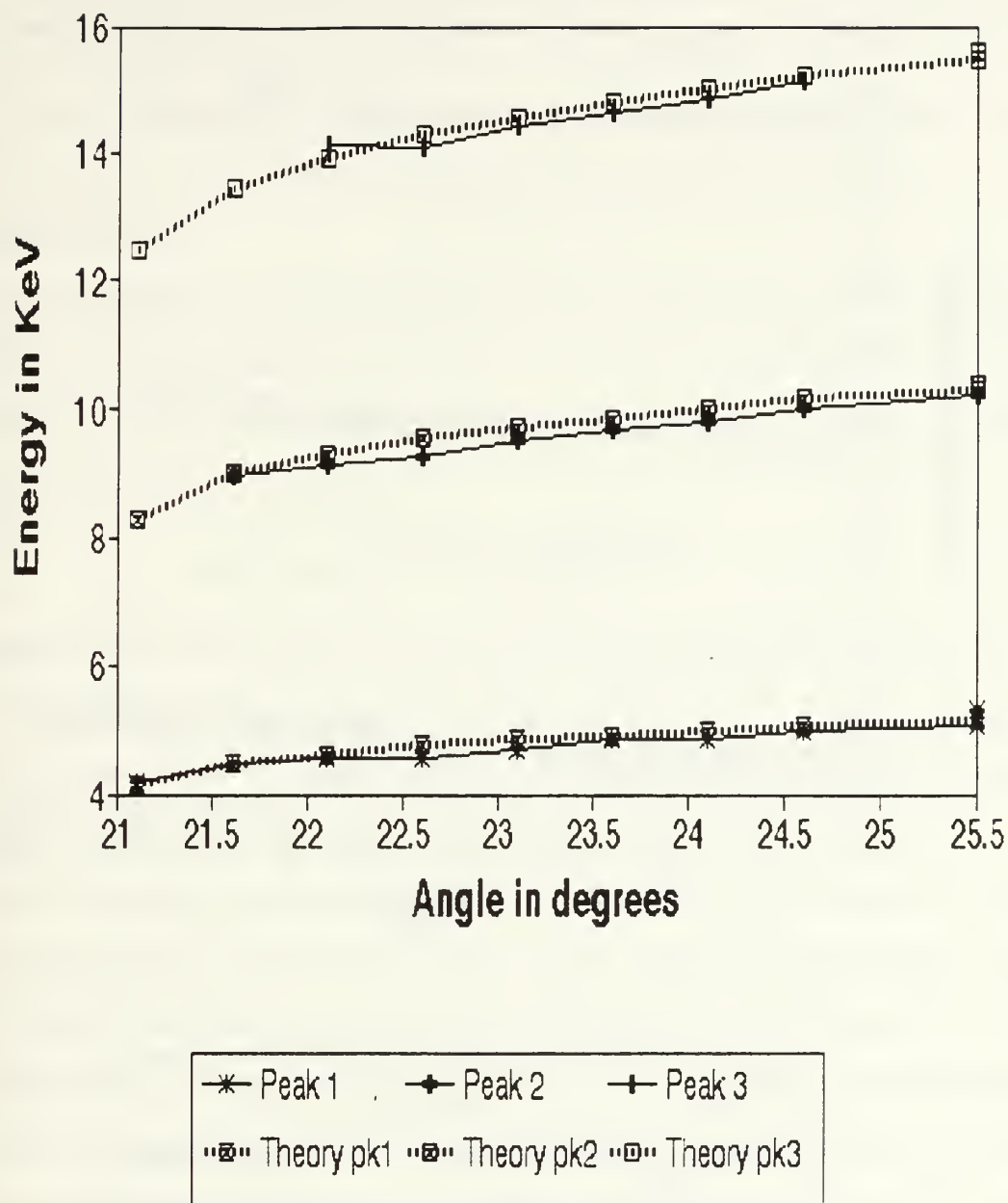


Figure 34. Plot of PXR corrected data and theory vs. angle for the first three orders for the June 5<sup>th</sup> experiment (far region).

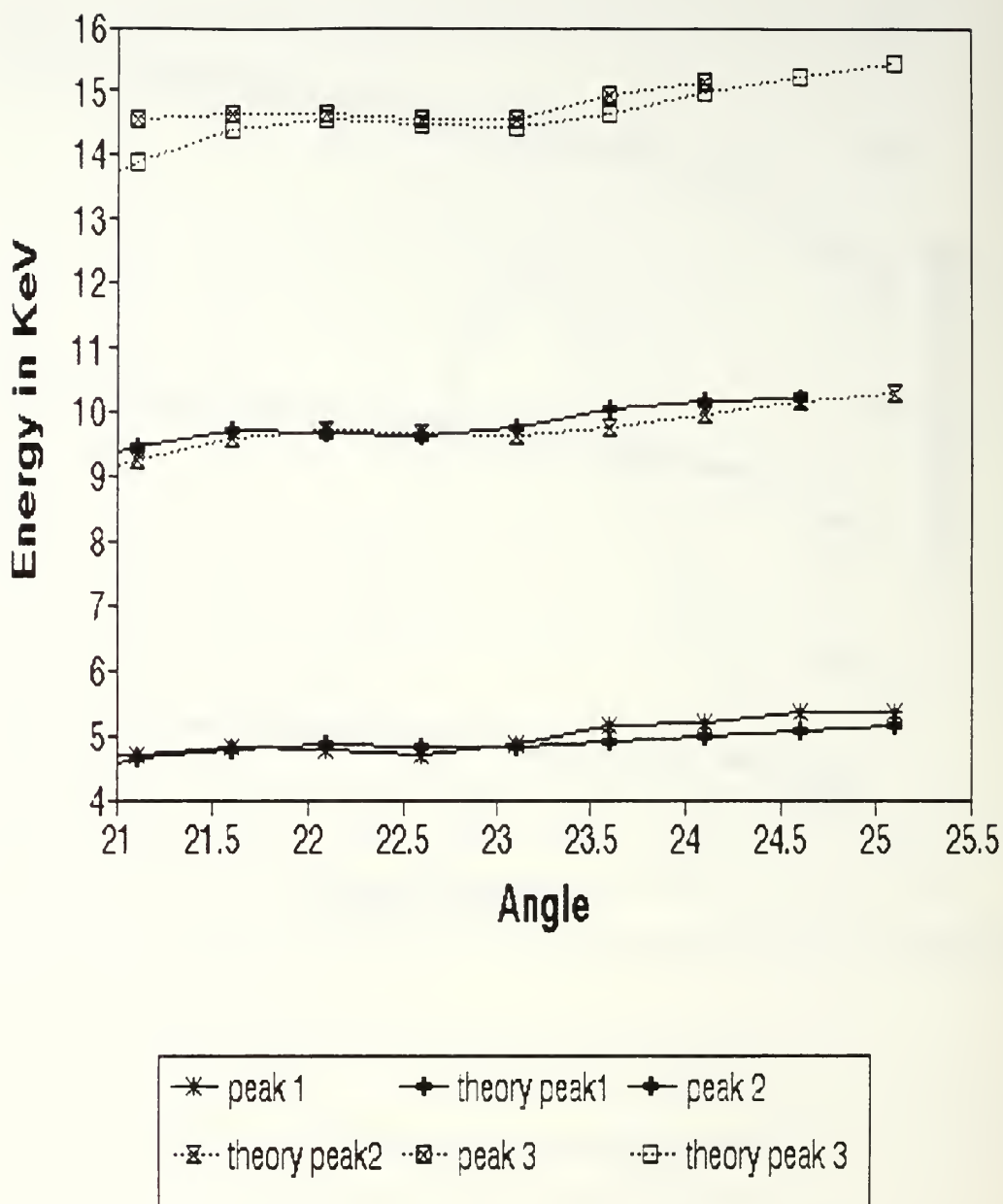


Figure 35. Plot of PXR corrected data and theory vs. angle for the first three orders for the July 22<sup>nd</sup> experiment (near region).

To compare the intensities at each angle the spectra obtained on June 5<sup>th</sup> and July 22<sup>nd</sup> at various angles needed to be normalized . Since the LINAC current was adjusted to maintain a machine pulse to PHA count rate ratio of about 6:1, and since angles closer to the Bragg angle of 22.5 degrees produce a larger number of x-rays, the current at these angles was lower.

For both dates, one spectrum was used to "strip" all the other spectra by shifting and scaling the spectrum based on the tin peaks. For the June 5<sup>th</sup> data the 19.1 degree spectrum was used and for the July 22<sup>nd</sup> data the 20.1 spectrum was used. The scaling factor was determined by equation 33.

$$\text{Scale Factor} = \frac{\text{Area Tin} - \text{Area Ref Tin}}{\text{Area Tin}} \quad (37)$$

where Area Tin is the actual tin area of the spectrum being scaled and Area Ref Tin is the corresponding area for the equivalent channels of the 19.1 or 20.1 degree spectrum tin peak. To account for the shift in tin energy, the spectrum was shifted and the reference was subtracted until the final spectrum showed an approximately zero net area.

After the spectrum were scaled and shifted, the June 5<sup>th</sup> data showed an average background of zero. For the July 22<sup>nd</sup> data there remained small amounts of LINAC induced noise, especially at the lower energies. Using QPRO spreadsheets and the XCOM program the counts were corrected channel by channel for attenuation through the Kapton window, the air gap and the Be window of the detector. The intensity (area) at the front face of the crystal was determined by summing over the channels of each peak. The areas are listed in Tables 16 and 17 for the far region (June 5<sup>th</sup> experiment) and the near region (July 22<sup>nd</sup> experiment) respectively. The scaled, shifted and corrected spectra for both the June 5<sup>th</sup> and July 22<sup>nd</sup> experiments can be found in Appendix A.

Using the scaled spectra, the intensity can be plotted as a function of angle for the various orders. Figures 36 and 37 show the scaled area intensities vs. angle for the June 5<sup>th</sup> and July 22<sup>nd</sup> experiments respectively. Note that the second order peak is larger than



TABLE 16. SCALED AREA INTENSITIES FOR THE JUNE 5TH EXPERIMENT (FAR REGION).

ANGLE	n=1	2	3	4	5	6
21.1	335	-	-	-	-	-
21.6	820	360	100	-	-	-
22.1	1770	1190	410	80	-	-
22.6	7420	8420	3490	1500	790	160
23.1	6300	6510	2720	1220	640	300
23.6	1460	1120	360	85	-	-
24.1	730	350	100	-	-	-
24.6	540	170	-	-	-	-
25.6	200	-	-	-	-	-

TABLE 17. SCALED AREA INTENSITIES FOR THE JULY 22ND EXPERIMENT (NEAR REGION).

ANGLE	n=1	2	3	4	5
21.1	3850	1860	430	-	-
21.6	8680	5970	2120	765	-
22.1	13950	11225	5280	2350	900
22.6	18250	14910	6660	2830	1290
23.1	12475	10630	4580	1480	-
23.6	5040	3130	1200	-	-
24.1	2635	1215	-	-	-
24.6	2160	700	-	-	-
25.6	1670	-	-	-	-

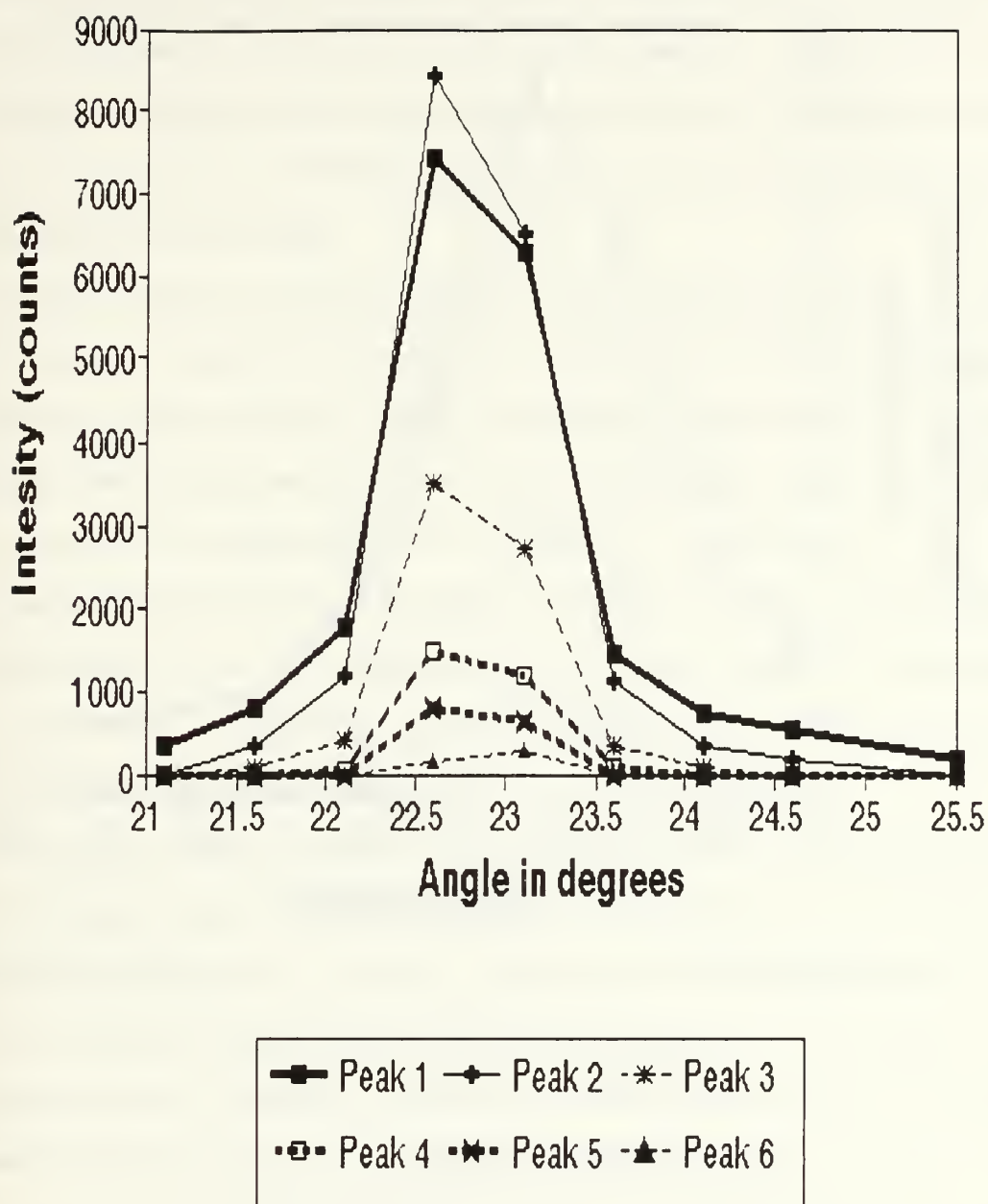


Figure 36. Plot of scaled area intensity for all orders versus angle for the June 5<sup>th</sup> experiment.

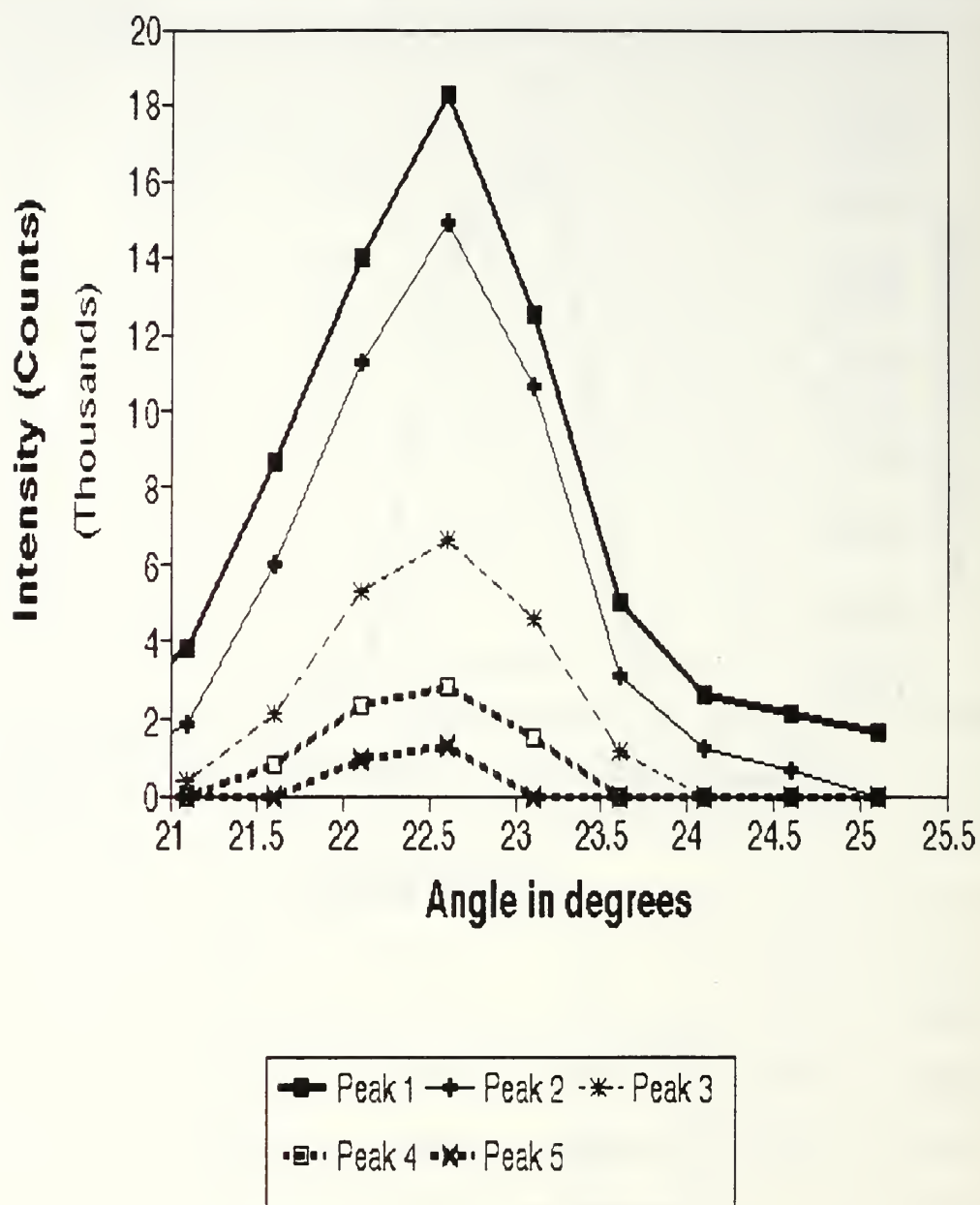


Figure 37. Plot of scaled area intensities for all orders versus angle for the July 22<sup>nd</sup> experiments.

the first order peak of the June 5<sup>th</sup> data at both 22.5 and 23 degrees, but it is smaller than the first order peak for all the angles of the July 22<sup>nd</sup> experiments . Also note that the plot as a function of angle for a given order is broader for the July 22<sup>nd</sup> experiment than for the June 5<sup>th</sup> experiment i.e., the PXR intensity falls off faster as a function of angle for the far region than for the near region.

The next comparison of the data with theory involved analysis using ratios. For the first order only, the intensities were divided by the first order intensity at 22.6 degrees (the angle with maximum intensity). Although the theoretical maximum is at 22.5 degrees, to compare with the experimental data, the number of photons per electron for each angle was divided by the theoretical value at 23 degrees. Figures 38 & 39 show these comparisons for the June 5<sup>th</sup> and July 22<sup>nd</sup> experiments respectively. Note that the June 5<sup>th</sup> data appears to be shifted by approximately 0.3 degrees, as shown by the dotted line. Also Note that the July 22<sup>nd</sup> data appears to be shifted in the other direction (compared to the June 5<sup>th</sup> data) by about 0.1 degrees.

These ratios compared one angle's first order intensity to that of the first order intensity at 22.6 degrees. A second comparison involves the ratio of any given order intensity to the first order intensity for a single angle. Tables 18 and 19 show these theoretical ratios with the experimental data in brackets for the far and near case respectively along with the experimental ratios in brackets. Figures 40 and 41 plot the experimental and theoretical values for  $I(2)/I(1)$  and for  $I(3)/I(1)$  for both the far and near region respectively. Note that there is little variation of the theoretical ratios with angle and that there is little difference between the theoretical values for the far and near case. The fact that the experimental values vary with angle with a maximum at  $\theta_B$  shows that searching for the maximum in this ratio can be used as a means to position the crystal at  $\theta_B$  if the LINAC current isn't monitored.

Lastly, the number of photons per electron for the data at each angle can be compared to the theory. The method of analysis is the same as that used in the single angle

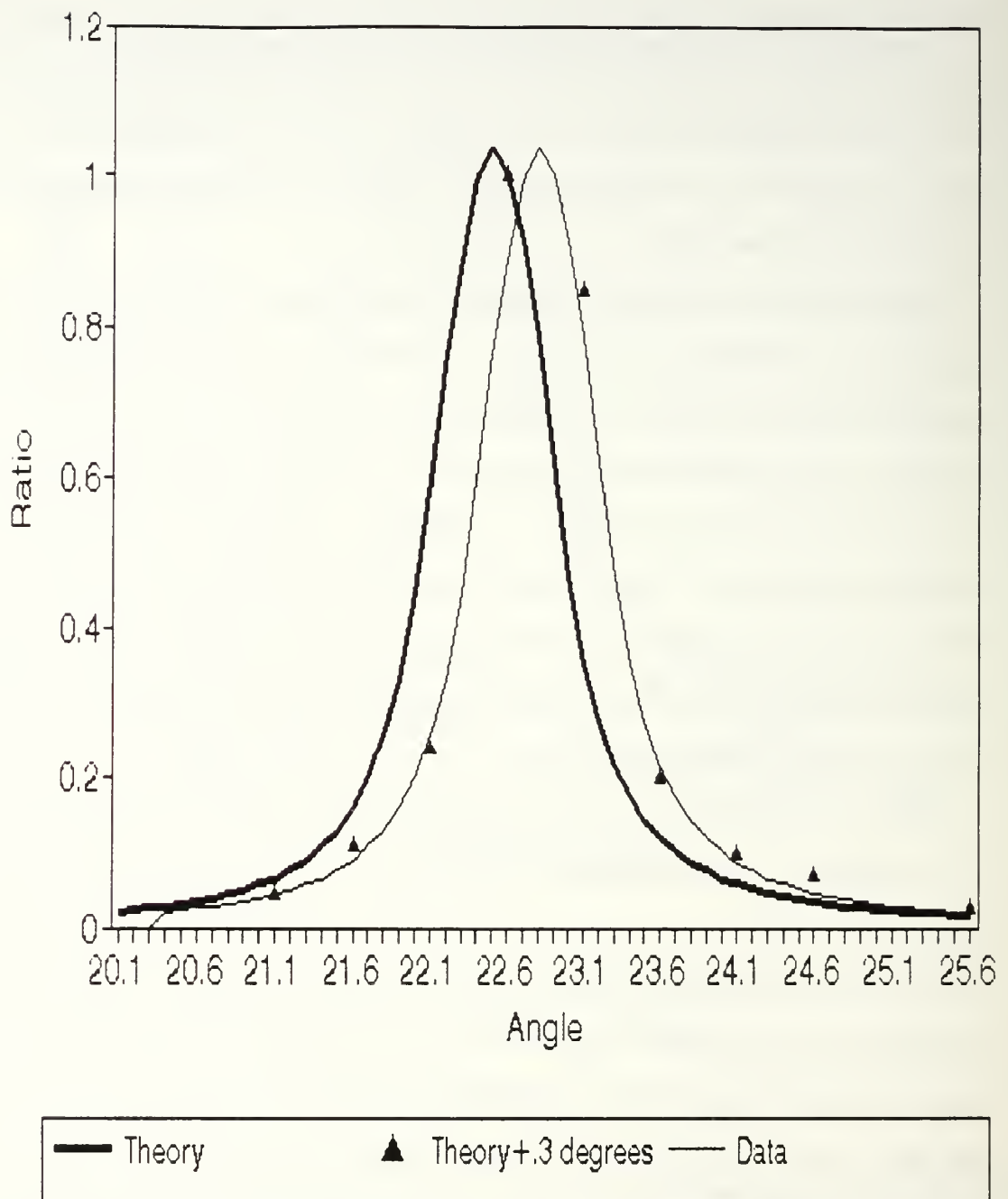


Figure 38. Plot of scaled area intensity divided by the area of 22.6 degrees for the first order versus angle, the theoretical ratio versus angle and the shifted theoretical ratio for the June 5<sup>th</sup> experiment (far region).



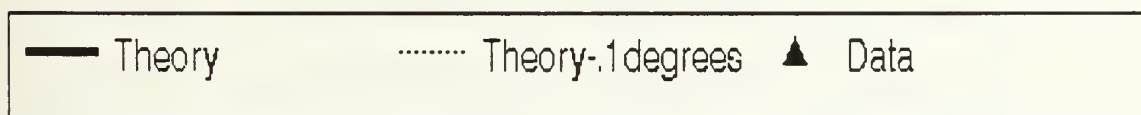
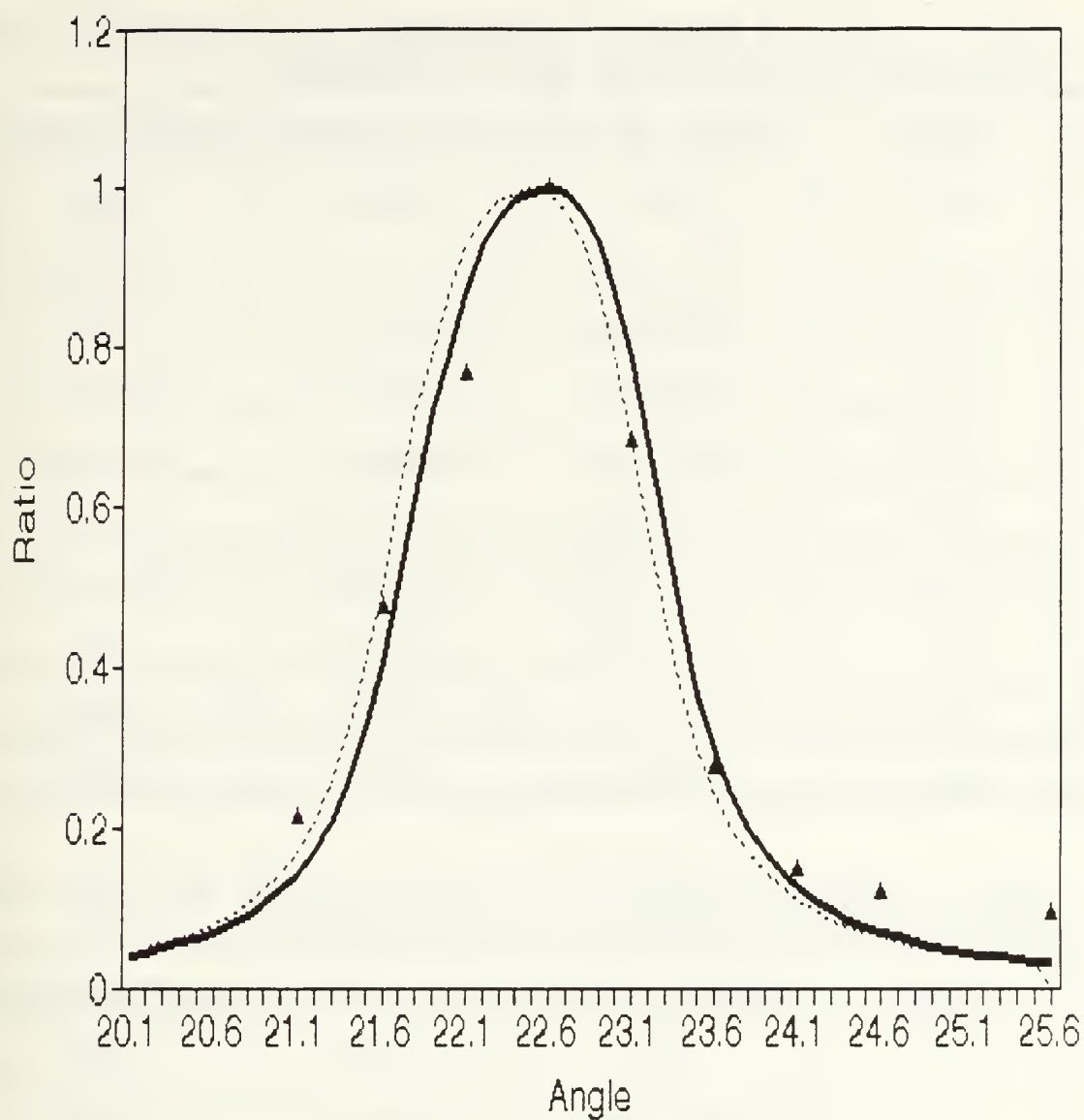


Figure 39. Plot of scaled area intensity divided by the area of 22.6 degrees for the first order versus angle and the theoretical ratio versus angle for the July 22<sup>nd</sup> experiments (near region).

TABLE 18. RATIO OF INTENSITY TO THE INTENSITY OF THE FIRST ORDER FOR VARIOUS ANGLES FOR THE JUNE 5<sup>th</sup> EXPERIMENT.

ANGLE	I(2)/I(1); [DATA]	I(3)/I(1); [DATA]	I(4)/I(1); [DATA]
20.1	0.184	0.034	0.009
21.1	0.185; [0.51]	0.034	0.009
21.6	0.188; [0.44]	0.034; [0.12]	0.009
22.1	0.214; [0.67]	0.040; [0.23]	0.011; [0.05]
22.6	0.262; [1.13]	0.050; [0.47]	0.014; [0.20]
23.1	0.197; [1.03]	0.035; [0.43]	0.010; [0.19]
23.6	0.186; [0.77]	0.033; [0.23]	0.009; [0.06]
24.1	0.184; [0.48]	0.032; [0.14]	0.009
24.6	0.182; [0.31]	0.032	0.008
25.6	0.182	0.031	0.008

TABLE 19. RATIO OF INTENSITY TO THE INTENSITY OF THE FIRST ORDER FOR VARIOUS ANGLES FOR THE JULY 22<sup>nd</sup> EXPERIMENT.

ANGLE	I(2)/I(1); [DATA]	I(3)/I(1); [DATA]	I(4)/I(1); [DATA]
20.1	0.184	0.034	0.009
21.1	0.186; [0.48]	0.034; [0.11]	0.009
21.6	0.198; [0.69]	0.036; [0.24]	0.010; [0.09]
22.1	0.214; [0.80]	0.040; [0.38]	0.011; [0.17]
22.6	0.212; [0.82]	0.039; [0.36]	0.011; [0.16]
23.1	0.215; [0.85]	0.040; [0.37]	0.011; [0.12]
23.6	0.191; [0.62]	0.034; [0.24]	0.009
24.1	0.183; [0.46]	0.032	0.009
24.6	0.183; [0.32]	0.032	0.009
25.6	0.182	0.031	0.008

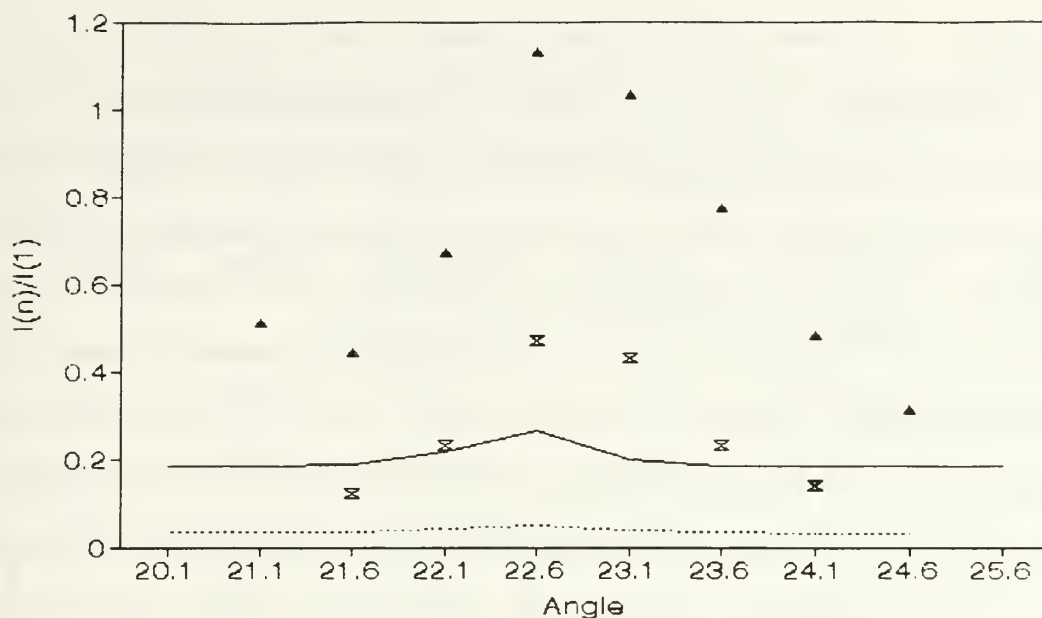


Figure 40. Plot of the experimental and theoretical ratio of the nth order intensities to the first order ( $I(n)/I(1)$ ) for the  $n=2$  and  $n=3$  peaks for the June 5th experiment (far region).

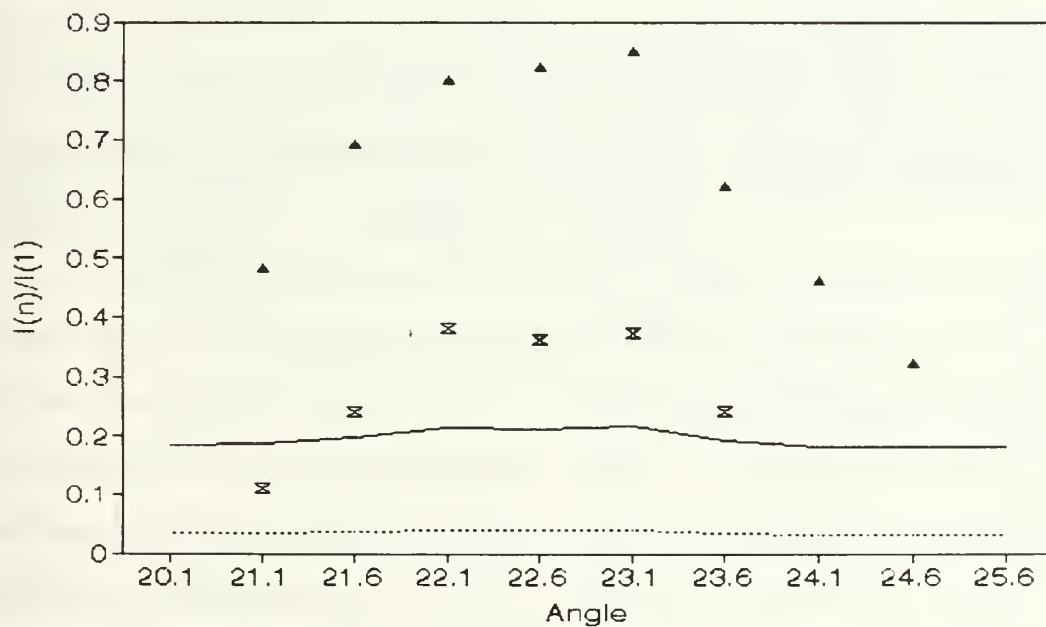


Figure 41. Plot of the experimental and theoretical ratio of the nth order intensities to the first order ( $I(n)/I(1)$ ) for the  $n=2$  and  $n=3$  peaks for the July 22nd experiment (near region).

experiments. The current was determined by using the area of the tin peak in the 19.1 and 21.1 degrees spectra for the June 5<sup>th</sup> and July 22<sup>nd</sup> experiments respectively. These angle were used since the scaling is based on them, and therefore the current will be normalized to this current. Table 20 and 21 show the experimental values, the theoretical values and the ratio of experiment to theory for the first order peaks at the various angles for the June 5<sup>th</sup> and July 22<sup>nd</sup> experiments respectively. The theoretical values are calculated using the theory presented in Chapter I. The large variation between the far region and the near region are due to the larger solid angle subtended by the detector in the near region. A larger solid angle corresponds to a larger field of view. These values were computed using computer integration of equation (23). An example of the computer variables is presented in Appendix B. Again, the theoretical values are much lower than the data in both the far and the near case. All of the analysis consistently shows that the data is clearly much larger than expected.

TABLE 20. NUMBER OF PHOTONS PER ELECTRON FOR THE DATA, THEORY WITHOUT MOSAIC SPREAD OR MULTIPLE SCATTERING AND THEORY WITH MOSAIC SPREAD AND MULTIPLE SCATTERING, FOR THE FIRST ORDER PEAK VERSUS ANGLE FOR THE JUNE 5<sup>th</sup> EXPERIMENT ( $I = 3.39\text{E-}19$  AMPS).

ANGLE	DATA	THEORY WITHOUT SCATTERING	<u>DATA</u> THEORY	THEORY WITH SCATTERING	<u>DATA</u> THEORY
21.1	8.77e-7	8.85e-9	10	5.77e-9	15
21.6	2.16e-7	2.13e-8	10	1.30e-8	17
22.1	4.64e-7	7.99e-8	508	3.43e-8	14
22.6	1.95e-6	1.34e-7	15	3.77e-8	52
23.1	1.65e-6	4.72e-8	35	2.55e-8	65
23.6	3.82e-7	1.60e-8	24	1.03e-8	37
24.1	1.90e-7	7.82e-9	24	5.29e-9	36
24.6	1.40e-7	4.64e-9	30	3.20e-9	44
25.6	5.32e-8	2.18e-9	24	1.53e-9	35

TABLE 21. NUMBER OF PHOTONS PER ELECTRON FOR THE DATA, THEORY WITHOUT MOSAIC SPREAD OR MULTIPLE SCATTERING AND THEORY WITH MOSAIC SPREAD AND MULTIPLE SCATTERING, FOR THE FIRST ORDER PEAK VERSUS ANGLE FOR THE JULY 22<sup>nd</sup> EXPERIMENT (I = 4.17X10<sup>-15</sup> AMPS). *Near End*

ANGLE	DATA	THEORY WITHOUT SCATTERING	<u>DATA</u> THEORY	THEORY WITH SCATTERING	<u>DATA</u> THEORY
20.1	1.39e-6	3.67e-8	38	2.44e-8	57
21.1	5.26e-6	1.32e-7	40	4.17e-8	126
21.6	1.19e-5	3.75e-7	32	8.36e-8	142
22.1	1.91e-5	8.12e-7	24	2.01e-7	95
22.6	2.59e-5	9.38e-7	28	4.33e-7	60
23.1	1.63e-5	7.31e-7	22	3.44e-7	47
23.6	6.89e-6	2.75e-7	25	1.66e-7	42
24.1	3.61e-6	1.15e-7	31	7.63e-8	47
24.6	2.96e-6	6.27e-8	47	4.30e-8	69
25.6	2.28e-6	2.76e-8	83	1.94e-8	118

Lastly, since the experiment in the near region was done as "rocking data" there wasn't a bandwidth resolution calculation computed for the near region in section IV. B.1. Table 22. lists the values of the natural linewidths of the calibration foils and the observed resolution for the July 22<sup>nd</sup> experiment. Table 23. lists the values of the observed resolution for a given energy, the calculated PXR bandwidth and the expected value as calculated for the near region.

$$N \left( \frac{E_c / \sin \theta_0}{E_c / \cos \theta} \right) = N \frac{\sin \theta_0}{\cos \theta}$$



TABLE 22. LIST OF CALIBRATION FOILS AND THE RESPECTIVE X-RAY ENERGY PEAK VALUES. INCLUDED IN THE LIST ARE THE NATURAL LINEWIDTHS OF THE FOILS, AND THE OBSERVED RESOLUTION.

Element	Energy (KeV)	$\Gamma_{lw}$ (KeV)	$\Gamma_{obs}$ (KeV)
Ti	4.51	0.002	0.150
Y	14.92	0.006	0.470
Sn	25.196	0.010	. <sup>8</sup>

TABLE 23. LIST OF OBSERVED RESOLUTION AND CALCULATED PXR BANDWIDTH FOR THE NEAR REGION FROM THE 22.1 DEGREE PXR SPECTRUM OBTAINED JULY 22ND (NEAR REGION).

Energy (KeV)	$\Gamma_{obs}$ (KeV)	$\Gamma_{PXR}$ (KeV)	Theory
5.02	0.450	0.420	0.332
9.94	0.500	0.384	0.587
14.89	0.205	-	0.835

---

<sup>8</sup>Unable to determine due to poor statistics in peak.

## V. CONCLUSIONS AND RECOMMENDATIONS

Enhanced higher order PXR spectra from the {002} planes of carbon have been observed. The ratio of the higher order peaks to the first order peaks ( $I(n)/I(1)$ ) were examined. These ratios were found to be much larger than expected, and the difference increases with increasing order. The absolute intensity was determined based on the LINAC current calculations from the fluorescent x-ray yield of a 0.0275 mm thick tin foil placed behind the graphite crystal. **The absolute intensity was found to exceed the theoretical values by a minimum factor of approximately 10 when the effect of multiple scattering of the electron beam and the effect of the mosaic spread of the crystal are not considered. This factor increased to more than 3000 when these effects are included.**

This is the first time that the theoretical effects of the limited aperture were examined. The effect of varying the crystal angle with a fixed detector angle (with respect to the electron beam) was examined. The variations with angle of  $I(n,\theta)/I(n,22.6^\circ)$  are consistent with theory when the data and theory are normalized to a given angle (in this case 22.6 degrees.) However, **the absolute yield still greatly exceeds the theoretical values.** That is, for both the far and the near regions  $I(1,\theta)_{\text{data}}/I(1,\theta)_{\text{theory}} \gg 1$ .  $I(n,\theta)/I(1,\theta)$  is not constant with respect to angle as is the theory. The maximum in this ratio occurs at  $\theta_B$ . If current is not monitored, look for the maximum in this ratio to insure the crystal angle is  $\theta_B$ . If current is monitored look for the maximum intensity in the first order peak,  $I(1)$ , to insure the crystal angle is  $\theta_B$ .

Additionally, the PXR spectral resolution was calculated for the far and near region. The detector subtended a solid angle of  $2 \times 10^{-4}$  sr. for the far region and  $2.37 \times 10^{-3}$  sr. for the near region. For the far region the PXR spectral resolution was in agreement with theory for the lower orders, but was narrower than expected for the higher orders. For the near region the PXR spectral resolution was in agreement with theory, such that the resolution was wider for a given energy in the near region than in the far region.

Further studies need to be done to further examine the effects of multiple scattering and mosaic spread. By comparing a thick pure crystal such as Si with other mosaic crystals such as carbon, the effect of mosaic spread can be clarified further.

This study has also shown that although alignment is not extremely critical it is important to take great care in focus and steering of the electron beam. Additionally, the effects of detector drift, or shifts due to other causes should be carefully examined. Many short data runs should be collected. These can then be added on a spreadsheet after shifting the known calibration peaks centroids so that they overlap, thus minimizing these effects.

It is extremely important for calibration purposes to have an x-ray fluorescent foil behind the crystal. This not only greatly improved the analysis, it allowed for the calculation of the LINAC current and the subsequent calculation of the absolute number of photons/electron. Care should be taken in selecting a fluorescent foil whose x-ray de-excitation energy falls between two PXR spectral peaks. Tin worked fairly well for carbon at shallower angles, but overlapped the 5th order peak near the Bragg angle, complicating the analysis.

PXR from a thick mosaic carbon graphite crystal has been shown to be a spectrally bright source of narrow bandwidth at energies equal to approximately 5 KeV and integer multiples thereof. Further study with other crystals could provide additional sources of PXR at other energies as well.

## APPENDIX A. FIGURES OF ROCKING DATA

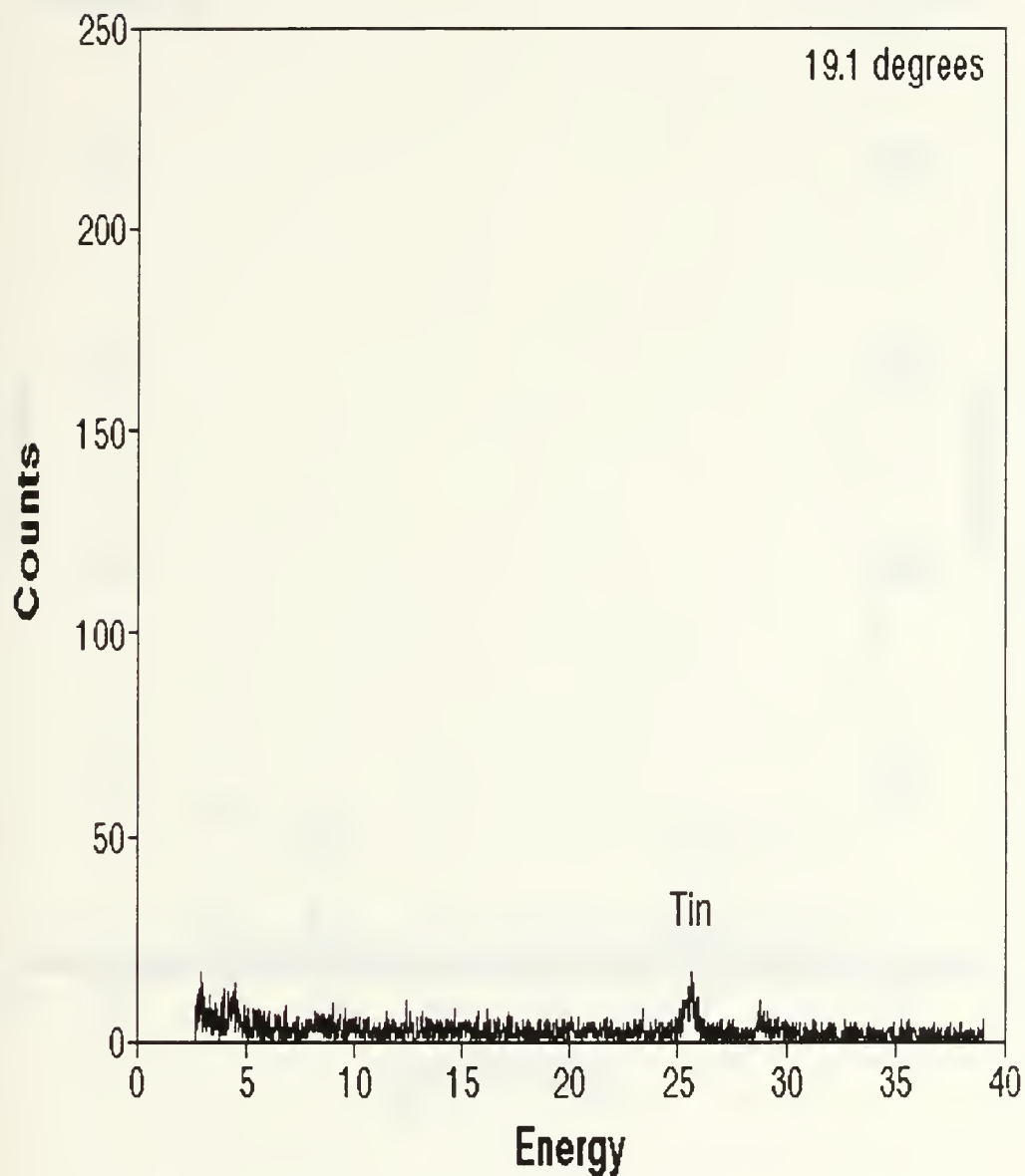


Figure 42. PXR spectrum from the {002} planes of carbon graphite, obtained on 5 June at an angle of 19.1 degrees. This spectrum shows negligible PXR peaks and a tin peak at about 25 keV.

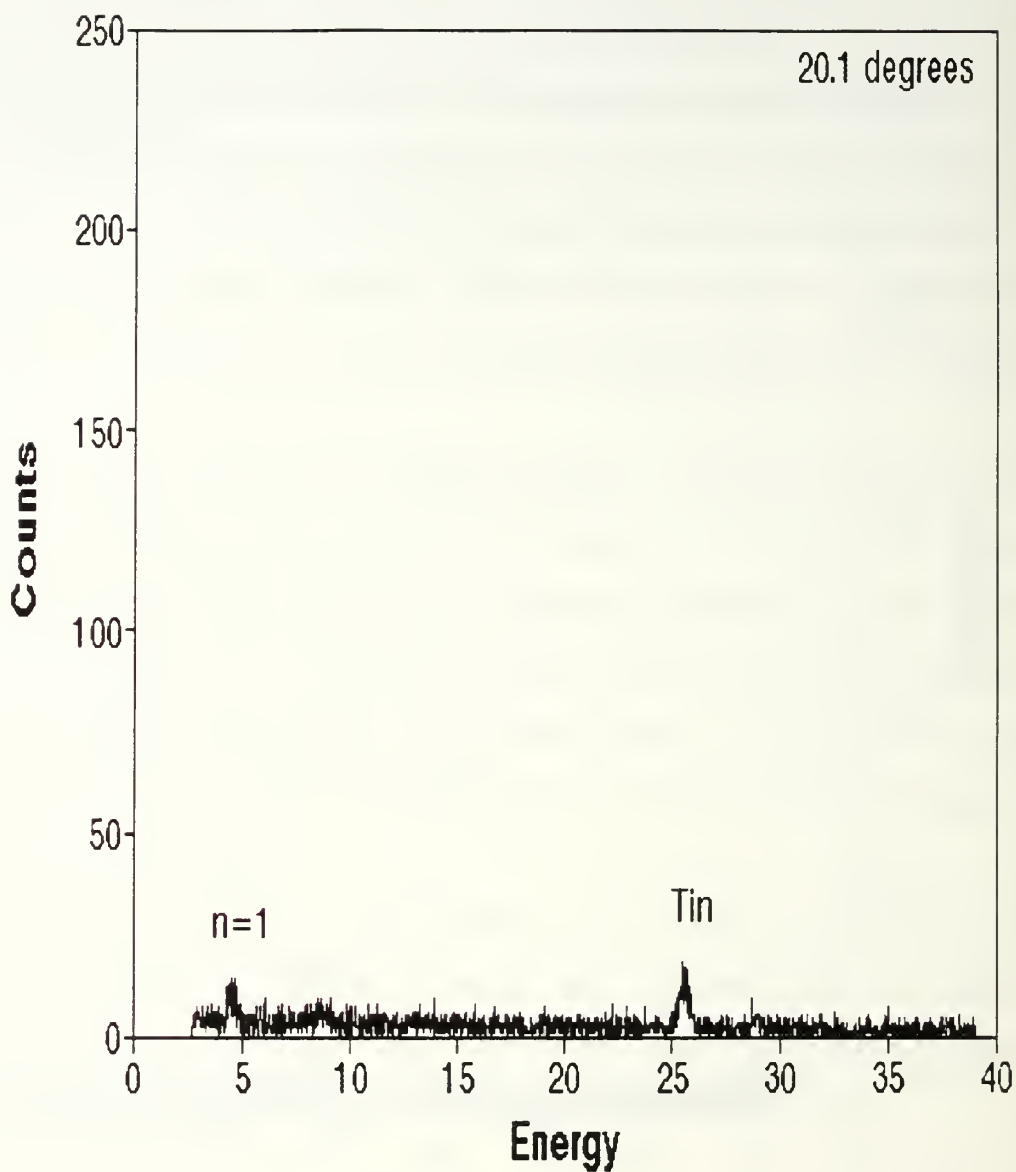


Figure 43. PXR spectrum from the {002} planes of carbon graphite, obtained on 5 June at an angle of 20.1 degrees. This spectrum shows a small first order PXR peak and a tin peak at about 25 keV.



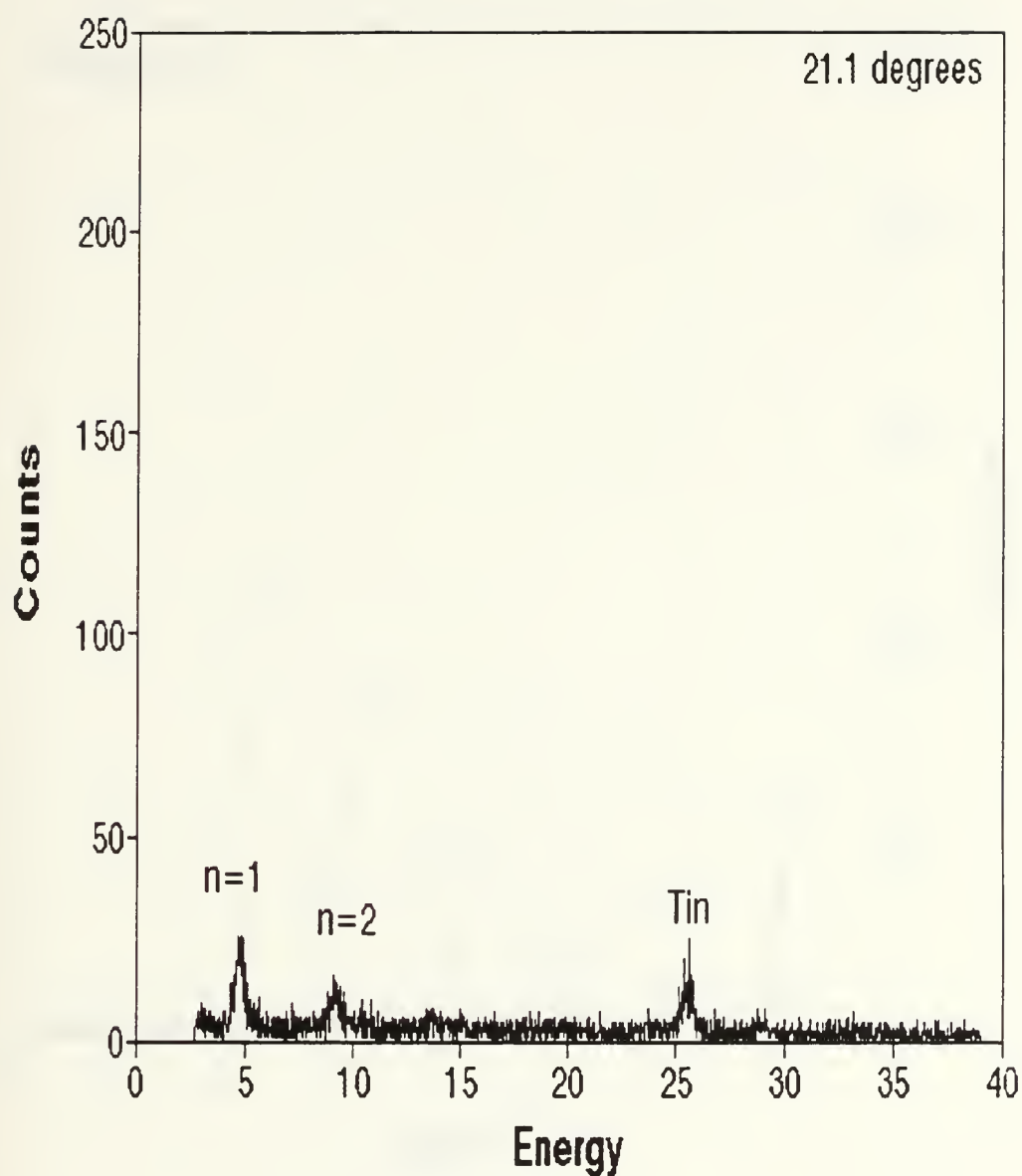


Figure 44. PXR spectrum from the {002} planes of carbon graphite, obtained on 5 June at an angle of 21.1 degrees. This spectrum shows the first 2 orders of PXR peaks and a tin peak at about 25 keV.

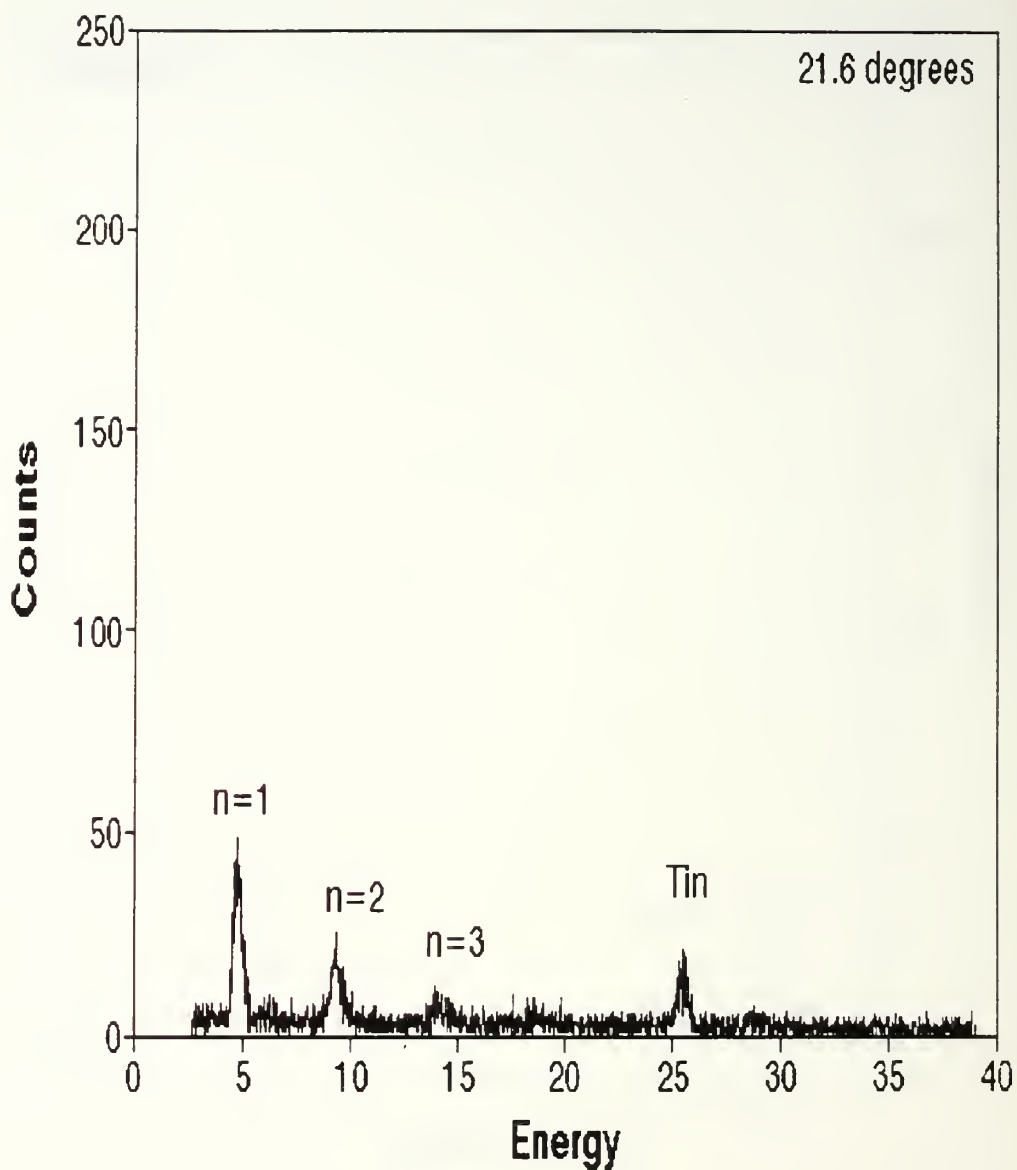


Figure 45. PXR spectrum from the {002} planes of carbon graphite, obtained on 5 June at an angle of 21.6 degrees. This spectrum shows three orders of PXR peaks and a tin peak at about 25 keV.

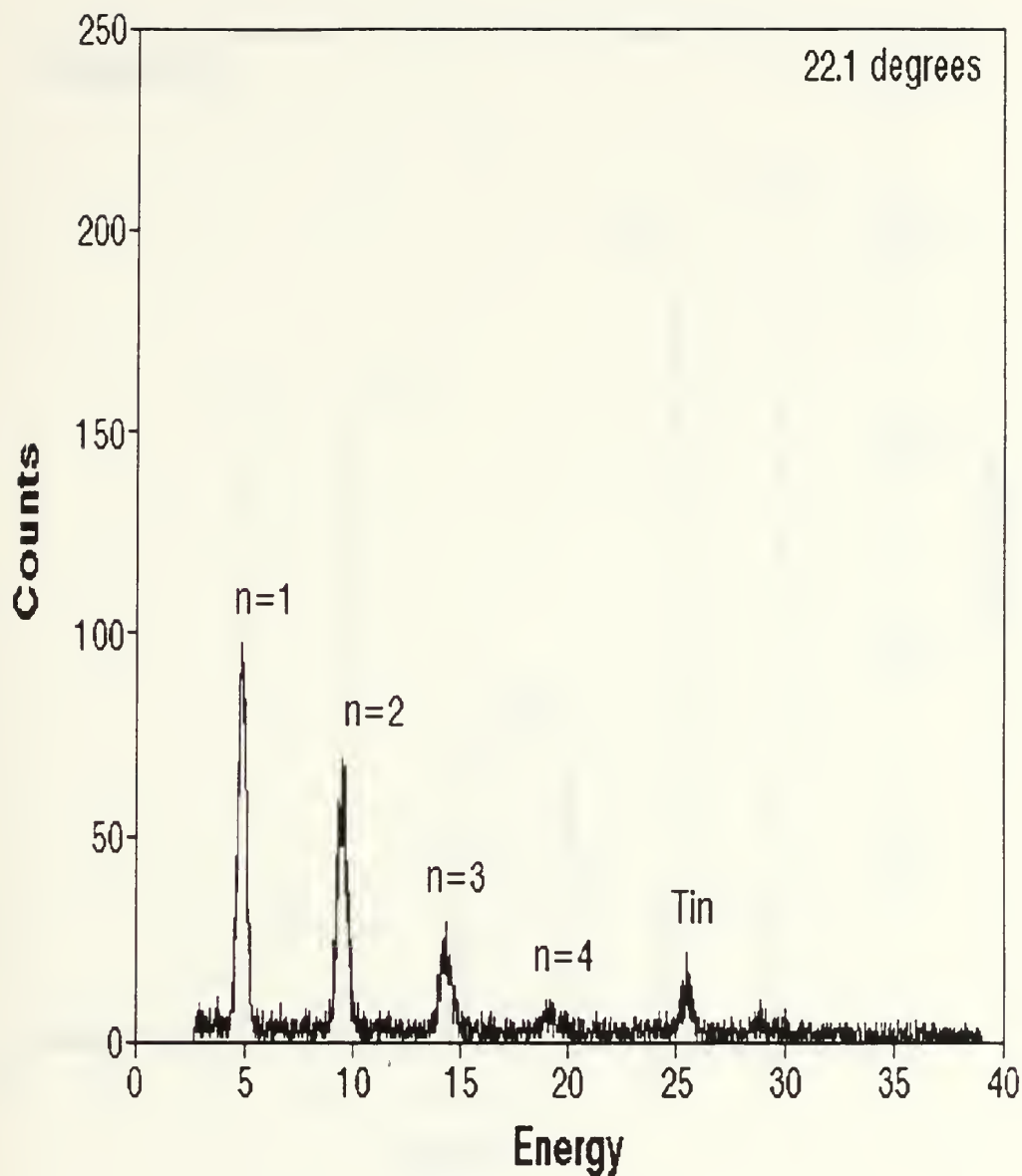


Figure 46. PXR spectrum from the {002} planes of carbon graphite, obtained on 5 June at an angle of 22.1 degrees. This spectrum shows possibly four orders of PXR peaks and a tin peak at about 25 keV.

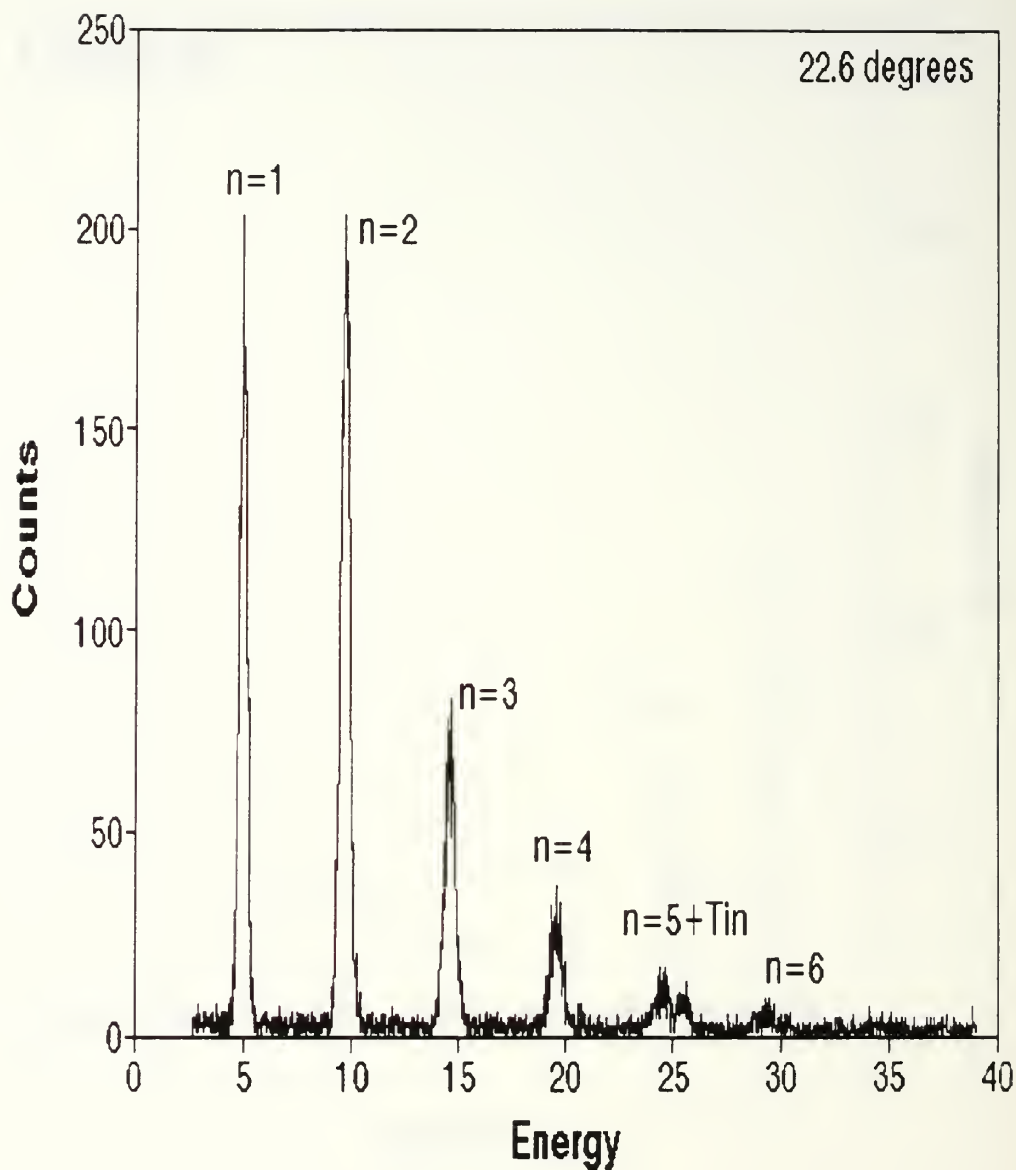


Figure 47. PXR spectrum from the {002} planes of carbon graphite, obtained on 5 June at an angle of 22.6 degrees. This spectrum shows six orders of PXR peaks. The fifth order peak and the Tin calibration peak are overlapping, with the Tin peak at a higher energy than the  $n=5$  peak.

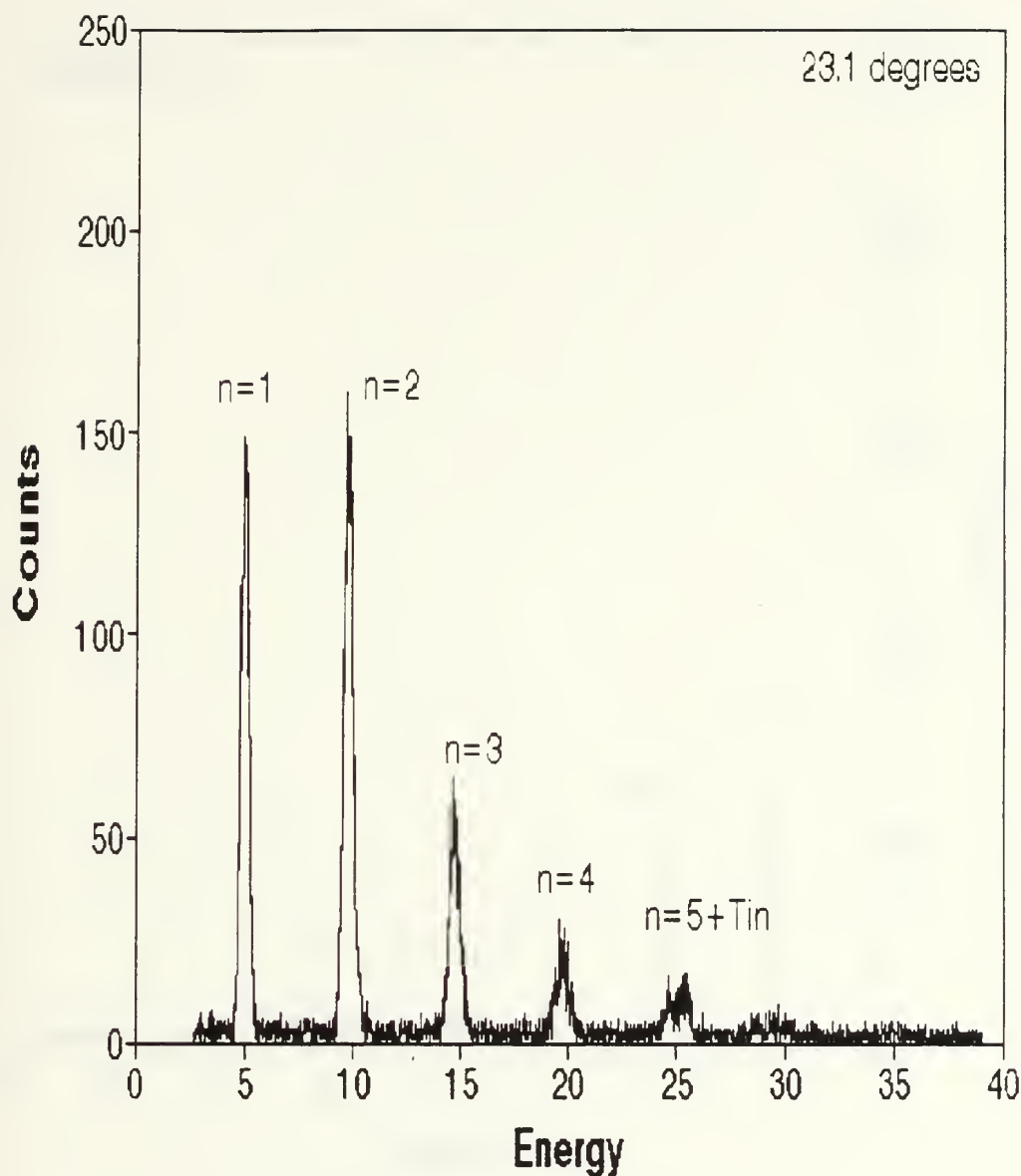


Figure 48. PXR spectrum from the {002} planes of carbon graphite, obtained on 5 June at an angle of 23.1 degrees. This spectrum shows five orders of PXR peaks. The fifth order peak and the Tin calibration peak are overlapping even more than at 22.6 degrees, with the Tin peak at a higher energy than the n=5 peak.



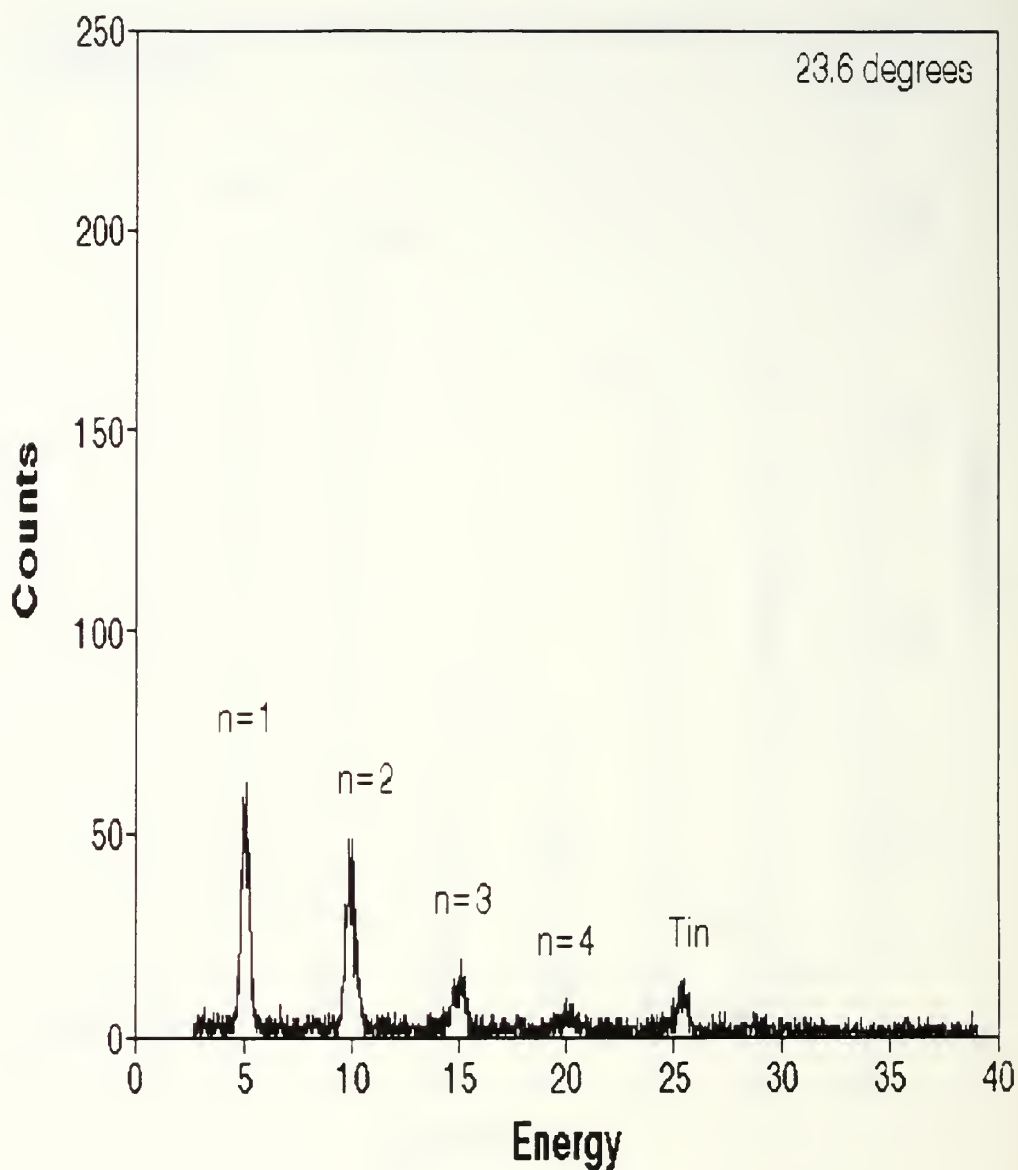


Figure 49. PXR spectrum from the {002} planes of carbon graphite, obtained on 5 June at an angle of 23.6 degrees. This spectrum shows possibly four orders of PXR peaks and a tin peak at about 25 keV.

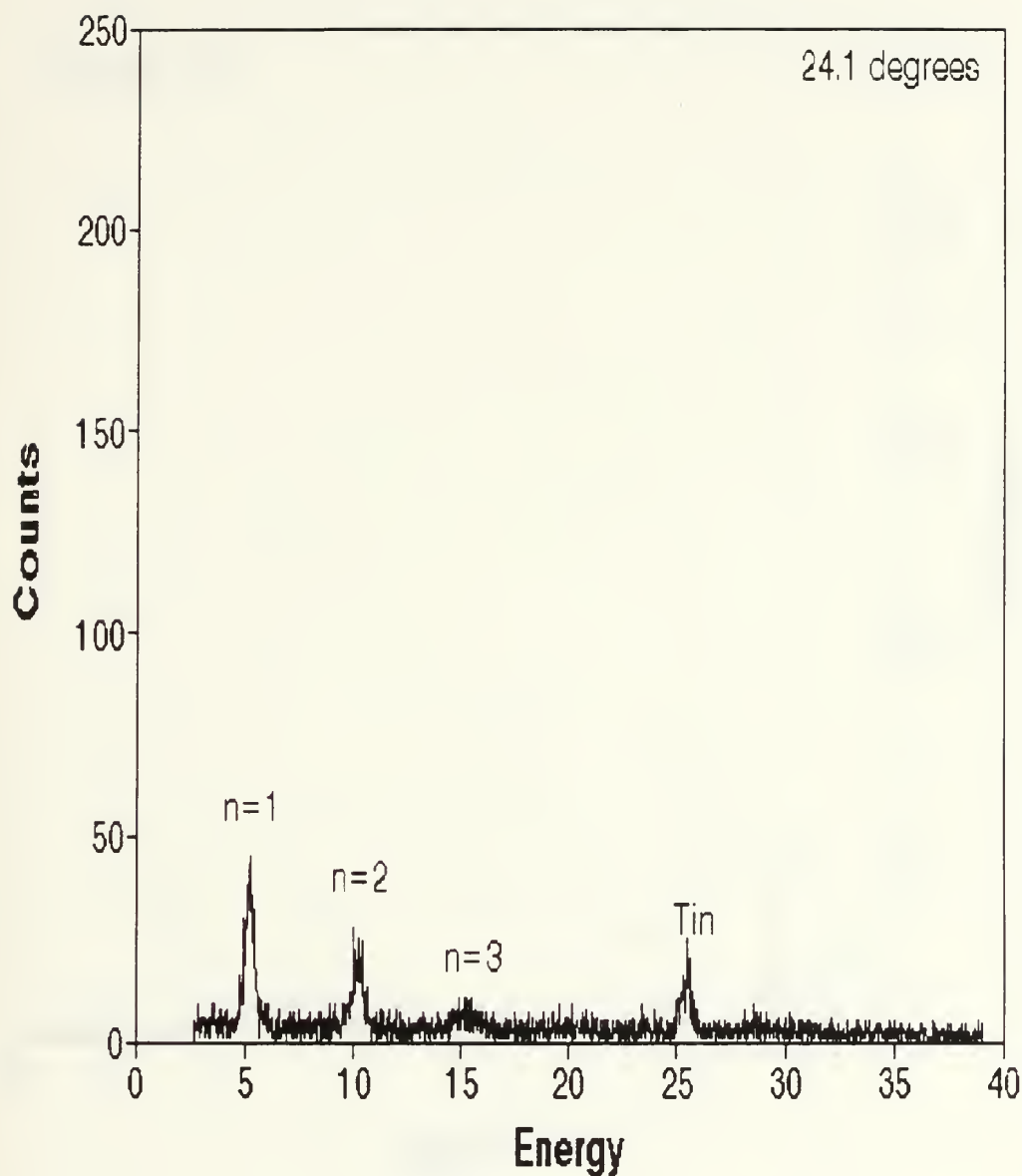


Figure 50. PXR spectrum from the {002} planes of carbon graphite, obtained on 5 June at an angle of 24.1 degrees. This spectrum shows three orders of PXR peaks and a tin peak at about 25 keV.

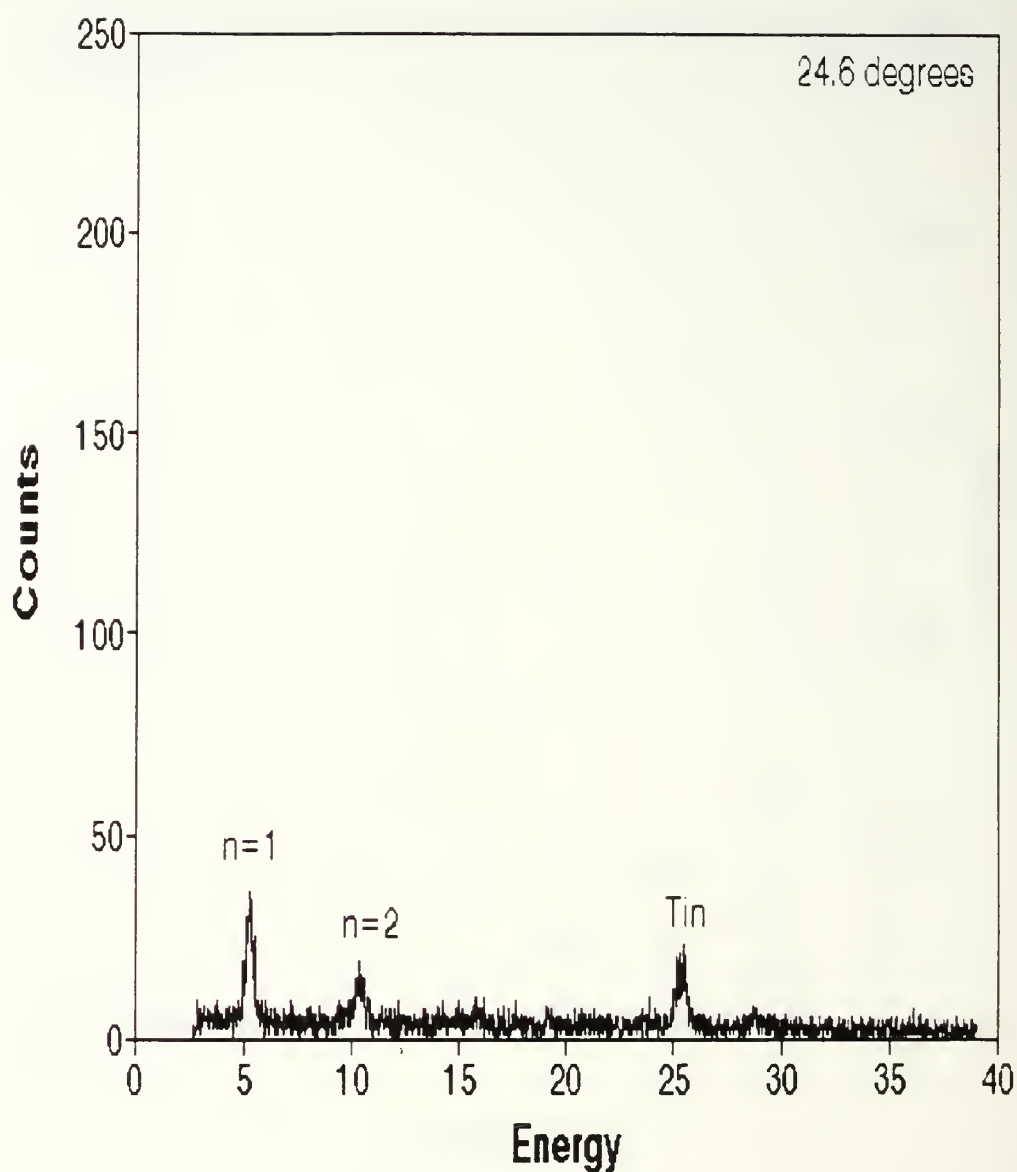


Figure 51. PXR spectrum from the {002} planes of carbon graphite, obtained on 5 June at an angle of 24.6 degrees. This spectrum shows two orders of PXR peaks and a tin peak at about 25 keV.

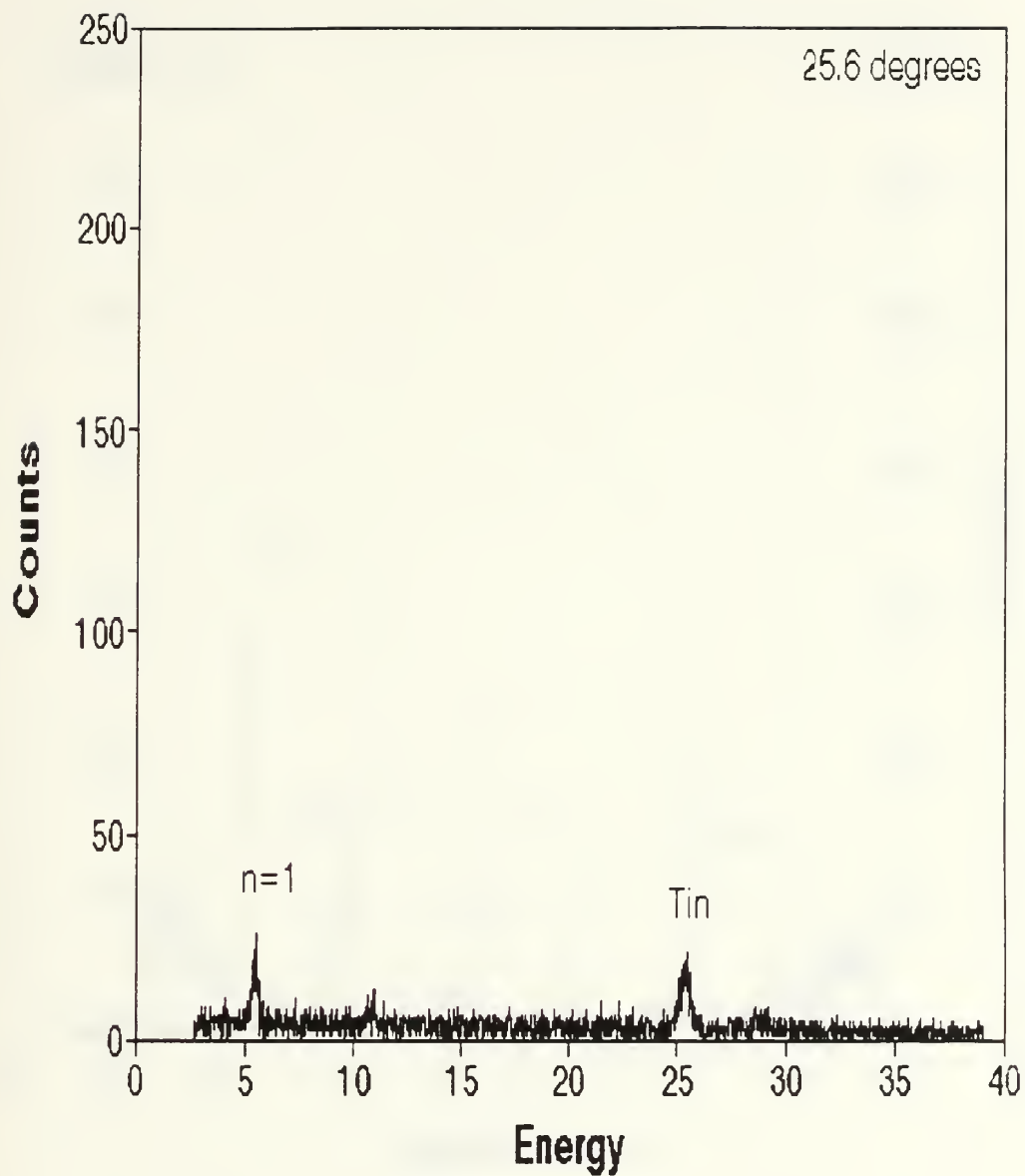


Figure 52. PXR spectrum from the {002} planes of carbon graphite, obtained on 5 June at an angle of 25.6 degrees. This spectrum shows possibly two orders of PXR peaks and a tin peak at about 25 keV.

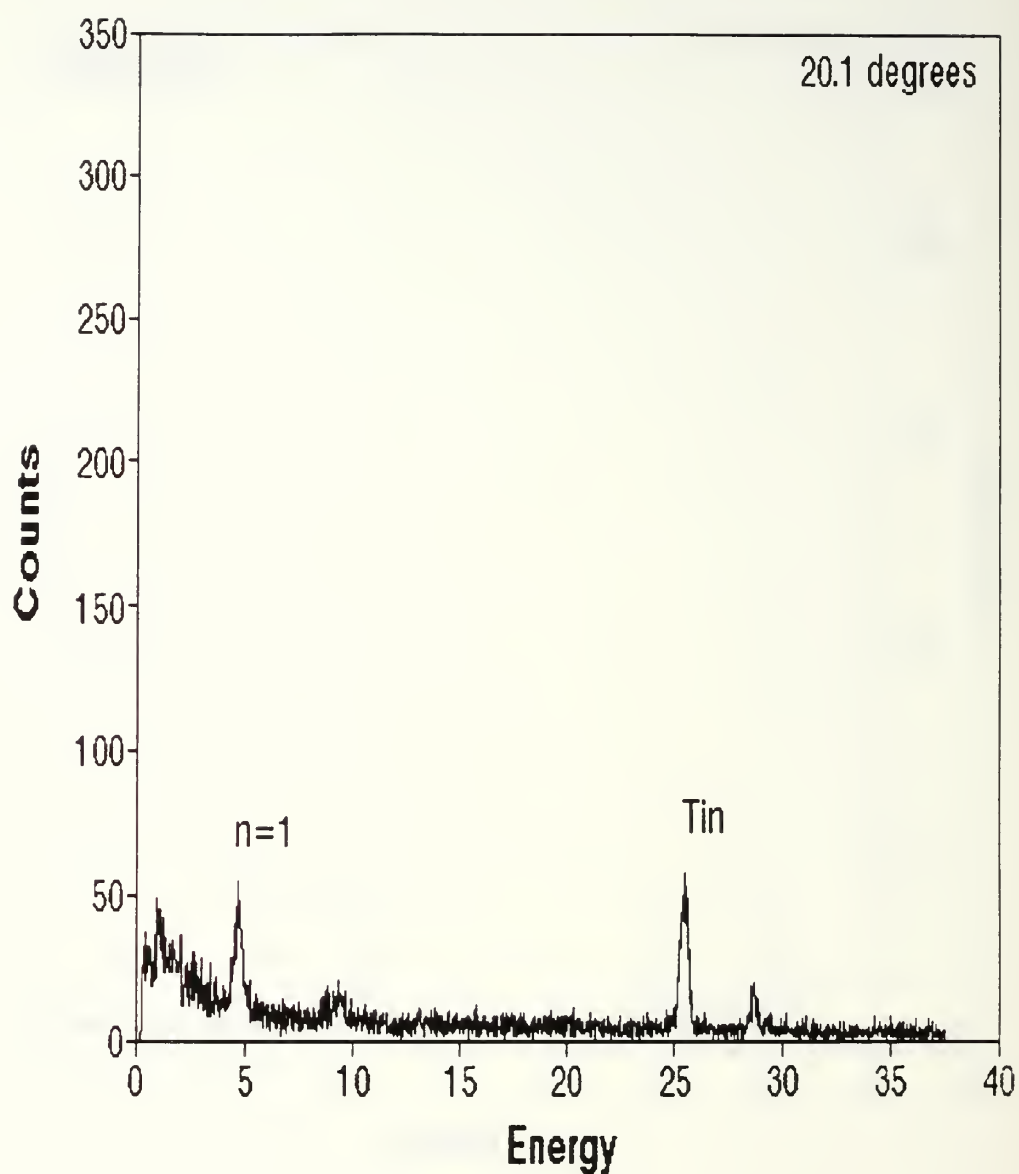


Figure 53. PXR spectrum from the {002} planes of carbon graphite, obtained on 22 July at an angle of 20.1 degrees. This spectrum shows two orders of PXR peaks and the Tin  $K_{\alpha}$  and  $K_{\beta}$  peaks



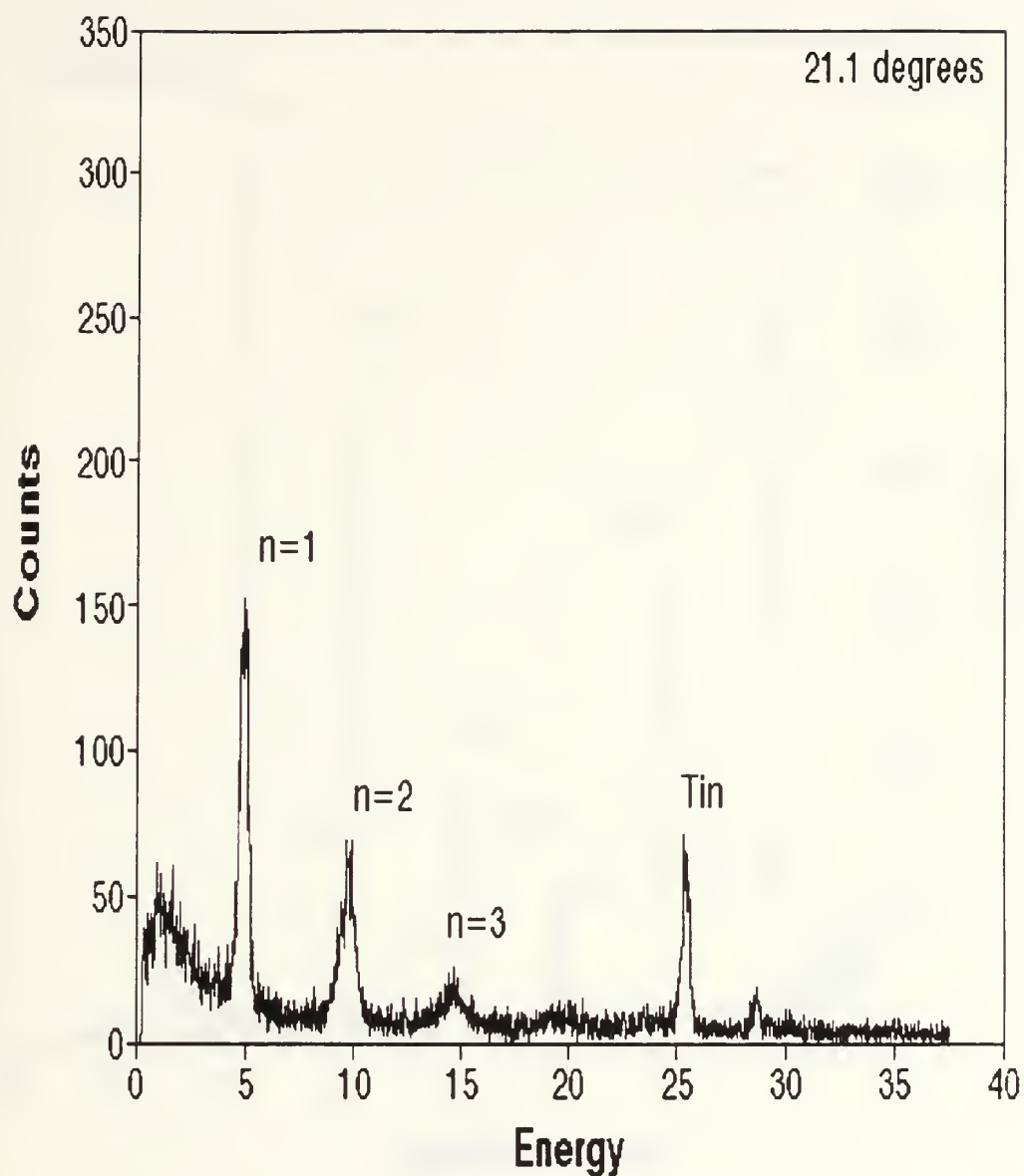


Figure 54. PXR spectrum from the {002} planes of carbon graphite, obtained on 22 July at an angle of 21.1 degrees. This spectrum shows the first and second order PXR peak and the Tin  $K_{\alpha}$  and  $K_{\beta}$  peaks.

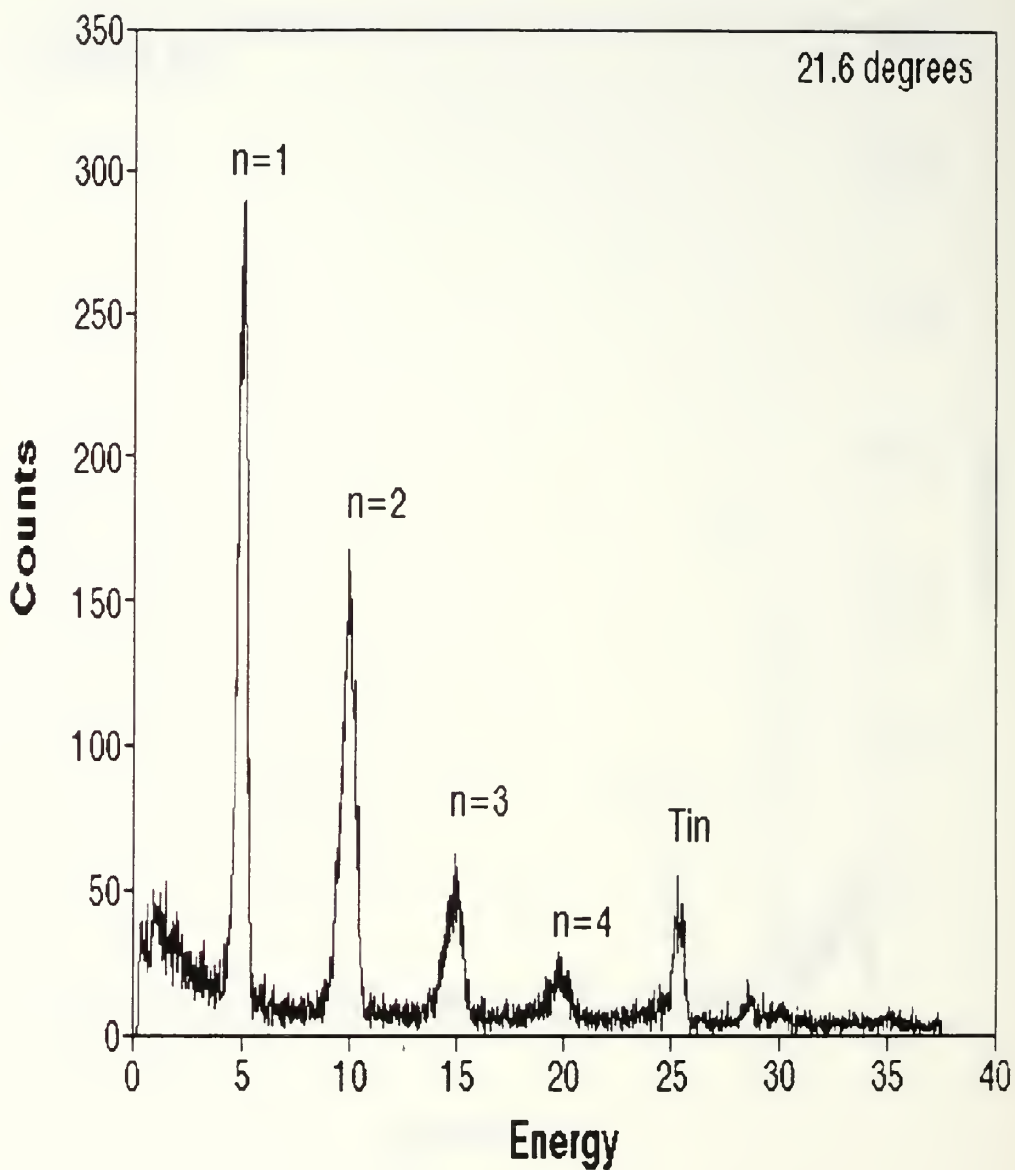


Figure 55. PXR spectrum from the  $\{002\}$  planes of carbon graphite, obtained on 22 July at an angle of 21.6 degrees. This spectrum shows the first 3 orders of PXR peaks and the Tin  $K_{\alpha}$  and  $K_{\beta}$  peaks.

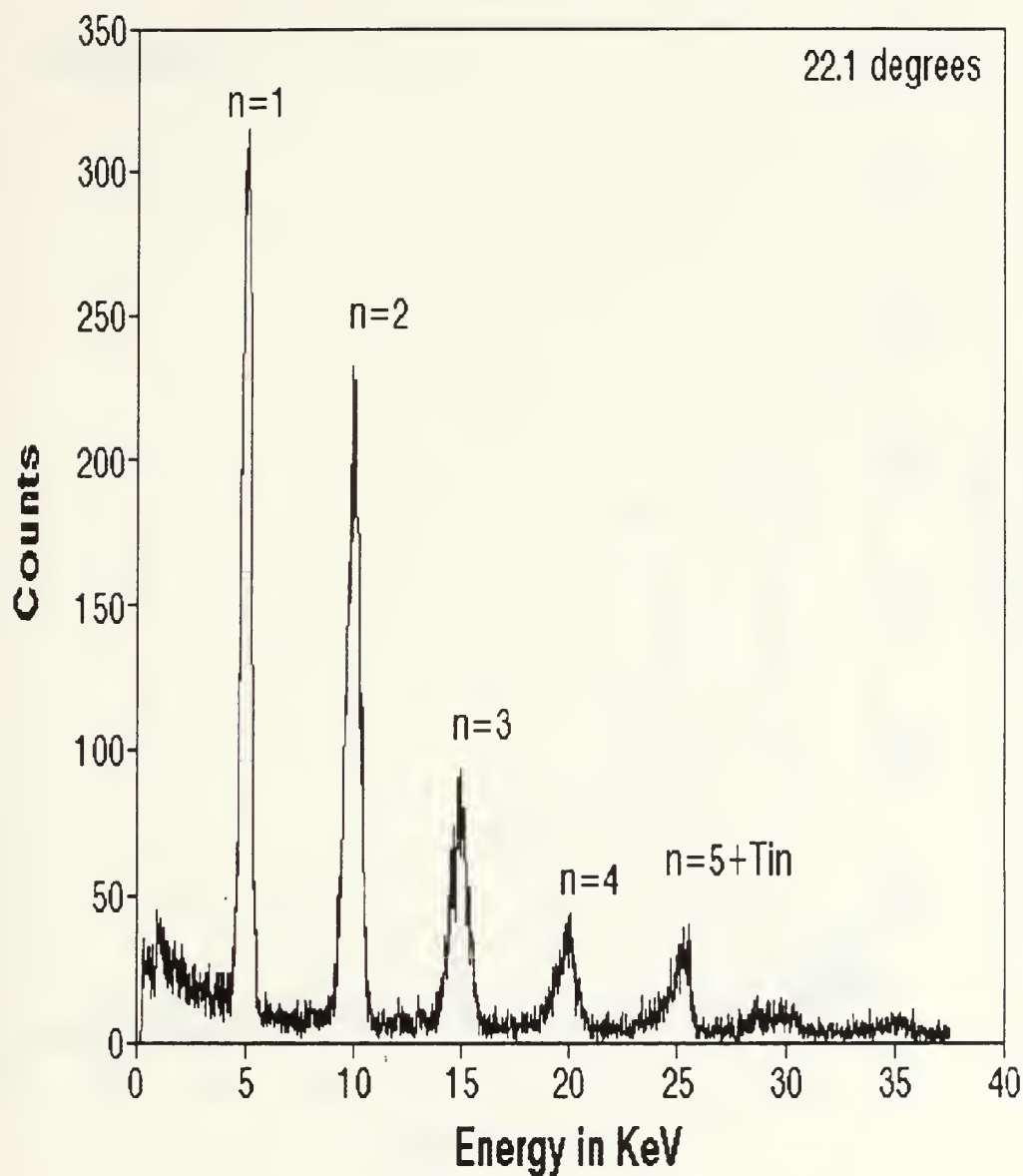


Figure 56. PXR spectrum from the {002} planes of carbon graphite, obtained on 22 July at an angle of 22.1 degrees. This spectrum shows four orders of PXR peaks and the Tin  $K_{\alpha}$  and  $K_{\beta}$  peaks.

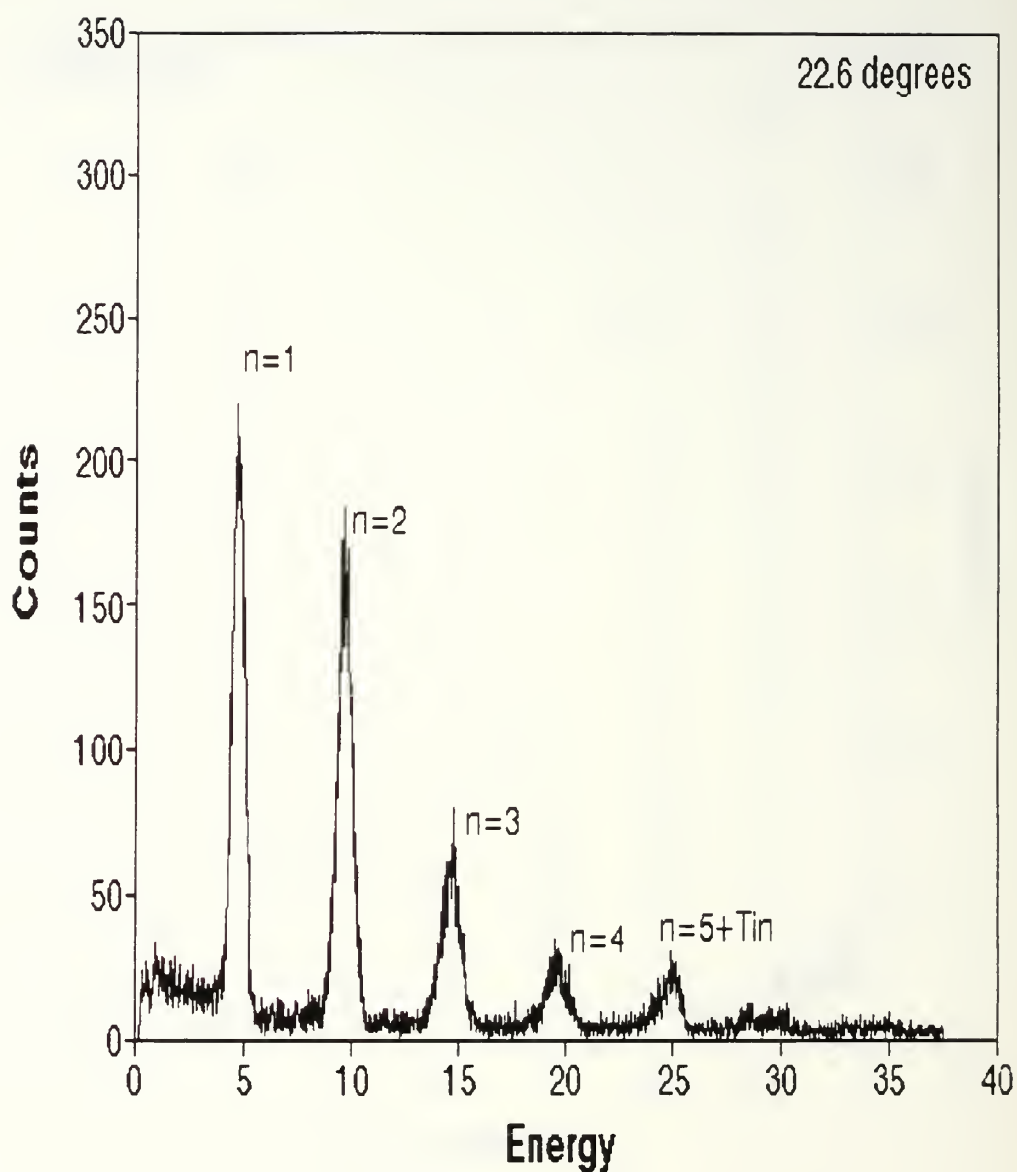


Figure 57. PXR spectrum from the {002} planes of carbon graphite, obtained on 22 July at an angle of 22.6 degrees. This spectrum shows five orders of PXR peaks with the Tin peak and n=5 peaks overlapping.

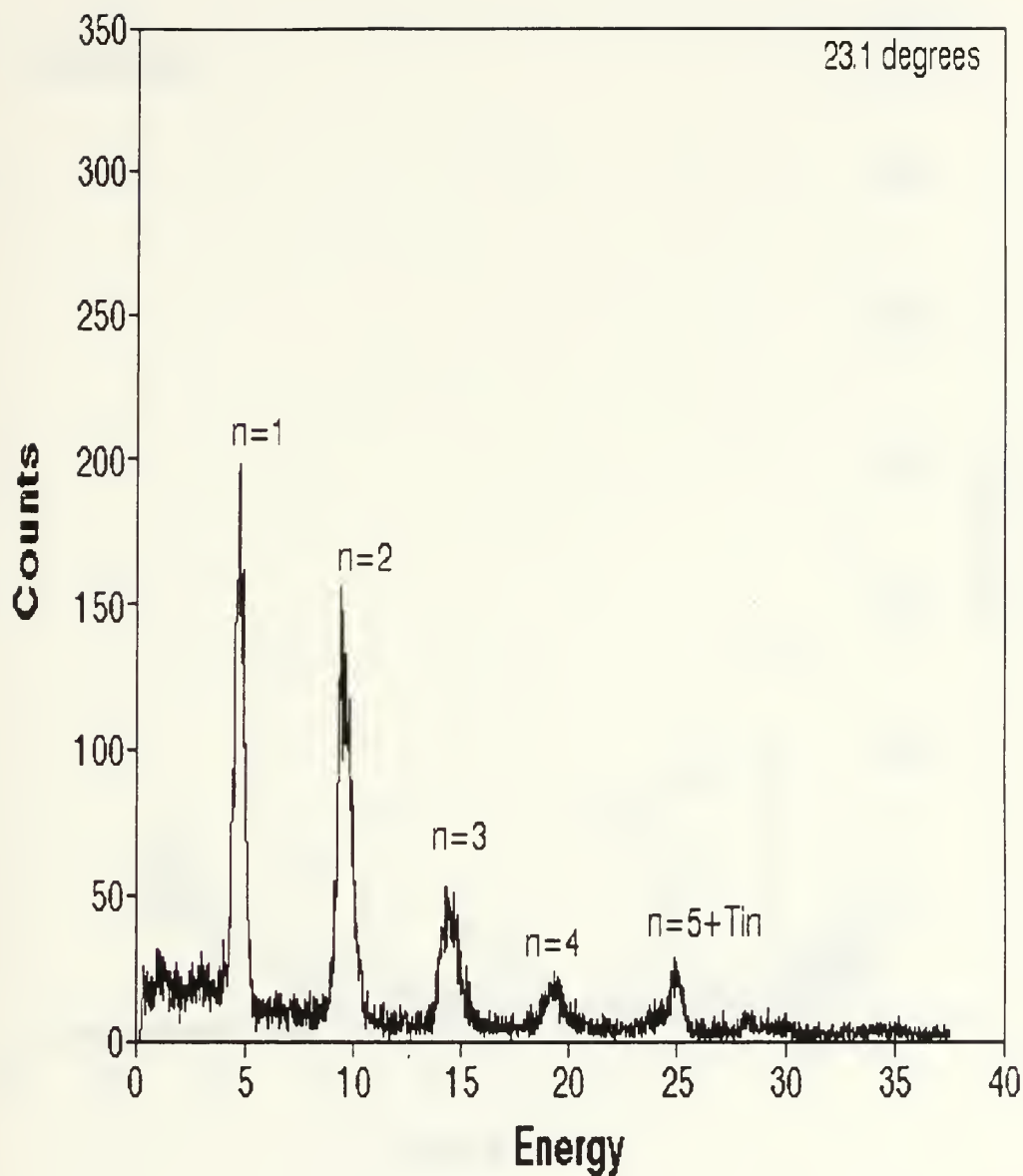


Figure 58. PXR spectrum from the {002} planes of carbon graphite, obtained on 22 July at an angle of 23.1 degrees. This spectrum shows five orders of PXR peaks. The fifth order peak and the Tin calibration peak are overlapping.



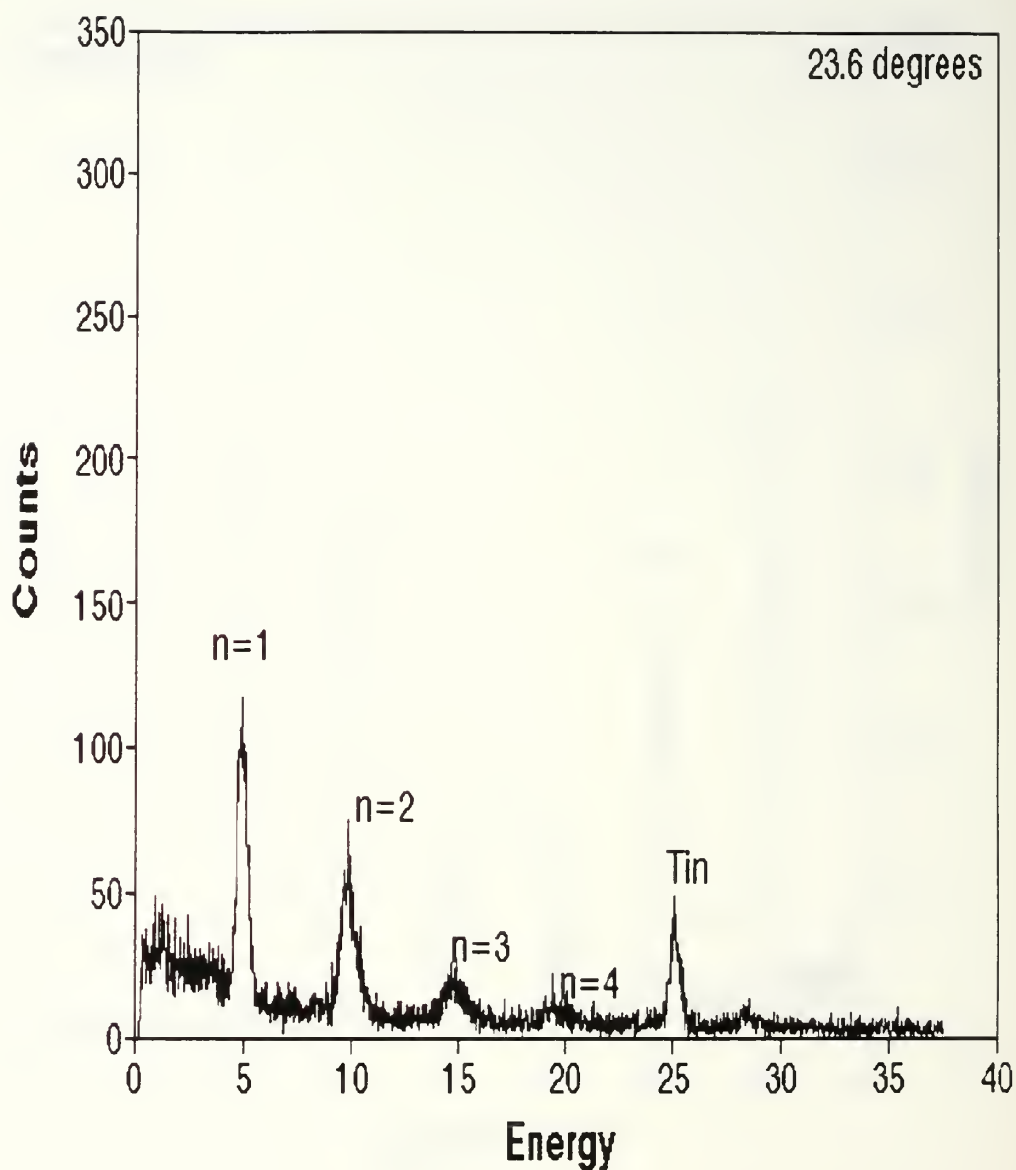


Figure 59. PXR spectrum from the {002} planes of carbon graphite, obtained on 22 July at an angle of 23.6 degrees. This spectrum shows possible five orders of PXR peaks. The fifth order peak and the Tin calibration peak are overlapping .

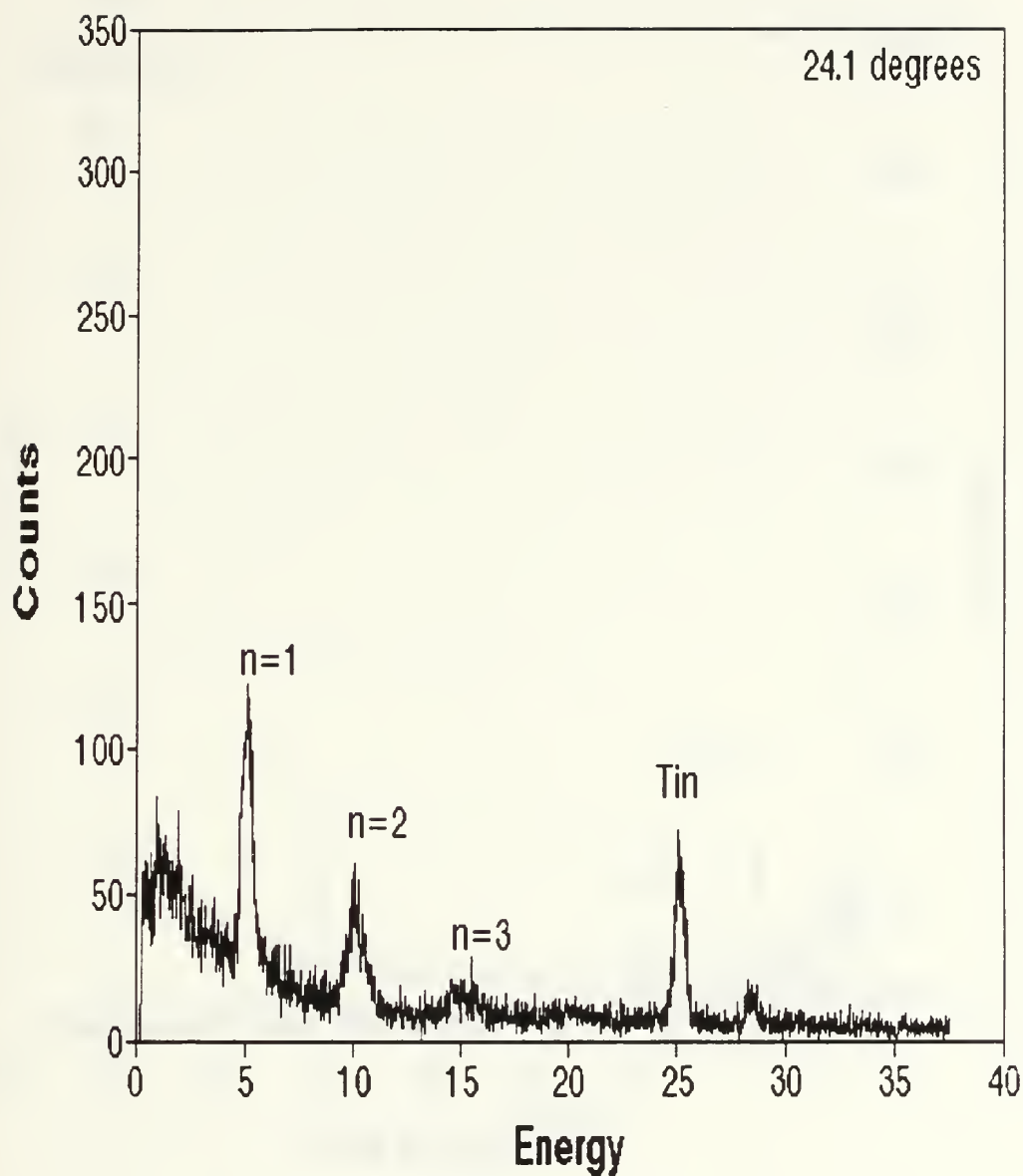


Figure 60. PXR spectrum from the {002} planes of carbon graphite, obtained on 22 July at an angle of 24.1 degrees. This spectrum shows possibly four orders of PXR peaks and a tin peak at about 25 keV.

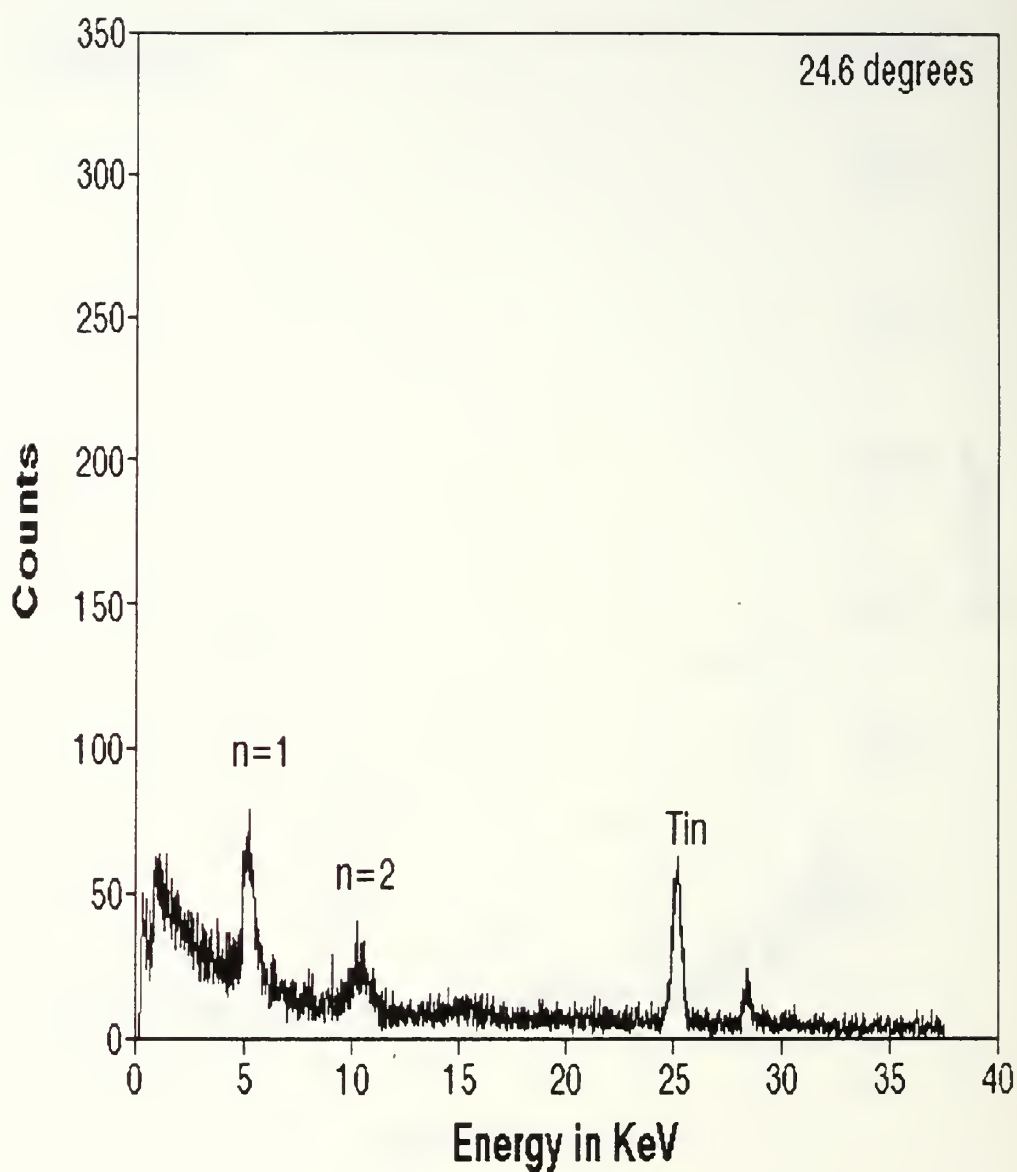


Figure 61. PXR spectrum from the {002} planes of carbon graphite, obtained on 22 July at an angle of 24.6 degrees. This spectrum shows three orders of PXR peaks and a tin peak at about 25 keV.

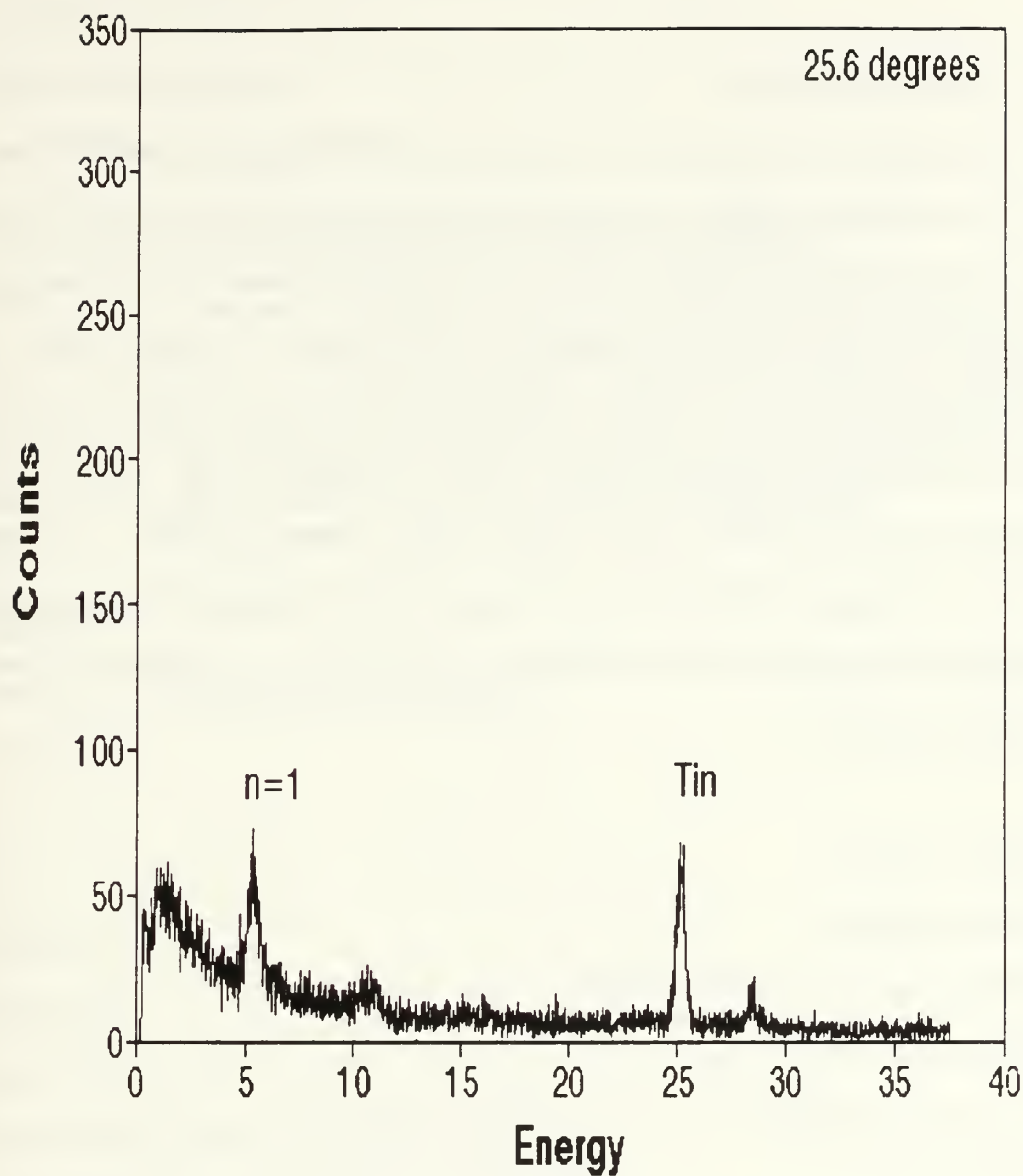


Figure 62. PXR spectrum from the {002} planes of carbon graphite, obtained on 22 July at an angle of 25.6 degrees. This spectrum shows two orders of PXR peaks and the Tin  $K_{\alpha}$  and  $K_{\beta}$  peaks.

## APPENDIX B

### A. PROGRAM IN C.

This program was written in C to convert the ASCII output from the PHA-II software to a file readable by QPRO. It binned every four channels into one bin and assigned the value of the third bin's energy to that bin. This program allowed the 8192 channels to be displayed in 2048 channels for comparison with the spectra obtained using the 2048 channel PHA-I software. To prepare the file, an editor was used to eliminate the commas, remove the heading comments and add "2045" to the top of the file. The output was in the form of "New channel number, Energy, counts" (comma's included). The parameter for the conversion from channel to energy must be changed from experiment to experiment depending upon the calibration for that data. See Chapter III section C equations (28)-(30).

```
#include <stdio.h>
#include <math.h>
main() {int ea, eb, ec, ed, i, N, counts;
float ca, cb, cc, cd, E;
int roia, roib, roic, roid;
scanf("%d",&n);
E=0.0;
counts=0.0; ca=0; cb=0; cc=0; cd=0;
for (i=0;i<N;++i) { scanf("%d%f%d",&ea,&ca,&roia);
scanf("%d%f%d",&eb,&cb,&roib);
scanf("%d%f%d",&ec,&cc,&roic);
scanf("%d%f%d",&ed,&cd,&roid);
counts=(int)(ca+cb+cc+cd);
```

```

E=0.00472*(i*4+2)-1.04;
printf("%d",i); printf(",");
printf("%g",E); printf(",");
printf("%d",counts); printf("\n"); } }

```

## B. COMPUTER INTEGRATION PROGRAM EXAMPLE

This program was used to determine the absolute intensity and the energy bandwidth for the PXR spectra. The various parameters changed based upon the experimental conditions. This example uses the variable for the far region at a crystal angle of 22.5 degrees. It includes the effects of multiple scattering and mosaic spread.

```

n=1
enbeam=90.0
flvec=(2.01,1.34,0.0946,0.624,0.402,0.268)
fl=flvec[n]
z=6
an=12
thetamm=0.4
thetabb=22.5
dang=6.708
Lavec=(0.0213,0.181,0.573,1.104,1.586,1.939)
La=Lavec[n]
dthetax=15/1002.19
dthetay=15/1002.19
dnm=dang/10
gam=(.511+enbeam)/.511
thetam=(pi/180)*thetamm
thetab=(pi/180)*thetabb

```



```

L=.139/sin(thetab)
num=La^2-(1*la+La^3)*exp(-L/La)
den=La*(1-exp(-L/La))
Tave=num/den
k=0.157*z*(z+1)*Tave/An*enbeam^2)
Thetassqr=k*Ln(1.13*z^(4/3)an^(-1)*Tave)
energy=n*2*pi*(197.32)/(dnm*sin(thetab))
lambcm=0.000124/energy
lambang=lambcm*100000000
x0=78.192*6/(energy)^2
x10sqr=(1.039e-12)*(lambang^4)*f1^2
thetap=sqrt((1/gam^2)+x0+thetassqr+thetam^2)
alphay=dthetay/(2*thetap)
alphax=dthetax/(2*thetap)
cs2=(cos(2*thetab))^2
j1(x)=(1+x^2*(1+cs2))/(1+x^2)^1.5
Q(x)=atan(alphay/(1+x^2)^.5)
j2a(x)=x^2*cs2*((alphay/(1+x^2))*1/(alphay^2+1+x^2)+Q(x)/(1+x^2)^1.5)
j2(x)=(j2a(x)+Q(x)/(1+x^2)^.5-alphay/(alphay^2+1+x^2)))
factor=(1-exp(-L/La))
coeff=x10sqr*La/(4*sin(thetab)*cos(thetab)lambcm*thetap*energy*137)*factor
dNdE1(x)=pi*coeff*j1(x)
dNdE2(x)=2*coeff*j2(x)
xdNdE2(x)=x*dNdE2(x)
x1=((pi/180)*(45-2*thetabb)+.5dthetax)/thetap
x2=((pi/180)*(45-2*thetabb)-.5dthetax)/thetap
xcent=(in((1e-5*xdNdE2(x)),x=x1 to x2))/(in((1e-5*dNdE2(x)),x=x1 to x2))

```

$acent = xcent * energy * \theta / \tan(\theta_{tab}) + energy$

$area = \int (dN/dE^2(x), x = x1 \text{ to } x2)$

$resolution = (x1 - x2) * energy * \theta / \tan(\theta_{tab})$ .

## LIST OF REFERENCES

1. Adishchev, Y.N., and others, "Measurements of Parametric X-Rays from Relativistic Electrons in Silicon Crystals", Nuclear Instruments and Methods in Physics Research, v. B21, pp. 49055, 1987.
2. Rule, D.W., and others, "Production of X-Rays by the Interaction of Charged Particle Beams with Periodic Structures in Crystalline Materials", paper no. 25 presented at SPIE's International Symposium on Optical Science and Engineering Conf. no. 1552 Short Wavelength Radiation Sources, San Diego, California, 21-26 July 1991.
3. Baryshevsky, V.G., and others, "Experimental Observation of Parametric X-Rays from Ultrarelativistic Electrons", J. Physics D: Applied Physics, v. 19, pp. 171-176, 1986.
4. Osborne, M.J., "Higher Order Parametric X-Rays", Masters thesis, Naval Postgraduate School, Monterey, California, December 1991.
5. Evertson, S., "Experimental Considerations of Higher Order Parametric X-Rays From Silicon Crystals of Varying Thicknesses", Masters thesis, Naval Postgraduate School, Monterey, California, June 1992.
6. Baryshevsky, V.G., and others, "A Comparative Analysis of Various Mechanisms for the Generation of X-Rays by Relativistic Particles", Nucl. Instrum. and Methods in Phys. Res. 228, pp.490-495, 1985.
7. Fiorito, R.B., and others, "PXR Generation From Moderate Energy Electron Beams", Proc. of 12th International Conference on Applications of Accelerators in Research and Industry. Denton Texas, November 1992.
8. Feranchuk, I.D. and Ivanshin, A.V., "Theoretical Investigation of the Parametric X-Ray Features", J. Physique, v. T46, no. 11, pp. 1981-1986, November 1985.
9. Private communication between Dr. Don Rule, Naval Surface Weapons Center, Silver Spring , Maryland and author, September 1992.
10. Straub, H., and others, Nuclear Physics vol.1, E. Segre, ed., (Wiley).
11. Private communication between D.W. Rule, and R.B. Fiorito, Naval Surface Warfare Command, Silver Spring, Maryland, and the author, August 19, 1992.
12. D. Rule, "Transition Radiation Diagnostics for Intense Charged Particle Beams", Nucl. Instrum. and Methods A296, p. 150, 1990.
13. Private communication between D.W. Rule, and R.B. Fiorito, Naval Surface Warfare Command, Silver Spring, Maryland, and the author, August 4, 1992.

14. Canberra Instruction Manual, Si(Li) Detector System Series 7300, S/N 1191404, revised January 1991.
15. Detector & Instruments for Nuclear Spectroscopy, EG&G ORTEC, pp(2-46)-(2-47), 1991-1992.
16. Union Carbide Incorporated coating services.
17. Fasanello, T.J., "Solid State X-ray Detector Calibration Techniques and LINAC Beam Intensity Measurements", Master Thesis, Naval Postgraduate School, Monterey California, December 1992.
18. Experiments in Nuclear Science AN34 Laboratory Manual, 3d ed., Revised, pp 167-168, EG&G Ortec Incorporated, 1984.
20. TENNELEC/Nucleus Instruction Manual, TC 244 Amplifier Rev 4.0.
21. M.J. Berger and J.H. Hubell, "XCOM:Photon Cross Sections on a Personal Computer", National Bureau of Stds.& Technol., NBSIR 87-3597, Gaithersburg, Maryland, 1987.
22. Borland, "QuattroPro v 3.0", copyright 1992.
23. Allison, S.K. and Compton, A.H., X-Rays in Theory and Experiment, 2nd ed., p. 745, D. Van Nostrand Company, Inc., 1935.
24. Perkins, S.T., Tables and Graphs of Electron-Interaction Cross Sections from 10eV to 100 GeV, Lawrence Livermore National Laboratory, 1991.
25. Perkins, S.T., Tables and Graphs of Atomic Subshell and Relaxation Data, Lawrence Livermore National Laboratory, 1991.
26. Jandel Scientific, "PeakFit v3.0 software", copyright 1991 AISN software.

# INITIAL DISTRIBUTION LIST

	No. Copies
1. Defense Technical Information Center..... Cameron Station Alexandria, VA 22304-6145	2
2. Library, Code 52..... Naval Postgraduate School Monterey, CA 93943-5002	2
3. Dr. K. E. Woehler, Code Ph/Wh..... Department of Physics Naval Postgraduate School Monterey, CA 93943-5002	1
4. Professor X. K. Maruyama, Code Ph/Mx..... Department of Physics Naval Postgraduate School Monterey, CA 93943-5002	20
5. LT K. L. DiNova, USN. .... 809 Rollingwood Ln. Valrico, FL 33594	1
6. Dr. R. B. Riorito, Code R36..... Naval Surface Warfare Center 10901 New Hampshire Avenue Silver Spring, MD 20903-5000	1
7. Dr. D. W. Rule, Code R36..... Naval Surface Warfare Center 10901 New Hampshire Avenue Silver Spring, MD 20903-5000	1
8. Dr. M. A. Piestrup..... 2181 Park Blvd. Palo Alto, CA 94306	1
10. Mr. D. Snyder, Code 61PH..... Department of Physics Naval Postgraduate School Monterey, CA 93943-5002	1

846-217











LIBRARY  
SCHOOL  
CALIFORNIA STATE UNIVERSITY  
5002



DENCO





DUDLEY KNOX LIBRARY



3 2768 00034299 2